
UNCERTAINTY QUANTIFICATION IN MULTI-PHYSICS MODEL FOR WIND TURBINE ASSET MANAGEMENT

Elias FEKHARI

ÉLECTRICITÉ DE FRANCE R&D

Chatou, France

&

CÔTE D'AZUR UNIVERSITY

Nice, France

A thesis submitted in partial fulfilment of the requirements for the degree of

Doctor of Philosophy
(in Computer Science)

publicly defended on March xx, 2024 in front of the following jury:

Pr. Mireille BOSSY,	INRIA, Sophia-Antipolis	Examiner
Dr. Vincent CHABRIDON	EDF R&D, Chatou	Co-advisor
Dr. Sébastien DA VEIGA	ENSAI, Rennes	Examiner
Dr. Bertrand IOOSS	EDF R&D, Chatou	Thesis director
Dr. Anaïs LOVERA	EDF R&D, Saclay	Invite
Dr. Joseph MURÉ	EDF R&D, Chatou	Co-advisor
Pr. Franck SCHOEFS	Nantes Université, Nantes	Reviewer
Pr. Daniel STRAUB	TUM, Munich	Reviewer
Pr. Bruno SUDRET	ETH, Zürich	Examiner

Contents

List of Figures	vii
List of Tables	ix
Introduction	1
I Introduction to uncertainty quantification and wind energy	11
1 Uncertainty quantification in computer experiments	13
1.1 Introduction	14
1.2 Black-box model specification	14
1.3 Enumerating and modeling the uncertain inputs	15
1.3.1 Sources of the input uncertainties	15
1.3.2 Modeling uncertain inputs with the probabilistic framework	16
1.3.3 Joint input probability distribution	17
1.4 Uncertainty propagation for central tendency study	20
1.4.1 Numerical integration	20
1.4.2 Numerical design of experiments	26
1.4.3 Summary and discussion	29
1.5 Uncertainty propagation for rare event estimation	31
1.5.1 Problem statement	31
1.5.2 Rare event estimation methods	34
1.5.3 Summary and discussion	43
1.6 Global sensitivity analysis	45
1.6.1 Screening methods	46
1.6.2 Variance-based importance measures	47
1.6.3 Moment-independent importance measures	50
1.6.4 Summary and discussion	52
1.7 Surrogate modeling	52
1.7.1 Common framework	52

1.7.2	General purposes surrogate model	54
1.7.3	Goal-oriented active surrogate model	56
1.7.4	Summary and discussion	60
1.8	Conclusion	60
2	Introduction to wind turbine modeling and design	61
2.1	Introduction	62
2.2	Metocean conditions simulation	62
2.2.1	Turbulent wind generation	63
2.2.2	Wake modeling	66
2.2.3	Irregular wave generation	67
2.3	Wind turbine multi-physics modeling	68
2.3.1	Aerodynamics of horizontal axis wind turbines	69
2.3.2	Hydrodynamics	71
2.3.3	Control	72
2.3.4	Structural dynamics	72
2.3.5	Fatigue damage	73
2.4	Design and operation practices	76
2.4.1	Types of technologies and preliminary design	77
2.4.2	Further design considerations	78
2.5	Uncertain inputs	81
2.5.1	Environmental inputs	82
2.5.2	System inputs	82
2.5.3	Probabilistic fatigue assessment	83
2.6	Conclusion	85
II	Contributions to uncertainty quantification and propagation	87
3	Kernel-based uncertainty quantification	89
3.1	Introduction	90
3.2	Dependence modeling with nonparametric copula	91
3.2.1	Preliminary definitions and properties	92
3.2.2	Empirical and checkerboard copula	94
3.2.3	Empirical Bernstein and Beta copula	94
3.3	<i>Copulogram</i> : a tool for multivariate data visualization	99
3.3.1	From pairwise plot to copulogram	99
3.3.2	Implementation in a Python package	99
3.4	Semiparametric inference of the South Brittany metocean conditions	102
3.4.1	Inference of the marginals	102
3.4.2	Nonparametric inference of the dependence	102

3.4.3	Goodness-of-fit and discussion	102
3.5	Quantifying and clustering the wake-induced perturbations within a wind farm	105
3.5.1	Uncertainty propagation in a wake model	106
3.5.2	Statistical metric of wake-induced perturbations	107
3.5.3	Summary and discussion	110
3.6	Conclusion	111
Bibliography		113

List of Figures

1	General uncertainty quantification framework (de Rocquigny et al. (2008), adapted by Ajenjo (2023))	3
1.1	Samples of three joint distributions with identical marginals and different dependence structures	18
1.2	Ranked samples represented in the Fig. 1.1	18
1.3	Univariate quadratures nodes for increasing sizes ($1 \leq n \leq 15$)	22
1.4	Two identical univariate Gauss-Legendre quadratures combined as a tensor product (left) and a Smolyak sparse grid (right).	23
1.5	Nested Monte Carlo and quasi-Monte Carlo designs ($n = 256$)	26
1.6	Latin hypercube designs with poor and optimized space-filling properties ($n = 8$)	29
1.7	One-dimensional reliability analysis example	32
1.8	FORM and SORM approximation on a two-dimensional reliability problem	35
1.9	Multi-FORM approximation on an example with two MPFPs	36
1.10	Illustration of a rare event estimation.	39
1.11	Illustration of a rare event estimation by subset sampling ($n = 4 \cdot 10^4, p_0 = 0.1$).	44
1.12	Illustration of a k -fold cross-validation (with $k = 4$)	54
1.13	Illustration of an ordinary kriging model fitted on a limited set of observations ($n = 7$). The predictor is represented in and several trajectories of the conditioned Gaussian process are drawn represented in purple.	56
1.14	Illustration of the expected improvement learning criterion	58
1.15	Illustration of the deviation number learning criterion	59
2.1	Wind spectrum from Brookhaven, USA (source: Burton et al. 2021)	63
2.2	[Should we keep this representation? If so, it will be done properly.]	64
2.3	Example of a turbulent wind field generated by TurbSim (source: Jonkman 2009)	65
2.4	Illustration of the wake created downstream a wind farm (source: Veers et al. 2019)	66
2.5	Peirson-Moskowitz and JONSWAP spectra at significant wave height $H_s = 3$ m and peak period $T_p = 7$ s (source: Milano 2021)	67
2.6	Chained numerical model of offshore wind turbine.	68

2.7	Hierarchy of structural (a) and aerodynamic (b) wind energy systems models (source: Veers et al. 2019)	69
2.8	Actuator disk model of the energy extraction (source: Burton et al. 2021). Longitudinal evolution of the air pressure and wind speed along the wind stream.	70
2.9	Blade element forces. With the lift and drag forces L and D , the flow angle ϕ , the pitch angle β and the angle of attack α (source: Burton et al. 2021).	71
2.10	Illustration of a soft-stiff design strategy, placing the structure's natural frequency f_0 away from the wind and wave power spectra, and the rotor excitation frequencies f_{1P} and f_{3P} (source: Kallehave et al. 2015).	73
2.11	Illustration of the Haigh diagram representing the combination of stress mean and amplitude leading to the same fatigue endurance.	76
2.12	Main offshore wind turbine technologies (sources: Ahmed et al. 2015; Mei and Xiong 2021).	78
2.13	Diagrams of an offshore wind turbine structure (source: (Chen et al., 2018)) and nacelle (source: US ODE).	79
2.14	Illustration of a probabilistic S-N curve according to the model defined in Guédé et al. (2007).	84
3.1	Evolution of m_{IMSE} for different dimensions and sample sizes.	97
3.2	Bernstein approximations of the empirical copula C_n (with size $n = 10$) of a Clayton copula (with parameter $\theta = 2.5$). The polynomial orders are assumed equal in the two dimensions $m_1 = m_2 \in \{3, 10, 20\}$	98
3.3	Copulogram of the iris flower dataset with colors assigned by the iris species.	101
3.4	Copulogram of Monte Carlo sample (with size $n = 10^3$) of the inputs and outputs of the modified Ishigami problem.	101
3.5	Marginal inference results of the South Brittany metocean data.	103
3.6	South Brittany wind farm layout (left). South Brittany wind rose from the ANEMOC data (right, source: ?).	106
3.7	Joint perturbation at WT 13, 19, and 25	108
3.8	Ambient and wake-disturbed distributions of the wind speed	108
3.9	Ambient and wake-disturbed distributions of the turbulence intensity	108
3.10	Kernel mean embedding of two probability distributions P and Q mapped in the RKHS H_k	109
3.11	South Brittany layout and wake effects measured by the squared MMD on wind conditions. Note that the vertical direction on this plot does not represent the north direction.	110
3.12	Convergence of the squared MMD estimation	111

List of Tables

2.1	S-N curve numerical values of welded tubular joints in different environmental conditions (source: DNV-RP-C203 2016)	75
2.2	Marginal distributions of the environmental random variables	83
2.3	Marginal distributions of the system random variables	83
3.1	Marginal inference results of the South Brittany metocean data.	103

Introduction

Industrial context and motivation

The current challenge of energy transition involves, among other things, reducing the share of fossil fuels in the global electricity mix. In this context, offshore wind energy offers several advantages ([Beauregard et al., 2022](#)). Offshore energy benefits from more consistent winds than onshore, mainly due to the absence of terrain roughness, it also makes possible the installation of larger and more powerful wind turbines. Since the construction of the first offshore wind farm in Vindeby, Denmark, in 1991, the industry has experienced rapid growth, with a total capacity of 56 GW in operation worldwide in 2021. Over time, offshore wind technology has matured, resulting in significant achievements such as securing projects in Europe through “zero-subsidy bids” where the electricity produced is directly sold on the wholesale market ([Beauregard et al., 2022](#)).

However, despite the progress of this sector, scaling limitations and numerous scientific challenges emerge. To meet ambitious national and regional development targets, the wind energy industry must address various scaling issues, including port logistics, the demand for critical natural resources, and sustainable end-of-life processes. Furthermore, the field presents several scientific challenges that often involve coupling data with numerical simulations of physical systems and their surrounding environment. The wind energy community is focused on different objectives, including enhancing the design of floating offshore wind turbines, refining wind resource estimation techniques, and optimizing maintenance operations. In general, several decisions are made throughout the lifespan of a wind turbine by its designer, installer, and operator, all while having only partial knowledge of certain physical phenomena. Therefore, modeling and controlling the various sources of uncertainties associated with offshore wind energy proved to be a key success factor in this highly competitive industry.

Overall, the offshore wind industry needs methods for uncertainty management regarding safety margins and industrial asset management (at the component, wind turbine, and overall wind farm levels) ([Van Kuik et al., 2016](#)). For wind project developers, the primary focus is on improving the wind potential assessment of candidate sites by combining various sources of information and modeling the multivariate distribution of environmental conditions. In the case of floating wind projects, the goal is to incorporate a probabilistic aspect from the design phase

(e.g., of the floaters) to define safer, more robust, and more cost-effective solutions. For wind farm owners, end-of-life management is another significant concern. An owner of a wind farm at the end of its life has three options: extend the operational life of assets, replace current wind turbines with newer models, or decommission and sell the wind farm. The first two options require evaluating the structural reliability and residual lifespan, with quantitative assessments reviewed by certification bodies and insurers to issue operating permits. To provide rigorous risk assessments, the generic methodology of *uncertainty quantification methodology* is a widely accepted approach in industrial sectors facing these types of issues ([de Rocquigny et al., 2008](#)).

Generic methodology for uncertainty quantification

Computer experiment is a discipline that emerged with the advent of informatics. This practice produces numerical models that allow the simulation of complex system behavior based on initial conditions defined by the analyst. Numerical models quickly became essential for the analysis, design, and certification of complex systems in cases where experiments or physical measurements are too costly or even unfeasible. However, such numerical models are mostly deterministic: the reproducible result of a simulation is associated with a fixed input set of parameters. The issue of managing uncertainties associated with these inputs arises when performing analysis with numerical models.

Uncertainty quantification aims at modeling and controlling uncertainties around a numerical model. To do so, a generic methodology has been proposed to quantify and analyze uncertainties between input and output variables of a numerical model ([de Rocquigny et al., 2008](#)). An overview of the mathematical tools used in this field is provided by [Sullivan \(2015\)](#). This approach improves the understanding of a system, ultimately contributing to more robust decision-making. Figure 1 illustrates the main step of the generic uncertainty quantification method, which are briefly summarized hereafter:

- **Step A – Problem specification:** This step involves identifying the system under study and constructing a numerical model capable of precisely simulating its behavior. Specifying the problem also involves the definition of a set of parameters inherent to the numerical model. These parameters include both the input variables and the output variables generated by the simulation. In this document, the numerical model is considered a black box, in contrast to approaches that are integrated within the numerical solution schemes for the system's behavioral equations (referred to as intrusive approaches ([Le Maître and Knio, 2010](#))). Generally, these numerical models are first calibrated against measured data and pass a process of validation and verification to reduce modeling errors ([Oberkampf and Roy, 2010](#)).
- **Step B – Uncertainty modeling:** The objective of the second step is to identify and model all the sources of uncertainty related to the input variables. Most of the time the uncertainty modeling is done in the probabilistic framework.

- **Step C – Uncertainty propagation:** This step consists in propagating the uncertain inputs through the computer model. Consequently, the output of the numerical model (commonly scalar) also becomes uncertain. The goal is to estimate a quantity of interest, which is a statistic related to the studied random output variable. The uncertainty propagation method may differ depending on the quantity of interest targeted (e.g., central tendency, a quantile, a rare event probability, etc.).
- **Step C' – Inverse analysis:** In this additional step, a sensitivity analysis can be performed to study the role allocated to each uncertain input leading to the uncertain output.
- **Metamodeling:** Considering the high computational cost associated with some simulations, statistical approaches emulate these expensive simulators with a limited number of simulations. Uncertainty quantification can then be carried out using a “surrogate model” (or metamodel) for a reduced computational cost. This optional step of statistical learning is not strictly a part of uncertainty quantification, but it often proves to be essential for enabling its practical implementation.

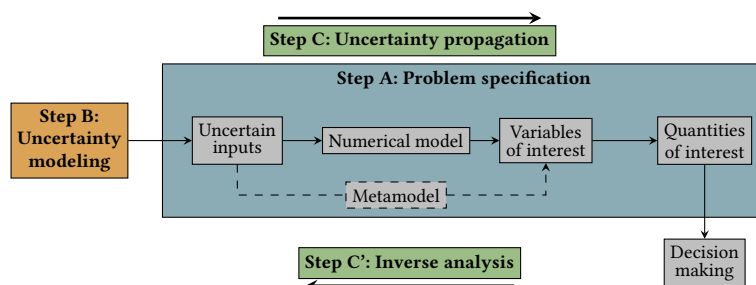


Figure 1 General uncertainty quantification framework ([de Rocquigny et al. \(2008\)](#), adapted by [Ajenjo \(2023\)](#))

Problem statement and outline of the thesis

Risk and uncertainty management in the field of wind energy is a significant concern for the electric utility Électricité de France (EDF). This thesis aims at adapting and applying the generic uncertainty quantification methodology to industrial offshore wind energy studies. As such, this use case raises scientific challenges related to its specific characteristics, described in the following:

- The numerical model exploited in the present work consists of a series of numerical models executed sequentially. This chain is divided into three parts: first, a temporal and stochastic generation of wind and wave velocity fields, followed by the simulation of the coupled hydro-aero-servo-elastic behavior of the wind turbine, and finally a post-processing phase to obtain scalar quantities of interest, aggregated over the temporal outputs.

- The complexity of this simulator, along with the high unit computational cost (about 40 minutes per simulation), requires the use of efficient sampling methods and high-performance computing systems. In addition to the complexity associated with the numerical model, modeling the input uncertainties also represents a challenge. Indeed, the joint distribution associated to environmental conditions present a complex dependence structure. The quality of the inference step is critical as it directly impacts the conclusions of uncertainty propagation.

In order to apply the generic methodology for uncertainty quantification to the offshore wind turbine case, this thesis aims at answering the following questions:

- Q1.** *How to accurately model the dependence structure associated with the joint environmental distribution?* (⇒ Step B)
- Q2.** *How to perform uncertainty propagation through a computationally expensive numerical chain uniquely based on an empirical description (measured data) of input uncertainties?* (⇒ Step C)
- Q3.** *How to estimate rare event probabilities related to the fatigue failure of offshore wind turbine structures?* (⇒ Step C)
- Q4.** *How to assess and analyse the sensitivity of uncertain inputs regarding quantities of interest resulting from structural reliability (i.e., reliability-oriented sensitivity analysis)?* (⇒ Step C')

To propose an answer to these questions, this manuscript is divided into three parts. The first part offers an introduction to uncertainty quantification methods and offshore wind turbine numerical modeling. The second part presents the contributions of this thesis to uncertainty quantification and propagation while the third part describes the contributions to rare event estimation. This manuscript is divided into seven chapters, which are summarized hereafter:

Chapter 1 – Introduction to uncertainty quantification. This chapter gives a brief overview of various topics in uncertainty quantification ([Sullivan, 2015](#)). After a reminder of some mathematical concepts, the model specification step is described, considering a black box and its input and output variables. The different types and sources of uncertainties are then presented, along with their modeling within a probabilistic framework. Uncertainty propagation depends on the estimated quantities of interest, therefore, one section addresses propagation methods for central tendency studies, and another focuses on rare event probability estimation (a statistic related to the tails of output distributions). The section dedicated to central tendency presents numerical integration, sampling, and design of experiments methods ([Fang et al., 2018](#)). The one about rare event probabilities introduces usual methods from the field of structural reliability ([Lemaire, 2013; Morio and Balesdent, 2015](#)).

This chapter also covers the main methods for global sensitivity analysis ([Da Veiga et al., 2021](#)). This field divides its methods into two major classes: screening methods and importance

measures. Screening techniques, typically applied in high-dimensional problems, aim to identify variables with low impact on the variability of the output of interest. Importance measures, on the other hand, quantitatively allocate, for each input variable, a share of the output variability, enabling the ranking of variables based on their influence.

Finally, this chapter presents an overview of the families of metamodels commonly used in uncertainty quantification ([Forrester et al., 2008](#)). Special attention is given to the Gaussian process regression, which involves conditioning a Gaussian process on a set of observations from the numerical model. Once conditioned, the Gaussian process provides richer information than other types of metamodels. This method simultaneously offers a surrogate model (mean of the Gaussian process, also called predictor) and an error function (variance of the process). Some iterative methods (called “active”) use this additional information to progressively enrich the metamodel and improve its predictability. These techniques were quite successful in the 1990s for solving optimization problems with expensive functions ([Jones et al., 1998](#)). Since then, their use has expanded to solve problems in structural reliability [Echard et al. \(2011\)](#).

Chapter 2 – Introduction to wind turbine modeling and design. The simulation of an offshore wind turbine involves modeling multiple physical aspects interacting with random environmental conditions. This chapter first introduces spectral methods used to generate wind and wave velocity fields by applying inverse Fourier transforms (e.g., as implemented in the TurbSim tool ([Jonkman, 2009](#))). These simulated wind velocity fields then become the inputs of a multi-physics wind turbines numerical model. Such simulation includes a simplified modeling of the interactions between fluids and structures (using the blade element momentum theory), dynamic modeling of the structure using flexible multibody methods, and modeling of wind turbine control systems [source]. The numerical code studied generates time series of several physical quantities describing the system’s behavior.

This thesis particularly focuses on the probabilistic evaluation of fatigue damage in wind turbine structures. Fatigue damage is a phenomenon that deteriorates the mechanical properties of a material as a result of exposure to many of cyclic, low-amplitude stresses. Currently, standards recommend the use of deterministic safety factors to address this failure mode ([IEC-61400-1, 2019](#); [DNV-ST-0437, 2016](#)). A probabilistic approach enhances the analysis and can sometimes reveal conservative of safety margins. Several recent studies have addressed this topic from different methodological perspectives ([Huchet, 2019](#); [Lataniotis, 2019](#); [Cousin, 2021](#); [Hirvoas, 2021](#); [Petrovska, 2022](#)).

In this context, this chapter enumerates the input parameters of the calculation chain that are considered uncertain. These random variables are grouped into two groups: the random vector related to the environment (e.g., average wind speed, wind speed standard deviation, wind direction, significant wave height, wave period, and wave direction), and the random vector related to the system (e.g., controller wind misalignment error, soil stiffness, fatigue calculation curve parameters).

Chapter 3 – Kernel-based uncertainty quantification. This chapter examines perturbations in environmental conditions within an offshore wind farm induced by wake effects [Larsen et al. \(2008\)](#). A theoretical offshore wind farm off the southern coast of Brittany is considered as a use case, and a simplified numerical model of wake in this wind farm is used. This model provides an analytical prediction of the wind speed deficit and turbulence created by the wake, taking into account the influence of the floaters' positions due to rigid body dynamics.

In a second phase, uncertainty propagation is carried out thought the wake model, considering the joint distribution of ambient environmental conditions as inputs. In the end, an environmental distribution perturbed by the wake is simulated for each wind turbine. A dissimilarity measure between distribution, based of kernels and named the *maximum mean discrepancy* (MMD), is used to compare the distributions perceived by each wind turbine. This measure allows the clustering of wind turbines exposed to similar environmental conditions, resulting in identical structural responses. Given the high computational cost of aero-servo-hydro-elastic simulations for offshore wind turbines, this preliminary study enables reliability analysis at the wind farm scale without repeating the analysis for each turbine. Ultimately, only four classes are selected to represent a wind farm of 25 turbines.

Chapter 4 – Kernel-based central tendency estimation. Chapter four presents the use of the kernel-based dissimilarity measure (MMD) in the context of probability distribution sampling, a method known as "kernel herding" introduced by [Chen et al. \(2010\)](#). This quadrature technique belongs to the family of "Bayesian quadratures" [Briol et al. \(2019\)](#), which can be viewed as a generalization of quasi-Monte Carlo methods [Li et al. \(2020\)](#).

The properties of this method are highlighted through an industrial application dedicated to estimating the mean fatigue damage of a wind turbine structure. Although this quantity is crucial in the design and certification of wind turbines, the methods used to estimated it are known to be suboptimal (i.e., regular grids). The study is conducted on a model of a fixed offshore wind turbine belonging to a farm in the North Sea. Uncertainties in input environmental conditions are inferred from in-situ measured data.

Finally, a numerical comparison with Monte Carlo and quasi-Monte Carlo sampling reveals the performance and practical advantages of kernel herding. This method allows for direct subsampling from a large environmental database without the need for inference (step B).

Chapter 5 – Kernel-based metamodel validation. This chapter proposes the use of kernel-based sampling methods in the context of model validation for machine learning (or surrogate models). Estimating the predictivity of supervised learning models requires an evaluation of the learned surrogate model on a set of test points that were not used during training. The quality of the validation naturally depends on the properties of the test set and the metric used to summarize the prediction error. This contribution first suggests using space-filling sampling methods to "optimally" select a test set, then, it introduces a new predictivity coefficient that weights the observed errors to improve the global error estimation. A numerical comparison between several sampling methods based on geometric approaches ([Shang and Apley, 2020](#)) or

kernel methods [Chen et al. \(2010\)](#); [Mak and Joseph \(2018\)](#) is carried out. Our results show that weighted versions of kernel methods offer superior performance. An application to simulated mechanical loads in an offshore wind turbine model is also presented. This experiment illustrates the practical relevance of this technique as an effective alternative to costly cross-validation techniques.

Chapter 6 – Nonparametric rare event estimation. Estimating rare events probabilities is a common issue in industrial risk management, especially in the field of structural reliability ([Chabridon, 2018](#)). To address this, several techniques have been proposed to overcome the known limitations of the Monte Carlo method. Among them, “subset sampling” ([Au and Beck, 2001](#)) is a technique based on the split of a rare probability into a product of less rare (and thus easier to estimate) conditional probabilities associated with nested failure events. However, this technique relies on conditional simulation using Markov chain Monte Carlo (MCMC) methods. These algorithms, while converging, often produce samples that are not independent and identically distributed (i.i.d.) due to the correlation between the Markov chains. In this chapter another conditional sampling method is proposed, with the advantage of preserving the i.i.d. property. Independent sampling is particularly relevant for reusing these samples in a posterior reliability-oriented sensitivity analysis. The algorithm introduced is based on the non-parametric inference of the conditional joint distribution using kernel density estimation of marginals combined with dependence inference using the empirical Bernstein copula ([Sancetta and Satchell, 2004](#)). The so-called “Bernstein adaptive nonparametric conditional sampling” (BANCS), is compared to the subset sampling method for several structural reliability problems. The initial results are promising, but further investigation is needed to control the estimator’s bias.

Chapter 7 – Sequential reliability oriented sensitivity analysis. This chapter deals with sensitivity analysis for risk measures (e.g., rare event probabilities). Global sensitivity analysis ([Da Veiga et al., 2021](#)) assigns a portion of the global output variability to each variable (or group of variables), often using a functional decomposition of the output variance. However, when studying risk measure (often located in the distributions’ tails), the global sensitivity might be very different to the sensitivity to the risk measure. “Reliability-oriented sensitivity analysis” (ROSA), studies the impact of the inputs in regard to a risk-measure such as a rare event probability (see e.g., [Chabridon \(2018\)](#)). Using the nested subsets obtained with the BANCS algorithm (presented in Chapter 6), the idea of this chapter is to study the ROSA evolution as the subsets get closer to the failure domain. For each subset, a ROSA is carried out with a kernel-based importance measure called the “Hilbert-Schmidt Independence Criterion” adapted to this context ([Marrel and Chabridon, 2021](#)).

Numerical developments

Several implementations developed in this thesis are available on different platforms, allowing the reader to reproduce some numerical results in an open-data approach:

- This Python package generates designs of experiments based on kernel methods such as Kernel Herding and Support Points. A tensorized implementation of the algorithms was proposed, significantly increasing their performances. Additionally, optimal weights for Bayesian quadrature are provided.

- This Python package, developed in collaboration with J.Muré, is available on the platform Pypi and fully documented.

-
- This Python package proposes an implementation of the “Bernstein Adaptive Non-parametric Conditional Sampling” method for rare event estimation.

- bancs²
- This Python package is available on the PyPI platform and is illustrated with examples and analytical benchmarks.

-
- This Python package presents a standardized process to benchmark different sampling methods for central tendency estimation.

- ctbenchmark³
- This Python package is available on a GitHub repository with analytical benchmarks.

-
- This Python package proposes an implementation of a synthetic visualization tool for multivariate distributions.

- copulogram⁴
- This Python package, developed in collaboration with V.Chabridon, is available on the Pypi platform.

¹Documentation: <https://efekhari27.github.io/otkerneldesign/master/>

²Repository: <https://github.com/efekhari27/bancs>

³Repository: <https://github.com/efekhari27/ctbenchmark>

⁴Repository: <https://github.com/efekhari27/copulogram>

Publications and communications

The research contributions in this manuscript are based on the following publications:

Book Chap.	<u>E. Fekhari</u> , B. Iooss, J. Muré, L. Pronzato and M.J. Rendas (2023). “Model predictivity assessment: incremental test-set selection and accuracy evaluation”. In: <i>Studies in Theoretical and Applied Statistics</i> , pages 315–347. Springer.
Jour Pap.	<u>E. Fekhari</u> , V. Chabridon, J. Muré and B. Iooss (2023). “Given-data probabilistic fatigue assessment for offshore wind turbines using Bayesian quadrature”. In: <i>Data-Centric Engineering</i> .
Int. Conf	<u>E. Fekhari</u> , B. Iooss, V. Chabridon, J. Muré (2022). “Numerical Studies of Bayesian Quadrature Applied to Offshore Wind Turbine Load Estimation”. In: <i>SIAM Conference on Uncertainty Quantification (SIAM UQ22)</i> , Atlanta, USA. (Talk)
	<u>E. Fekhari</u> , B. Iooss, V. Chabridon, J. Muré (2022). “Model predictivity assessment: incremental test-set selection and accuracy evaluation”. In: <i>22nd Annual Conference of the European Network for Business and Industrial Statistics (ENBIS 2022)</i> , Trondheim, Norway. (Talk)
	<u>E. Fekhari</u> , B. Iooss, V. Chabridon, J. Muré (2022). “Efficient techniques for fast uncertainty propagation in an offshore wind turbine multi-physics simulation tool”. In: <i>Proceedings of the 5th International Conference on Renewable Energies Offshore (RENEW 2022)</i> , Lisbon, Portugal. (Paper & Talk)
	<u>E. Fekhari</u> , V. Chabridon, J. Muré and B. Iooss (2023). “Bernstein adaptive nonparametric conditional sampling: a new method for rare event probability estimation” ⁵ . In: <i>Proceedings of the 13th International Conference on Applications of Statistics and Probability in Civil Engineering (ICASP 14)</i> , Dublin, Ireland. (Paper & Talk)
	<u>E. Vanem</u> , <u>E. Fekhari</u> , N. Dimitrov, M. Kelly, A. Cousin and M. Guiton (2023). “A joint probability distribution model for multivariate wind and wave conditions”. In: <i>Proceedings of the ASME 2023 42th International Conference on Ocean, Offshore and Arctic Engineering (OMAE 2023)</i> , Melbourne, Australia. (Paper)
	<u>A. Lovera</u> , <u>E. Fekhari</u> , B. Jézéquel, M. Dupoirion, M. Guiton and E. Ardillon (2023). “Quantifying and clustering the wake-induced perturbations within a wind farm for load analysis”. In: <i>Journal of Physics: Conference Series (WAKE 2023)</i> , Visby, Sweden (Paper)
Nat. Conf.	<u>E. Fekhari</u> , B. Iooss, V. Chabridon, J. Muré (2022). “Kernel-based quadrature applied to offshore wind turbine damage estimation”. In: <i>Proceedings of the Mascot-Num 2022 Annual Conference (MASCOT NUM 2022)</i> , Clermont-Ferrand, France (Poster)
	<u>E. Fekhari</u> , B. Iooss, V. Chabridon, J. Muré (2023). “Rare event estimation using nonparametric Bernstein adaptive sampling”. In: <i>Proceedings of the Mascot-Num 2023 Annual Conference (MASCOT-NUM 2023)</i> , Le Croisic, France (Talk)

⁵This contribution was rewarded by the “CERRA Student Recognition Award”

PART I:

INTRODUCTION TO UNCERTAINTY QUANTIFICATION AND WIND ENERGY

Toute pensée émet un coup de dé.

S. MALLARMÉ

Chapter **1**

Uncertainty quantification in computer experiments

1.1	Introduction	14
1.2	Black-box model specification	14
1.3	Enumerating and modeling the uncertain inputs	15
1.3.1	Sources of the input uncertainties	15
1.3.2	Modeling uncertain inputs with the probabilistic framework	16
1.3.3	Joint input probability distribution	17
1.4	Uncertainty propagation for central tendency study	20
1.4.1	Numerical integration	20
1.4.2	Numerical design of experiments	26
1.4.3	Summary and discussion	29
1.5	Uncertainty propagation for rare event estimation	31
1.5.1	Problem statement	31
1.5.2	Rare event estimation methods	34
1.5.3	Summary and discussion	43
1.6	Global sensitivity analysis	45
1.6.1	Screening methods	46
1.6.2	Variance-based importance measures	47
1.6.3	Moment-independent importance measures	50
1.6.4	Summary and discussion	52
1.7	Surrogate modeling	52
1.7.1	Common framework	52
1.7.2	General purposes surrogate model	54
1.7.3	Goal-oriented active surrogate model	56
1.7.4	Summary and discussion	60
1.8	Conclusion	60

1.1 Introduction

The progress of computer simulation gradually allows the virtual resolution of more complex problems in scientific fields such as physics, astrophysics, engineering, climatology, chemistry, or biology. This domain often provides a deterministic solution to complex problems depending on several inputs. Associating an uncertainty quantification (UQ) analysis with these numerical models is a key element to improving the understanding of the phenomena studied. A wide panel of UQ methods has been developed over the years to pursue these studies for a reasonable computational cost.

This chapter presents the essential tools and methods from the generic UQ framework, including elements partially inspired from [Sullivan \(2015\)](#) and [Chabridon \(2018\)](#). It is structured as follows: Section 1.2 describes the context of the model specification step; Section 1.3 presents a classification of the inputs uncertainties and the probabilistic framework to model them; Section 1.4 and 1.5 introduce various methods to propagate the input uncertainties through the numerical model for different purposes; Section 1.6 presents the main inverse methods to perform sensitivity analysis in our framework; Finally, 1.7 introduces the concept of surrogate models to emulate a model by realizing a statistical learning on a limited dataset.

OpenTURNS¹. Is a high-performance Python library dedicated to UQ ([Baudin et al., 2017](#)). OpenTURNS (“Open source initiative for the Treatment of Uncertainties, Risks’N Statistics”) is developed by industrial researchers from EDF R&D, Airbus Group, PHIMECA Engineering, IMACS and ONERA. It combines high-performance using C++ programming with high-accessibility through a Python API. Overall, this open source library provides tools for various steps of the UQ framework (e.g., uncertainty quantification, uncertainty propagation, surrogate modeling, reliability, sensitivity analysis and calibration). To guaranty software quality, the development follows robust processes such as exhaustive unit testing and multiplatform continuous integration. A dedicated forum hosts an active community, which is helping new users and discussing future developments. Finally, no-code users can benefit from OpenTURNS’s free-download Graphical User Interface software, named [Persalys](#)². In this chapter, the methodological concepts introduced are linked to minimal OpenTURNS implementations examples, available in the Appendix ??.

1.2 Black-box model specification

In our computer experiments context, uncertainty quantification is performed around an input-output numerical simulation model. This numerical model, or code, is hereafter considered as *black-box* since the knowledge of the underlying physics doesn’t inform the UQ methods. Alternatively, one could consider *intrusive* UQ methods, introducing uncertainties within the

¹OpenTURNS installation guide and documentation are available at <https://openturns.github.io/www/>

²Persalys, a free-download graphical user interface available at <https://www.persalys.fr/obtenir.php>

resolution of the equations of the physics (see e.g., [Le Maître and Knio 2010](#)). In practice, numerical models might be a sequence of codes executed in series to obtain a variable of interest.

While simulation models are in most cases deterministic, they may also be qualified as intrinsically stochastic (i.e., two runs of the same model taking the same inputs return different outputs). Additionally, numerical simulation always presents modeling errors. In the following, it will be assumed that the numerical models passed a *validation & verification* phase, to quantify their confidence and predictive accuracy.

Formally, part of the problem specification is the definition of the set of d input variables $\mathbf{x} = (x_1, \dots, x_d)^\top$ considered as uncertain (e.g., wind speed, wave period, etc.). The outputs studied are also defined at this stage, which will only be of scalar type in the present work. UQ methods suited to other types of outputs exist (see e.g., for time series outputs [Lataniotis 2019](#), for functional outputs [Audet et al. 2012; Rollón de Pinedo et al. 2021](#)). Let us then define the following numerical model:

$$\mathcal{M} : \begin{cases} \mathcal{D}_x \subseteq \mathbb{R}^d & \longrightarrow \mathcal{D}_y \subseteq \mathbb{R} \\ \mathbf{x} & \longmapsto y. \end{cases} \quad (1.1)$$

Unlike the typical machine learning input-output dataset framework, the UQ analyst can simulate the output image of any inputs (in the input domain), using a numerical model. However, numerical simulations often come with an important computational cost. Therefore, UQ methods should be efficient and require as few simulations as possible. In this context, surrogate models (or metamodels) are statistical approximations of the costly numerical model, that can be used to perform tractable UQ. Surrogate models are built and validated on a limited number of simulations (in a *supervised learning* framework). In practice, note that the model specification step is often associated with the development of a *wrapper* of the code. It is an overlay of code allowing its execution in a parametric way, which is often associated with *high-performance computer* (HPC) deployment. Once the model is specified, a critical step in uncertainty quantification is enumerating the input uncertainties and building their associated mathematical model.

1.3 Enumerating and modeling the uncertain inputs

1.3.1 Sources of the input uncertainties

The analyst should construct a list of uncertain inputs as exhaustive as possible, to ensure a complete risk assessment (e.g., associated with the exploitation of a wind energy asset). Even if these uncertainties might have different origins, they should all be considered jointly in the UQ study. Authors proposed to classify them for practical purposes into two groups:

- **aleatory uncertainty** regroups the uncertainties arising from natural randomness (e.g., wind turbulence). From a risk management point of view, these uncertainties are qualified

as *irreducible* since the industrials facing them will not be able to acquire additional information to reduce them (e.g., additional measures).

- **epistemic uncertainty** gathers the uncertainties resulting from a lack of knowledge (e.g., material properties). Contrarily to the aleatory ones, epistemic uncertainties might be reduced by investigating their origin (often at a certain cost).

[Der Kiureghian and Ditlevsen \(2009\)](#) discuss the relevance of this classification. They affirm that this split is practical for decision-makers to identify possible ways to reduce their uncertainties. However, it should not affect the way of modeling or propagating uncertainties. In the following, the probabilistic framework is introduced to deal with uncertainties.

1.3.2 Modeling uncertain inputs with the probabilistic framework

Uncertainties are traditionally modeled with objects from the probability theory. In this thesis, the *probabilistic framework* is adopted. Alternative theories exist to mathematically model uncertainties. For example, imprecise probability theory allows more general modeling of the uncertainties ([Beer et al., 2013; Schöbi and Sudret, 2017](#)). It becomes useful when dealing with very limited and possibly contradictory information (e.g., expert elicitation). The core probabilistic tools and objects are introduced hereafter.

The *probability space* is a measure space with total measure summing to one, also called probability triple and denoted $(\Omega, \mathcal{A}, \mathbb{P})$. This mathematical concept first includes a sample space Ω , which contains a set of outcomes $\omega \in \Omega$. Note that an *event* is defined as a set of outcomes in the sample space. Then, a σ -algebra \mathcal{A} , also called event space, is a set of events. Finally, a probability function $\mathbb{P} : \mathcal{A} \rightarrow [0, 1]$, is a positive probability measure associated with an event. Most often, the choice of the probability space will not be specified. The main object will be functions defined over this probability space: random variables.

The *random vector* \mathbf{X} (i.e., multivariate random variable) is a measurable function defined as:

$$\mathbf{X} : \begin{cases} \Omega & \longrightarrow \mathcal{D}_{\mathbf{x}} \subseteq \mathbb{R}^d \\ \omega & \longmapsto \mathbf{X}(\omega) = \mathbf{x}. \end{cases} \quad (1.2)$$

In the following, the random vector \mathbf{X} will be considered to be a squared-integrable function against the measure \mathbb{P} (i.e., $\int_{\Omega} |\mathbf{X}(\omega)|^2 d\mathbb{P}(\omega) < \infty$). Moreover, the present thesis deals with continuous random variables.

The *probability distribution* of the random vector \mathbf{X} is the pushforward measure of \mathbb{P} by \mathbf{X} . Which is a probability measure on $(\mathcal{D}_{\mathbf{x}}, \mathcal{A})$, denoted $\mathbb{P}_{\mathbf{X}}$ and defined by:

$$\mathbb{P}_{\mathbf{X}}(B) = \mathbb{P}(\mathbf{X} \in B) = \mathbb{P}(\omega \in \Omega : \mathbf{X}(\omega) \in B), \quad \forall B \in \mathcal{A}. \quad (1.3)$$

The *cumulative distribution function* (CDF) is a common tool to manipulate random variables. It is a function $F_{\mathbf{X}} : \mathcal{D}_{\mathbf{x}} \rightarrow [0, 1]$ defined for all $\mathbf{x} \in \mathcal{D}_{\mathbf{x}}$ as:

$$F_{\mathbf{X}}(\mathbf{x}) = \mathbb{P}(\mathbf{X} \leq \mathbf{x}) = \mathbb{P}(X_1 \leq x_1, \dots, X_d \leq x_d) = \mathbb{P}_{\mathbf{X}}([-\infty, x_1] \times \dots \times [-\infty, x_d]). \quad (1.4)$$

The CDF is a positive, increasing, right-continuous function, which tends to 0 as \mathbf{x} tends to $-\infty$ and to 1 as \mathbf{x} tends to $+\infty$. In the continuous case, one can also define a corresponding *probability density function* (PDF) $f_{\mathbf{X}} : \mathcal{D}_{\mathbf{x}} \rightarrow \mathbb{R}_+$ with $f_{\mathbf{X}}(\mathbf{x}) = \frac{\partial^d F_{\mathbf{X}}(\mathbf{x})}{\partial x_1 \dots \partial x_d}$.

The expected value of a random vector $\mathbb{E}[\mathbf{X}]$, also called first moment, is a vector defined as:

$$\mu_{\mathbf{X}} = \mathbb{E}[\mathbf{X}] = \int_{\Omega} \mathbf{X}(\omega) d\mathbb{P}(\omega) = \int_{\mathcal{D}_{\mathbf{x}}} \mathbf{x} f_{\mathbf{X}}(\mathbf{x}) d\mathbf{x} = (\mathbb{E}[X_1], \dots, \mathbb{E}[X_d])^\top. \quad (1.5)$$

In addition, considering two random variables X_i and X_j , with $i, j \in \{1, \dots, d\}$, one can write their respective variance:

$$\text{Var}(X_i) = \mathbb{E}[(X_i - \mathbb{E}[X_i])^2], \quad (1.6)$$

and a covariance describing their joint variability:

$$\text{Cov}(X_i, X_j) = \mathbb{E}[(X_i - \mathbb{E}[X_i])(X_j - \mathbb{E}[X_j])]. \quad (1.7)$$

The *standard deviation* $\sigma_{X_j} = \sqrt{\text{Var}(X_j)}$ and *coefficient of variation* $\delta_{X_j} = \frac{\text{Var}(X_j)}{|\mathbb{E}[X_j]|}$ are two quantities directly associated to the two first moments.

1.3.3 Joint input probability distribution

This section introduces various techniques to model and infer a joint probability distribution (or multivariate distribution). It will first define the *copula*, a mathematical tool used to model the dependence structure of a joint distribution. Then, a few methods to fit a joint distribution over a dataset will be mentioned. Finally, a panel of tools to evaluate the goodness of fit between a probabilistic model and a dataset will be recalled.

In general, the single effects of multivariate distributions tend to be well modeled. However, modeling the dependence structure underlying in a joint distribution is often overlooked. To illustrate the importance of this step, Fig. 1.1 represents three i.i.d samples from three bivariate distributions sharing the same single effects (e.g., here two exponential distributions) but different dependence structures. Judging from this example, one can assume that the joint distribution results from the composition of the single effects, also called marginals, and an application governing the dependence between them.

An empirical way of isolating the dependence structures from this example is to transform the samples in the ranked space. Let us consider an n -sized sample $\mathbf{X}_n = \{\mathbf{x}^{(1)}, \dots, \mathbf{x}^{(n)}\} \in \mathcal{D}_{\mathbf{x}}^n$. The corresponding ranked sample is defined as: $\mathbf{R}_n = \{\mathbf{r}^{(1)}, \dots, \mathbf{r}^{(n)}\}$, where³ $r_j^{(i)} = \sum_{l=1}^n \mathbb{1}_{\{x_j^{(l)} \leq x_j^{(i)}\}}$, $\forall j \in \{1, \dots, d\}, i \in \{1, \dots, n\}$. Ranking a multivariate dataset allows us to isolate the dependence

³The *indicator function* is defined such that $\mathbb{1}_{\{\mathcal{A}\}}(x) = 1$ if $x \in \mathcal{A}$ and is equal to zero otherwise.

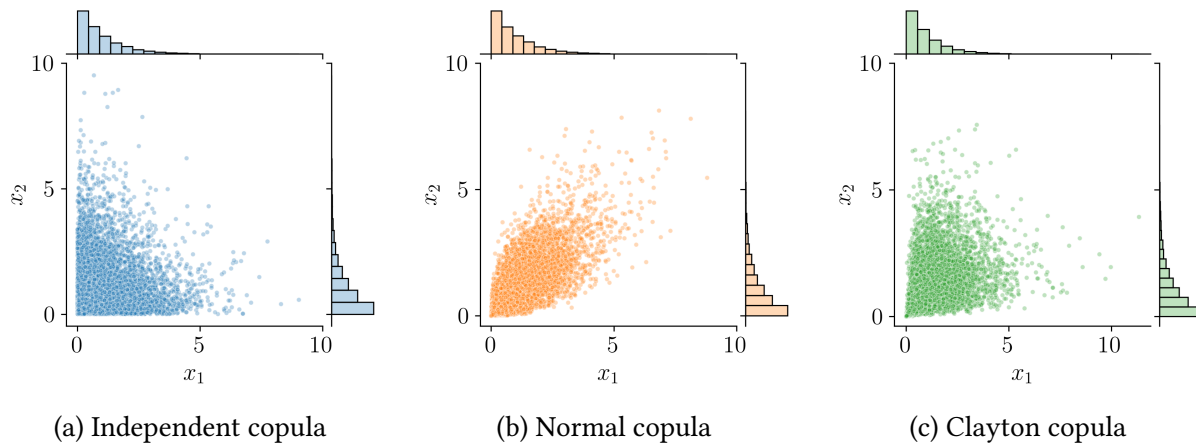


Figure 1.1 Samples of three joint distributions with identical marginals and different dependence structures

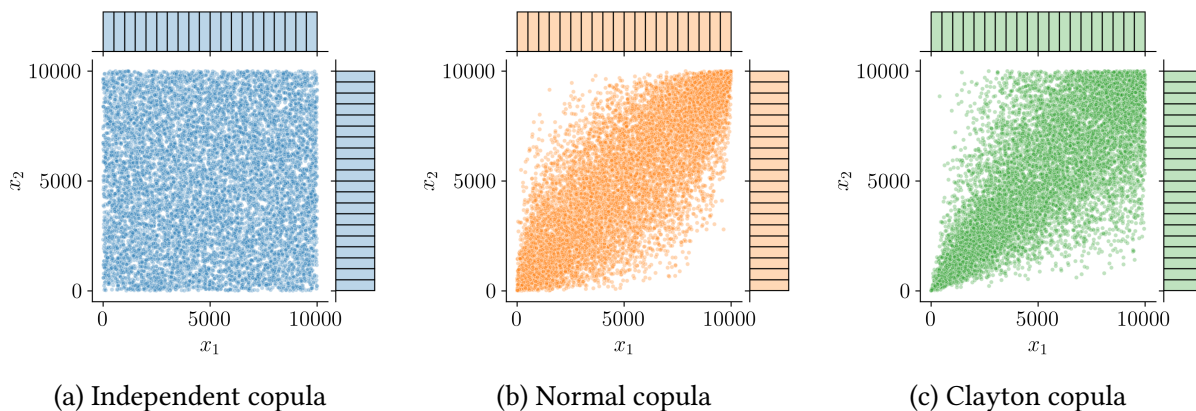


Figure 1.2 Ranked samples represented in the Fig. 1.1

structure witnessed empirically (Saporta, 2006). Fig. 1.2 shows the same three samples from Fig. 1.1 in the ranked space. One can first notice that the marginals are uniform since each rank is uniformly distributed. Then, the scatter plot from the distribution with independent copula (left plot) is uniform while the two others present different patterns.

A theorem states that the multivariate distribution of any random vector can be broken down into two objects (Joe, 1997). First, a set of univariate marginal distributions describing the behavior of the individual variables; Second, a function describing the dependence structure between all variables: a copula.

Theorem 1 (Sklar's theorem). *Let $\mathbf{X} \in \mathbb{R}^d$ be a random vector and its joint CDF $F_{\mathbf{X}}$ with marginals $\{F_{X_j}\}_{j=1}^d$, there exists a copula $C : [0, 1]^d \rightarrow [0, 1]$, such that:*

$$F_{\mathbf{X}}(x_1, \dots, x_d) = \mathbb{P}(X_1 \leq x_1, \dots, X_d \leq x_d) = C(F_{X_1}(x_1), \dots, F_{X_d}(x_d)). \quad (1.8)$$

If the marginals F_{X_i} are continuous, then this copula is unique. If the multivariate distribution has a PDF $f_{\mathbf{X}}$, it can also be expressed:

$$f_{\mathbf{X}}(x_1, \dots, x_d) = c(F_{X_1}(x_1), \dots, F_{X_d}(x_d)) \times f_{X_1}(x_1) \times \dots \times f_{X_d}(x_d), \quad (1.9)$$

where c is the density of the copula, sometimes also called copula by misuse of language. The reader might refer to [Durante and Sempi \(2015\)](#) for three different mathematical proofs.

Theorem 1 expresses the joint CDF by combining marginal CDFs and a copula, which is practical for sampling joint distributions. Conversely, the copula can be defined by using the joint CDF and the marginal CDFs:

$$C(u_1, \dots, u_d) = F_{\mathbf{X}}(F_{X_1}^{-1}(u_1), \dots, F_{X_d}^{-1}(u_d)) \quad (1.10)$$

This equation allows us to extract a copula from a joint distribution by knowing its marginals. Additionally, copulas are invariant under increasing transformations. This property is important to understand the use of rank transformation to display the copula without the marginal effects.

Identically to the univariate continuous distributions, a large catalog of families of copulas exists (e.g., independent, Normal, Clayton, Frank, Gumbel copula, etc.). Note that the independent copula Π implies that the distribution is defined as the product of its marginals $\Pi = \prod_{j=1}^d u_j$. In an inference context, this theorem divides the fitting problem into two independent problems: fitting the marginals and fitting the copula. Provided a dataset, this framework allows the potential combination of a parametric (or nonparametric) fit of marginals with a parametric (or nonparametric) fit of the copula.

To infer a joint distribution over a dataset, the analyst should determine a fitting strategy. Appropriate data visualization helps to choose the fitting methods susceptible to be relevant to the problem. In practice, the following points can be asked at this early stage:

- Is the distribution unimodal? If not, mixtures methods or nonparametric models might be required;
- Is the validity domain restrictive? If so, specific families of parametric distributions can be chosen or truncation can be applied;
- Is there a dependence structure? Does it concern all the variables together or only some groups of variables?
- Is the dependence structure complex? Transforming the dataset in the ranked space gives an empirical description of the dependence.

To ease the reading, a few techniques for estimating marginal distributions are available in Appendix ???. In addition, two nonparametric methods are introduced in Chapter 3 to infer a copula: the “empirical Bernstein copula” and the “Beta copula”. The adequation between a fitted probabilistic model and a dataset should be validated, therefore, Appendices ?? recall visual and quantitative tools for univariate goodness-of-fit evaluation.

OpenTURNS 1 (Bivariate distribution). The Python code available in Appendix ?? proposes a minimalistic OpenTURNS example of a probabilistic uncertainty modeling. Figures illustrating the present section may be reproduced, using the OpenTURNS scripts available on GitHub⁴.

1.4 Uncertainty propagation for central tendency study

The previous section aimed at building a probabilistic model of the uncertainties considering the knowledge available. This one introduces diverse methods for forward propagation of the input uncertainties through a numerical model. In the present section, uncertainty propagation is dedicated to the “central tendency” as its goal is to study the mean and variance of the output distribution. This approach contrasts with the uncertainty propagation committed to rare event probability estimation, which will be introduced in Section 1.5 (e.g., used to assess reliability).

The difficulties related to any uncertainty propagation mostly arise from the practical properties of the numerical model. Its potential high dimension, irregularity and nonlinearity each represent a challenge. Such studies rely on a finite number of observations of the numerical model, depending on the computational budget affordable. Uncertainty propagation is at the end of generic UQ approach (step C), however, it is affected by the “garbage in, garbage out” concept. Meaning that its conclusions depend on the accuracy of the inputs’ uncertainty modeling.

This section introduces the main methods of global uncertainty propagation, outlining the links between numerical integration (i.e., Lebesgue integration or central tendency estimation) and numerical design of experiments.

1.4.1 Numerical integration

Forward uncertainty propagation aims at integrating a measurable function $g : \mathcal{D}_X \rightarrow \mathbb{R}$ with respect to a probability measure \mathbb{P}_X . Numerical integration provides algorithmic tools to help the resolution of this probabilistic integration (i.e., Lebesgue integration). Note that the measurable function g , in the context of computer experiments, becomes the numerical model \mathcal{M} introduced in Eq. (1.1).

In practice, this integral is approximated by summing a finite n -sized set of realizations $\mathbf{y}_n = \{g(\mathbf{x}^{(1)}), \dots, g(\mathbf{x}^{(n)})\}$ from a set of input samples $\mathbf{X}_n = \{\mathbf{x}^{(1)}, \dots, \mathbf{x}^{(n)}\}$. A *quadrature* establishes a rule selecting the input samples \mathbf{X}_n (also called nodes), and an associated set of weights

⁴https://github.com/efekhari27/thesis/blob/main/numerical_experiments/chapter1/copulas.ipynb

$\mathbf{w}_n = \{w_1, \dots, w_n\} \in \mathbb{R}^n$. The approximation given by a quadrature rule is defined as a weighted arithmetic mean of the realizations:

$$I_{\mathbb{P}_X}(g) := \int_{\mathcal{D}_X} g(\mathbf{x}) d\mathbb{P}_X(\mathbf{x}) \approx \sum_{i=1}^n w_i g(\mathbf{x}^{(i)}). \quad (1.11)$$

For a given sample size n , the goal is to find a set of tuples $\{\mathbf{x}^{(i)}, w_i\}_{i=1}^n$ (i.e., quadrature rule), giving the best approximation of our quantity. Ideally, the approximation quality should be fulfilled for a wide class of integrands. Most quadrature rules only depend on the measure space $(\Omega, \mathcal{A}, \mathbb{P}_X)$, regardless of the integrand values. In the context of a costly numerical model, this property allows the analyst to massively distribute the calls to the numerical model.

This section aims at presenting the main multivariate integration techniques. These methods encompass different properties: some are deterministic and some are aleatory; some are sequential (i.e., nested) some are not; some are victims of the curse of dimensionality and some are not.

Classical multivariate deterministic quadrature

Historically, quadrature methods have been developed for univariate integrals. The Gaussian rule and the Fejér-Clebschaw-Curtis rule are two univariate deterministic quadratures that will be briefly introduced (see [Sullivan 2015](#) for further elements).

Gaussian quadrature is a powerful univariate quadrature building together a set of irregular nodes and a set of weights. The computed weights are positive, which ensures a numerically stable rule even for large sample sizes.

Different variants of Gaussian rules exist, the most common being the Gauss-Legendre quadrature. In this case, the function g to be integrated with respect to the uniform measure on $[-1, 1]$ is approximated by Legendre polynomials. Considering the Legendre polynomial of order n , denoted l_n , the quadrature nodes $x^{(i)}_{i=1}^n$ are given by the polynomial roots. The respective weights are given by the following formula:

$$w_i = \frac{2}{\left(1 - (x^{(i)})^2\right) (l'_n(x^{(i)}))^2}. \quad (1.12)$$

Gauss-Legendre quadrature guarantees a very precise approximation provided that the integrand is well-approximated by a polynomial of degree $2n - 1$ or less on $[-1, 1]$. This rule is deterministic but not sequential, meaning that two rules with sizes n_1 and n_2 , $n_1 < n_2$ will not be nested. However, a sequential extension is proposed by the Gauss-Kronrod rule ([Laurie, 1997](#)), at the expense of a slightly lower accuracy.

To overcome this practical drawback, Fejér then Clebschaw with Curtis proposed a nested rule with mostly equivalent accuracy as Gaussian quadratures. This method is usually presented to integrate a function with respect to the uniform measure on $[-1, 1]$ and starts with a change

of variables:

$$\int_{-1}^1 g(x) dx = \int_0^\pi g(\cos(\theta)) \sin(\theta) d\theta. \quad (1.13)$$

This expression can be written as an expansion of the integrand using cosine series. Therefore, knowing that cosine series are closely related to the Chebyshev polynomials of the first kind. Fejér's "first rule" (Trefethen, 2008) uses the Chebyshev polynomials roots as nodes $x^{(i)} = \cos(\theta^{(i+1/2)})$, associated with the following weights:

$$w_i = \frac{2}{n} \left(1 - 2 \sum_{j=1}^{\lfloor n/2 \rfloor} \frac{1}{4j^2 - 1} \cos(j\theta^{(2i+1)}) \right). \quad (1.14)$$

These two univariate integration schemes are both very efficient on a wide panel of functions. Yet, Fejér-Clebschaw-Curtis is sequential and offers easy implementations, benefitting from powerful algorithms such as the *fast Fourier transform*. Fig. 1.3 illustrates the nested properties of Fejér-Clebschaw-Curtis quadrature by representing the nodes of quadrature rules with increasing size.

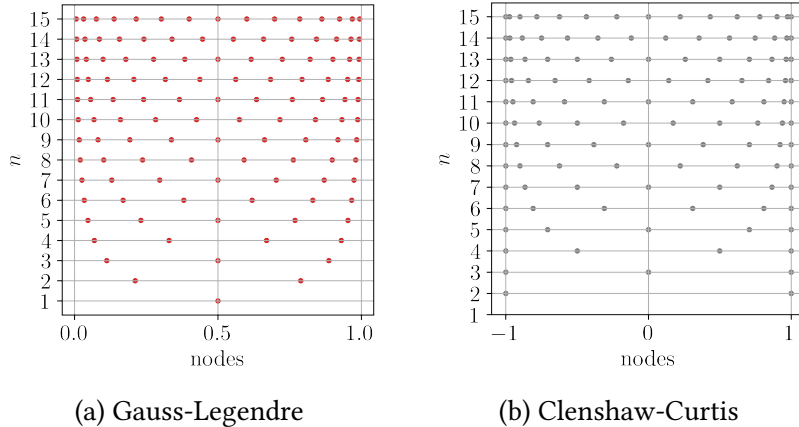


Figure 1.3 Univariate quadrature nodes for increasing sizes ($1 \leq n \leq 15$)

Uncertainty quantification problems are rarely unidimensional, but one can directly build a multivariate quadrature rule by defining the tensor product (also called full grids) of univariate rules. This exhaustive approach quickly shows its practical limits as the problem's dimension increases. In Fig. 1.4, the left plot represents a two-dimensional tensor product of identical Gauss-Legendre quadratures. Alternatively, sparse multivariate quadratures (i.e., Smolyak sparse grid) explore the joint domain more efficiently. Using the Smolyak recursive formula (see e.g., Sullivan 2015), two univariate quadratures can be combined as illustrated on the right of Fig. 1.4.

Monte Carlo methods

Monte Carlo methods were initially developed in the 1940s to solve problems in neutronics. Ever since, this frequentist technique has been applied to the resolution of the Lebesgue integral.

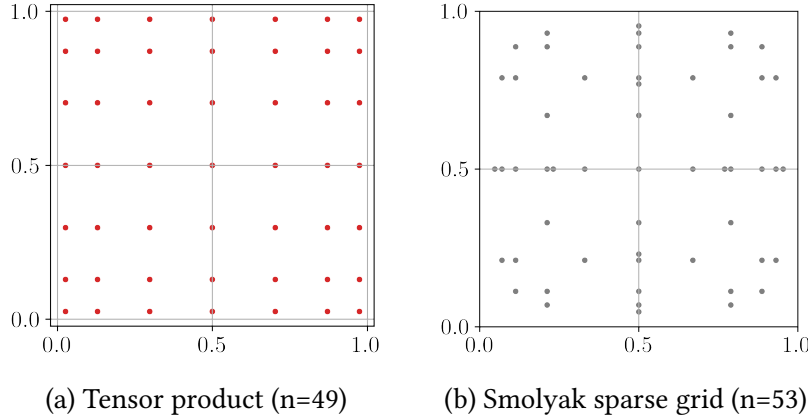


Figure 1.4 Two identical univariate Gauss-Legendre quadratures combined as a tensor product (left) and a Smolyak sparse grid (right).

To integrate a function g against a measure \mathbb{P}_X , it randomly generates points following the input measure. The integral is estimated by taking the uniform arithmetic mean of the nodes' images obtained by this random process.

This aleatory method requires to be able to generate points following a given distribution. To do so, the most common approach is to first uniformly generate a sequence of random points on $[0, 1]$. These sequences mimic actual randomness but are in fact generated by deterministic algorithms, also called pseudorandom number generators. Pseudorandom algorithms generate a sequence of numbers with a very large, but finite length. This sequence can be exactly repeated by fixing the same initial point, also called *pseudorandom seed*. Most programming languages use the Mersenne-Twister pseudorandom generator (Matsumoto and Nishimura, 1998), offering a very long period (around 4.3×10^{6001} iterations).

Formally, the “Vanilla” Monte Carlo (sometimes called “crude” Monte Carlo) method uses a set of i.i.d samples $\mathbf{X}_n = \{\mathbf{x}^{(1)}, \dots, \mathbf{x}^{(n)}\}$ following the joint distribution of \mathbb{P}_X . The Monte Carlo estimator of the integral is given by:

$$I_{\mathbb{P}_X}(g) \approx \bar{y}_n^{\text{MC}} = \frac{1}{n} \sum_{i=1}^n g(\mathbf{x}^{(i)}). \quad (1.15)$$

By construction, the law of large numbers makes this estimator unbiased, however, it converges relatively slowly. Considering the images of the sample \mathbf{X}_n , one can also estimate the variance of the output random variable $\hat{\sigma}_Y^2$. The variance of the Monte Carlo estimator results from a manipulation of the central limit theorem:

$$\text{Var}\left(\bar{y}_n^{\text{MC}}\right) = \frac{1}{\sqrt{n}} \text{Var}(g(\mathbf{X})). \quad (1.16)$$

This estimator also comes with theoretical confidence intervals at $\alpha\%$, regardless of the output distribution:

$$I_{\mathbb{P}_X}(g) \in \left[\bar{y}_n^{\text{MC}} - q_\alpha \frac{\text{Var}(g(\mathbf{X}))}{\sqrt{n}}, \bar{y}_n^{\text{MC}} + q_\alpha \frac{\text{Var}(g(\mathbf{X}))}{\sqrt{n}} \right], \quad (1.17)$$

where q_α is the α -quantile of the standard normal distribution. Monte Carlo presents the advantage of being a universal method, with no bias and strong convergence guarantees. Moreover, it is worth noting that its convergence properties do not depend on the dimension of the input domain. Unlike the previous multivariate deterministic quadrature, it doesn't suffer from the curse of dimensionality. The main limit of crude Monte Carlo is its convergence speed, making it intractable for most practical cases. More recent methods aim at keeping the interesting properties of this technique while making it more efficient. Among the *variance reduction* methods, let us mention importance sampling, stratified sampling (e.g., Latin hypercube sampling), control variates and multi-level Monte Carlo. For further details, the reader may refer to Chapters 8, 9 and 10 from [Owen \(2013\)](#) and [\(Giles, 2008\)](#).

Quasi-Monte Carlo and Koksma-Hlawka inequality

Among the methods presented so far, classical deterministic quadratures are subject to the curse of dimension while Monte Carlo methods deliver contrasted performances. Quasi-Monte Carlo is a deterministic family of numerical integration schemes with respect to the uniform measure on $[0, 1]$. It offers powerful performances with strong guarantees by choosing nodes according to *low discrepancy* sequences.

The discrepancy of a set of nodes (or a design) can be seen as a metric of its uniformity. The lowest the discrepancy of a design is, the “closest” it is to uniformity.

The Koksma-Hlawka theorem ([Morokoff and Caflisch, 1995](#); [Leobacher and Pillichshammer, 2014](#)) is a fundamental result for understanding the role of the discrepancy in numerical integration.

Theorem 2 (Koksma-Hlawka). *If $g : [0, 1]^d \rightarrow \mathbb{R}$ has a bounded variation (i.e., its total variation is finite), then for any design $\mathbf{X}_n = \{\mathbf{x}^{(1)}, \dots, \mathbf{x}^{(n)}\} \in [0, 1]^d$:*

$$\left| \int_{[0,1]^d} g(\mathbf{x}) d\mathbf{x} - \frac{1}{n} \sum_{i=1}^n g(\mathbf{x}^{(i)}) \right| \leq V(g) D^*(\mathbf{X}_n). \quad (1.18)$$

Where $D^*(\mathbf{X}_n)$ is the star discrepancy of the design \mathbf{X}_n , while $V(g)$ quantifies the complexity of the integrand, which is related to its total variation. The reader might refer to [Leobacher and Pillichshammer \(2014\)](#) Section 3.4 for further mathematical proof.

The function's variation $V(g)$ in Eq. (1.18) can be formally defined as the Hardy-Klause variation:

$$V(g) = \sum_{u \subseteq \{1, \dots, p\}} \int_{[0,1]^u} \left| \frac{\partial^u g}{\partial \mathbf{x}^u}(\mathbf{x}_u, 1) \right| d\mathbf{x}_u. \quad (1.19)$$

In which the L_p star discrepancy of a design \mathbf{X}_n is defined as the L_p -norm of the difference between the empirical CDF of the design $\widehat{F}_{\mathbf{X}_n}$ and the CDF of the uniform distribution F_U :

$$D_p^*(\mathbf{X}_n) = \|\widehat{F}_{\mathbf{X}_n} - F_U\|_p = \left(\int_{[0,1]^d} |\widehat{F}_{\mathbf{X}_n}(\mathbf{x}) - F_U(\mathbf{x})|^p d\mathbf{x} \right)^{1/p}. \quad (1.20)$$

Additionally, the L_∞ star discrepancy can be defined from a geometric point of view. Let us first consider the number of elements from a design \mathbf{X}_n , falling in a subdomain $[\mathbf{0}, \mathbf{x})$ as $\#(\mathbf{X}_n \cap [\mathbf{0}, \mathbf{x}))$. Then, if this empirical quantification is compared with the volume of the rectangle $[\mathbf{0}, \mathbf{x})$, denoted by $\text{vol}([\mathbf{0}, \mathbf{x}))$, the star discrepancy is expressed as:

$$D^*(\mathbf{X}_n) = \sup_{\mathbf{x} \in [0,1]^d} \left| \frac{\#(\mathbf{X}_n \cap [\mathbf{0}, \mathbf{x}))}{n} - \text{vol}([\mathbf{0}, \mathbf{x})) \right|. \quad (1.21)$$

Let us point out that this star discrepancy is equivalent to the Kolmogorov-Smirnov statistic, verifying whether the design follows a uniform distribution.

One can notice how the Koksma-Hlawka inequality dissociates the quadrature performance into a contribution from the function complexity and one from the repartition of the quadrature nodes. Knowing that the complexity of the studied integrand is fixed, this property explains the motivation to generate low-discrepancy quadratures in numerical integration.

Note that the design can also be considered as a discrete distribution (uniform sum of Dirac distributions). The discrepancy can then be expressed as a probabilistic distance between this discrete distribution and the uniform distribution. A generalized discrepancy between distributions called *maximum mean discrepancy* is introduced in the Appendix ?? and used for efficient sampling in Chapter ?? of this manuscript.

Some famous low-discrepancy sequences (e.g., van der Corput, Halton, Sobol', Faure, etc.) can offer a bounded star discrepancy $D^*(\mathbf{X}_n) \leq \frac{C \log(n)^d}{n}$, with the constant C depending on the sequence. Therefore, using these sequences as a quadrature rule with uniform weights provides the following absolute error upper bound:

$$\left| \int_{[0,1]^d} g(\mathbf{x}) d\mathbf{x} - \frac{1}{n} \sum_{i=1}^n g(\mathbf{x}^{(i)}) \right| \leq \frac{V(g) \log(n)^d}{n}. \quad (1.22)$$

The generation of such sequences does not necessarily require more effort than pseudo-random sampling. Chapter 15 in [Owen \(2013\)](#) offers an extended presentation of the ways to generate different low-discrepancy sequences. For example, the van der Corput and Halton sequences rely on congruential generators.

Halton sequences in medium dimension, unfortunately introduce pathological patterns when looking at their subprojections. To overcome these limits, digital nets such as the famous Sobol' or Faure sequences were developed. Sobol' sequences are in base two and have the advantage of being extensible in dimension. Note that by construction, these sequences offer significantly lower discrepancies for specific size values. Typically, designs with sizes equal to powers of two or power of prime numbers will be favorable. To illustrate the different repartition and properties of the methods, Fig. 1.5 represents the three Monte Carlo and quasi-Monte Carlo designs (with size $n = 256$). Each is split into the first 128 points (in red) and the following 128 points (in black) to show the nested properties of the QMC sequences.

Crude Monte Carlo estimators provide a confidence associated to the estimate. This complementary information is essential to deliver an end-to-end uncertainty quantification, which

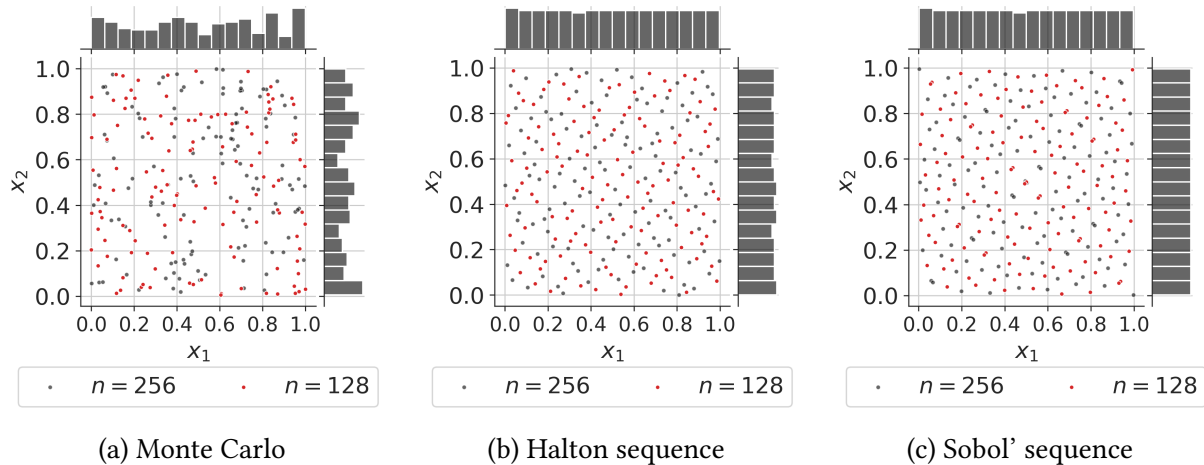


Figure 1.5 Nested Monte Carlo and quasi-Monte Carlo designs ($n = 256$)

misses in deterministic QMC methods. *Randomized quasi-Monte Carlo* (RQMC) is a method introducing some randomness in QMC in order to compute confidence intervals while benefiting from a low variance. A specific review of the randomized (also called “scrambled”) QMC is proposed by L’Ecuyer (2018). Various authors recommend the use of RQMC by default instead of QMC as a good practice. Recent works aim at exploring the use of these methods to estimate different quantities of interest, such as an expected value (Gobet et al., 2022) or a quantile (Kaplan et al., 2019).

Ultimately, quasi-Monte Carlo methods generate powerful integration schemes. The Koksma-Hlawka inequality associates an upper bound and a convergence rate to most integrals. A randomization overlay fades the deterministic property of these designs, allowing to compute confidence intervals. In the following, sampling techniques are presented from the numerical *design of experiments* point of view. Even if the goal might look different from numerical integration, these two topics shares many methods and concepts.

OpenTURNS 2 (Numerical integration). The Python code available in Appendix ?? proposes a minimalistic OpenTURNS example to build multivariate quadrature rules. Figures illustrating the present section may be reproduced, using the OpenTURNS scripts available on GitHub⁵.

1.4.2 Numerical design of experiments

Numerical design of experiments aim at uniformly exploring the input domain, e.g., to build a learning set for a regression model, or to initialize a multi-start optimization strategy. A design of experiment (also simply called design) is qualified as *space-filling* when it uniformly covers a domain. As well as in integration, a design is used to propagate uncertainties through a numerical model (or a physical experiment). However, a difference comes from the fact that

⁵https://github.com/efekhari27/thesis/blob/main/numerical_experiments/chapter1/integration.ipynb

this community often works with designs of very limited size. Users of designs of experiments also consider various properties.

- Some might be interested in the sequentiality of a sampling method, to eventually add new points as they get their computational budget extended.
- Some might request a sampling method conserving its properties in any subdomains. This second property can be useful to reduce the problem's dimension by dropping a few unimportant variables (see the following Section 1.6 on global sensitivity analysis).

Different metrics are commonly used to quantify how space-filling a design of experiments is. The previously introduced of discrepancies are an example of space-filling metrics. Other types of space-filling metrics rely on purely geometrical considerations.

This section will first define a few space-filling metrics. Secondly, the *Latin hypercube sampling* (LHS) will be introduced as a variance-reduction method that became popular the UQ community. Finally, a general discussion on uncertainty propagation with respect to non-uniform measures will be presented.

Space-filling metrics and properties

Space-filling criteria are key to evaluating designs and are often used to optimize their performances. In the previous section, the star discrepancy was introduced as a distance of a finite design to uniformity. However, the L_∞ star discrepancy is hard to estimate, fortunately, Warnock (1972) elaborated an explicit expression specific to the L_2 star discrepancy:

$$[D_2^*(\mathbf{X}_n)]^2 = \frac{1}{9} - \frac{2}{n} \sum_{i=1}^n \prod_{l=1}^d \frac{(1-x_l^{(i)})}{2} + \frac{1}{n^2} \sum_{i,j=1}^n \prod_{l=1}^d \left[1 - \max(x_l^{(i)}, x_l^{(j)}) \right]. \quad (1.23)$$

One can notice that this expression is similar to the Cramér-von Mises test statistic. Even if this expression is tractable, Fang et al. (2018) detailed its limits: the star L_2 discrepancy generates designs that are not robust to projections in sub-spaces; it is not an invariant metric by rotation and reflection; and finally, by construction, L_p discrepancies give a disproportionate role to the point $\mathbf{0}$ by anchoring the box $[\mathbf{0}, \mathbf{x}]$.

Two improved criteria were proposed by Hickernell (1998) with the *centered L_2 discrepancy* and the *wrap-around L_2 discrepancy*. Those are widely used in practice since they solve the previous limits while satisfying the Koksma-Hlawka inequality with a modification of the total variation. Let us introduce the explicit formula of the centered L_2 discrepancy:

$$\begin{aligned} CD_2^*(\mathbf{X}_n) = & \left(\frac{13}{12} \right)^d - \frac{2}{n} \sum_{i=1}^n \prod_{l=1}^d \left(1 + \frac{1}{2} |x_l^{(i)} - 0.5| - \frac{1}{2} |x_l^{(i)} - 0.5|^2 \right) \\ & + \frac{1}{n^2} \sum_{i,j=1}^n \prod_{l=1}^d \left(1 + \frac{1}{2} |x_l^{(i)} - 0.5| + \frac{1}{2} |x_l^{(j)} - 0.5| - \frac{1}{2} |x_l^{(i)} - x_l^{(j)}| \right). \end{aligned} \quad (1.24)$$

As an alternative to discrepancies, many geometrical criteria exist to assess a space-filling design. The most common way to do so is to maximize the minimal distance among the pairs of Euclidian distances between the points of a design. The criterion to maximize is then simply called the *minimal distance* of a design (denoted ϕ_{\min}). For numerical reasons, the ϕ_p criterion is often used instead of the minimal distance. The following ϕ_p criterion converges towards the minimum distance as $p \geq 1$ tends to infinity:

$$\phi_{\min}(\mathbf{X}_n) = \min_{i \neq j} \|\mathbf{x}^{(i)} - \mathbf{x}^{(j)}\|_2, \quad \phi_p(\mathbf{X}_n) = \sum_{i=1}^j \sum_{j=1}^n \left(|x^{(i)} - x^{(j)}|^{-p} \right)^{\frac{1}{p}}. \quad (1.25)$$

More space-filling criteria are reviewed in [Abtini \(2018\)](#) and in the Appendix A from [Da Veiga et al. \(2021\)](#). Further relations between some mathematical objects related to space-filling are developed in [Pronzato and Müller \(2012\)](#). These space-filling metrics are widely used to optimize a different sampling technique.

Latin hypercube sampling

Latin hypercube sampling is a method introduced in 1979 ([Mckay et al., 1979](#)), initially for numerical integration. In a bounded domain, this stratified sampling technique forces the distribution of each sub-projection to be as uniform as possible. To do so, for an n -sized design, each marginal domain is divided into n identical segments. This creates a regular grid of n^d squared cells over the domain.

Then, a Latin hypercube design (LHD) does not allow more than one point within a segment. That way, new LHDs can be built as a permutation of the marginals of an existing LHD. Inside each selected cell from the grid, the point can be placed at the center or randomly.

Various contributions proposed a variance, and a central limit theorem to LHS ([Koehler and Owen, 1996](#)). Similarly to the Monte Carlo variance in Eq. (1.16), LHS variance can be expressed as:

$$\text{Var}\left(\bar{y}_n^{\text{LHS}}\right) = \frac{1}{\sqrt{n}} \text{Var}(g(\mathbf{X})) - \frac{C}{n} + o\left(\frac{1}{n}\right). \quad (1.26)$$

Where C is a positive constant, showing that the LHS usually reduces the variance for numerical integration. Because of its stratified structure, LHS can generate poor designs from a space-filling point of view (see e.g., the illustration in Fig. 1.6a). The following section presents various methods aiming at optimizing LHDs.

Optimized Latin hypercube sampling

To improve the space-filling property of LHD, it is common to add an optimization step. The goal of this optimization is to improve a space-filling criterion by generating LHD from permutations of an initial LHD. [Damblin et al. \(2013\)](#) reviews LHS optimization using different discrepancy criteria and subprojection properties. This optimization can be performed by different algorithms, such as the stochastic evolutionary algorithm or simulated annealing. The results from

this work show that LHD optimized by L_2 centered or wrap-around discrepancies offer strong robustness to two-dimensional projections. It also shows that these designs keep this property for dimensions larger than 10, while scrambled Sobol' sequences lose it. Fig. 1.6 illustrates two LHD, optimized by the L_2 centered discrepancy and the geometrical ϕ_p . The space-filling difference is not obvious in two dimensions, and they both spread uniformly.

More recent work developed different ways to optimize LHD. Among them, let us mention the maximum projection designs from Joseph et al. (2015) which relies on the optimization of a geometrical criterion and delivers interesting performances. In the same vein, the uniform projection designs from Sun et al. (2019) is also a method to optimize LHS, this time based on a criterion averaging discrepancies between each pairs of marginals.

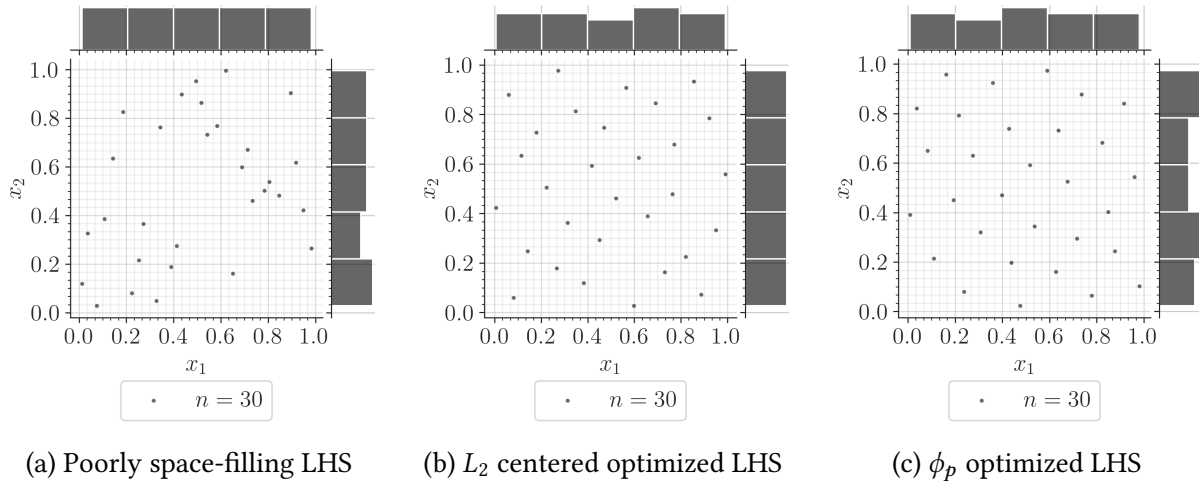


Figure 1.6 Latin hypercube designs with poor and optimized space-filling properties ($n = 8$)

OpenTURNS 3 (Design of experiments). The Python code available in Appendix ?? proposes a minimalistic OpenTURNS example to build an LHS and an LHS optimized w.r.t. to a space-filling metric (here the L2-centered discrepancy) using the simulated annealing algorithm. Figures illustrating the present section may be reproduced, using the OpenTURNS scripts available on GitHub⁶.

1.4.3 Summary and discussion

A wide panel of sampling techniques exists for numerical integration or design of experiments purposes. In both cases, the studied domain is bounded and the targeted measure is uniform. However, uncertainty propagation is often performed on complex input distributions, with possibly unbounded domains. In uncertainty quantification, this step might be referred to as the estimation of the output random variable's central tendency (i.e., its mean and variance). Central tendency estimation is a numerical integration with respect to any input distribution,

⁶https://github.com/efekhari27/thesis/blob/main/numerical_experiments/chapter1/designofexperiments.ipynb

sometimes called *probabilistic integration* (Briol et al., 2019) as part of *probabilistic numerics* (Oates and Sullivan, 2019).

To generate i.i.d samples following any distribution (i.e., non-uniform), one may use *inverse transform* sampling. After generating samples in the unit hypercube, the inverse CDF function (i.e., quantile function) is applied on marginals. Finally, possible dependence effects may be added using the Sklar theorem Eq. (1).

One may wonder if the properties from the uniform design are conserved after this nonlinear transformation. Li et al. (2020) explores this question from a discrepancy point of view. The authors find correspondences between discrepancies with respect to uniformity and discrepancy with respect to the target distribution. However, this result show practical limits, sometimes making the interpretation of the last discrepancy easier. This question will be further discussed in the [Chapter 4], using a more general framework.

Let us also remark that, depending on the distribution, defining the inverse CDF is not always possible. For example, samples following truncated distributions or mixture distributions might sometime be generated with a different technique. The *acceptance-rejection* method offers a versatile generation only based on the PDF f_x . Assuming that a well-known proposal PDF f_x^* exists such that $f_x \leq c \times f_x^*, c \in [1, +\infty]$. One may generate a sample according to $c \times f_x^*$ and only retain from this sample the points under the PDF f_x . Note that some sampling methods, such as QMC, are not well suited with acceptance-rejection since their structure gets perturbed.

In this section, many methods were presented to propagate input uncertainties against a deterministic function. The propagation with the three following goals and contexts were introduced:

- building a quadrature rule for numerical integration against a uniform distribution,
- creating a space-filling design of experiments to uniformly explore the space, often in a small data context (e.g., to build the learning set of a surrogate model),
- generating a design for central-tendency estimation, which is simply a numerical integration against a nonuniform density.

These three objectives have been explored in different communities, but they actually share similar methods. They all have in common the general analysis (i.e., global behavior) of the output random variable. However, some studies require to shift the focus towards specific areas of the output random variables. When using uncertainty propagation to perform risk analysis, the events studied are often contained in the tails of the output distribution. In this case, dedicated uncertainty propagation methods will significantly improve the estimation of the associated statistical quantities.

1.5 Uncertainty propagation for rare event estimation

This section aims at presenting another type of uncertainty propagation. In the context of a risk analysis applied to the engineering field, the reliability of a system needs to be assessed. Most often, a risk measure associated with a failure mode of the studied system is estimated.

Since most systems studied in risk analysis must be highly reliable, the occurrence of such event is qualified as rare. Only a small amount of extreme input conditions or an unlikely unfavorable combinations of inputs lead to the failure of the system. Hence, the usage of the equivalent terms *reliability analysis* and *rare event estimation*. The notion of risk associated with an event is often decomposed as a product of its likelihood and its consequences. The failure of a system might be very rare, but its consequences can be severe (e.g., civil engineering structures, nuclear infrastructure, telecommunication networks, electrical grid, railway signalling, etc.).

Different risk measures (i.e., quantities of interest related to the tail of the distributions) can be studied depending on the type of risk analysis. Quantiles are a first conservative measure, widely used for risk analysis. The α -quantile q_α of the output random variable Y is defined as:

$$q_\alpha = \inf_{y \in \mathbb{R}} \{F_Y(y) \geq \alpha\}, \quad \alpha \in [0, 1]. \quad (1.27)$$

As an alternative, one can define a scalar safety threshold y_{th} that should not be exceeded to keep the system safe. Then, a second risk measure is the probability of exceeding this safety threshold, also called *failure probability*:

$$p_f = \mathbb{P}(Y \geq y_{\text{th}}), \quad y_{\text{th}} \in \mathbb{R}. \quad (1.28)$$

To illustrate this quantity, Fig. 1.7 shows the one-dimensional propagation of a normal distribution (represented by the PDF on the left), through a function $g(\cdot)$. The probability of exceeding a given threshold y_{th} is represented by the area in red under the output PDF on top. An interesting reflection on the use and the interpretation of risk measures including measures from the finance domain such as the *conditional value-at-risk* (also called superquantile) is presented in [Rockafellar and Royset \(2015\)](#).

In the following section, the formalism for reliability analysis problems will be first presented, then the main methods solving this specific problem will be introduced. Note however that the present work will not address the problems of time-dependent reliability analysis tackled in [Hawchar et al. \(2017\)](#).

1.5.1 Problem statement

Following to the UQ methodology, the behavior of the system is modeled by $\mathcal{M}(\cdot)$. Considering the problem of exceeding a safety threshold in Eq. (1.28), the system's performance is commonly defined as the difference between the model's output and the safety threshold $y_{\text{th}} \in \mathbb{R}$. Formally,

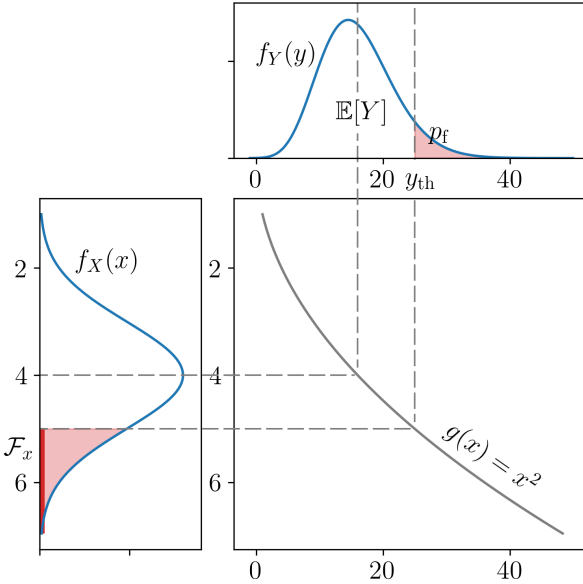


Figure 1.7 One-dimensional reliability analysis example

the *limit-state function* (LSF) is a deterministic function $g : \mathbb{R} \rightarrow \mathbb{R}$ quantifying this performance:

$$g(\mathbf{x}) = y_{\text{th}} - \mathcal{M}(\mathbf{x}). \quad (1.29)$$

Depending on the sign of its images, this function splits the inputs space into two disjoint and complementary domains called the *failure domain* \mathcal{F}_x , and the *safe domain* \mathcal{S}_x which are defined as:

$$\mathcal{F}_x = \{\mathbf{x} \in \mathcal{D}_x \mid g(\mathbf{x}) \leq y_{\text{th}}\}, \quad \mathcal{S}_x := \{\mathbf{x} \in \mathcal{D}_x \mid g(\mathbf{x}) > y_{\text{th}}\}. \quad (1.30)$$

The border between these two domains is a hypersurface called *limit-state surface* (LLS), defined by $\mathcal{F}_x^0 := \{\mathbf{x} \in \mathcal{D}_x \mid g(\mathbf{x}) = 0\}$. Similarly to any UQ study using a numerical model, this problem may require to be resolved using a limited number of calls to a black-box simulator. The difficulties in a reliability problem come from the properties of the LSF: nonlinear, costly to evaluate or with a multimodal failure domain. Additionally, note that the reliability problem can be the composition of multiple reliability problems, often modeled as system of problems in series and parallel.

A rare event estimation results from a particular uncertainty propagation through the LSF. Considering the output variable of interest $g(\mathbf{X})$, its probability of being negative (i.e., in the failure domain) is a common risk measure. The so-called *failure probability*, denoted by p_f , is the quantity of interest for reliability analysis considered in this work. This quantity is formally written⁷:

$$p_f = \mathbb{P}(Y \geq y_{\text{th}}) = \mathbb{P}(g(\mathbf{X}) \leq 0) = \int_{\mathcal{F}_x} f_{\mathbf{X}}(\mathbf{x}) d\mathbf{x} = \int_{\mathcal{D}_x} \mathbb{1}_{\mathcal{F}_x}(\mathbf{x}) f_{\mathbf{X}}(\mathbf{x}) d\mathbf{x}, \quad (1.31)$$

⁷Note that this probabilistic integration is usually written using the PDF $f_{\mathbf{X}}(\cdot)$, but it could identically be expressed in terms of probability measure by taking $f_{\mathbf{X}}(\mathbf{x}) d\mathbf{x} = d\mathbb{P}_{\mathbf{X}}(\mathbf{x})$, $\forall \mathbf{x} \in \mathcal{D}_x$.

were the indicator function applied to the failure domain returns $\mathbb{1}_{\{\mathcal{F}_X\}}(x) = 1$ if $x \in \mathcal{F}_X$ and $\mathbb{1}_{\{\mathcal{F}_X\}}(x) = 0$ otherwise. Rare event estimation implies both contour finding (i.e., characterizing the LSF) and an estimation strategy targeting the failure domain (often with a limited number of simulations). Note that failure events are qualified as rare when their failure probability has an order of magnitude between $10^{-2} \leq p_f \leq 10^{-9}$ (see e.g., [Lemaire 2013](#)).

Instead of directly performing a reliability analysis in the physical space (i.e., \mathbf{x} -space), these problems are usually solved in the *standard normal space* (i.e., \mathbf{u} -space). Working in the standard space reduces numerical issues caused by potentially unscaled or asymmetric marginals. Moreover, a larger panel of methods can be applied in the standard space since the random inputs become independent. The bijective mapping between these two spaces is called an “iso-probabilistic transformation”, denoted by $T : \mathcal{D}_X \subseteq \mathbb{R}^d \rightarrow \mathbb{R}^d$, $\mathbf{x} \mapsto T(\mathbf{X}) = \mathbf{u} = (u_1, \dots, u_d)^\top$. When considering any random vector $\mathbf{X} = (X_1, \dots, X_d)^\top$ and the independent standard Gaussian vector $\mathbf{U} = (U_1, \dots, U_d)^\top$, the following equalities hold:

$$\mathbf{U} = T(\mathbf{X}) \Leftrightarrow \mathbf{X} = T^{-1}(\mathbf{U}). \quad (1.32)$$

A reliability problem can be expressed in the standard normal space. Let us first consider the transformed limit-state function \check{g} defined as:

$$\check{g} : \begin{array}{ccc} \mathbb{R}^d & \longrightarrow & \mathbb{R} \\ \mathbf{u} & \longmapsto & \check{g}(\mathbf{u}) = (g \circ T^{-1})(\mathbf{u}). \end{array} \quad (1.33)$$

Since this transformation is a diffeomorphism⁸, one can apply the change of variable $\mathbf{x} = T(\mathbf{u})$ to express the reliability problem from Eq. (1.31) in the standard space:

$$p_f = \mathbb{P}(\check{g}(\mathbf{U}) \leq 0) = \int_{\mathcal{F}_u} \varphi_d(\mathbf{u}) d\mathbf{u} = \int_{\mathbb{R}^d} \mathbb{1}_{\mathcal{F}_u}(\mathbf{u}) \varphi_d(\mathbf{u}) d\mathbf{u}, \quad (1.34)$$

with the transformed failure domain denoted by $\mathcal{F}_u = \{\mathbf{u} \in \mathbb{R}^d \mid \check{g}(\mathbf{u}) \leq 0\}$, and the d -dimensional standard Gaussian PDF $\varphi_d(\mathbf{u}) = \frac{1}{(2\pi)^{d/2}} \exp\left(-\frac{\|\mathbf{u}\|_2^2}{2}\right)$. The fact that the failure probability is invariant by this transformation allows the analyst to estimate this quantity in both spaces.

Different types of transformations exist, such as the Rosenblatt or the generalized Nataf transformation introduced by [Lebrun \(2013\)](#). In practice, the transformation choice depends on the properties of the input distribution studied. For example in OpenTURNS, depending on the three following cases, different types of transformations are applied:

- for elliptical distributions, a linear Nataf transformation is applied;
- for distributions with an elliptical copula, the generalized Nataf transformation is used;
- otherwise, the Rosenblatt transformation is used.

⁸Considering two manifolds A and B , a transformation $T : A \rightarrow B$ is called a diffeomorphism if it is a differentiable bijection with a differentiable inverse $T^{-1} : B \rightarrow A$.

1.5.2 Rare event estimation methods

The main risk measure chosen for rare event estimation in this work is the previously introduced failure probability. Therefore, let us recall that the goal is to build an efficient estimation (or approximation) of the following d -dimensional integral:

$$p_f = \int_{\mathcal{D}_x} \mathbb{1}_{\mathcal{F}_x}(\mathbf{x}) f_x(\mathbf{x}) d\mathbf{x} \quad (1.35)$$

In the context of rare event estimation using costly to evaluate numerical models, the simulation budget is often limited to n runs with $p_f \ll \frac{1}{n}$. Which explains the need for specific methods offering approximations or simulations targeting the unknown failure domain. Two types of rare event estimation methods are classically presented: first, using approximation approaches, second, using sampling techniques. This section introduced the commonly used rare event methods, see [Morio and Balesdent \(2015\)](#) for a more exhaustive review.

First and second order reliability methods (FORM/SORM)

The well-known first and second order reliability methods (FORM and SORM) both rely on a geometric approximation to estimate a failure probability ([Lemaire, 2013](#)). They extrapolate a local approximation of the LSF built in the vicinity of a *most-probable-failure-point* (MPFP), also called *design point*.

Working in the standard space, the methods first look for this MPFP, denoted P^* , with coordinates \mathbf{u}^* . To find it, one can solve the following quadratic optimization problem:

$$\mathbf{u}^* = \arg \max_{\mathbf{u} \in \mathbb{R}^d} (\mathbb{1}_{\mathcal{F}_u}(\mathbf{u}) \varphi_d(\mathbf{u})). \quad (1.36)$$

Using the properties of the standard space allows us to rewrite it as:

$$\mathbf{u}^* = \arg \max_{\mathbf{u} \in \mathbb{R}^d} \frac{1}{(2\pi)^{d/2}} \exp\left(-\frac{\mathbf{u}^\top \mathbf{u}}{2}\right) \quad \text{s.t. } \mathbf{u} \in \mathcal{F}_u \quad (1.37)$$

$$= \arg \min_{\mathbf{u} \in \mathbb{R}^d} \mathbf{u}^\top \mathbf{u} \quad \text{s.t. } \check{g}(\mathbf{u}) \leq 0. \quad (1.38)$$

This problem then becomes a quadratic optimization under nonlinear constraint. It is classically solved by gradient decent algorithms (e.g., Abdo-Rackwitz algorithm [Abdo and Rackwitz, 1991](#)) but can also use gradient-free techniques (e.g., Cobyla algorithm [Powell, 1994](#)). This point defines the smallest Euclidian distance between the LSS and the origin of the standard space. To understand its role in the reliability problem, let us recall that the density of the standard normal present an exponential decay in its radial and tangential direction. Then, P^* is the point with the biggest contribution to the failure probability (see the illustration in Fig. 1.8).

This distance between the origin and P^* is another risk measure, defined as the *Hasofer-Lind reliability index* (Lemaire, 2013), $\beta \in \mathbb{R}$ such that:

$$\beta = \|\mathbf{u}^*\|_2 = \boldsymbol{\alpha}^\top \mathbf{u}^*, \quad \text{s.t.} \quad \boldsymbol{\alpha} = \frac{\nabla_{\mathbf{u}} \check{g}(\mathbf{u})}{\|\nabla_{\mathbf{u}} \check{g}(\mathbf{u})\|_2}. \quad (1.39)$$

The vector $\boldsymbol{\alpha}$ is the unit vector pointing at P^* from the origin point.

Then, FORM aims at approximating the limit-state function $\check{g}(\cdot)$ by its first-order Taylor expansion around the MPFP, denoted $\check{g}_1(\mathbf{u}^*)$:

$$\begin{aligned} \check{g}(\mathbf{u}) &= \check{g}_1(\mathbf{u}^*) + o\left(\|\mathbf{u} - \mathbf{u}^*\|_2^2\right) \\ &= \check{g}(\mathbf{u}^*) + \nabla_{\mathbf{u}} \check{g}(\mathbf{u}^*)^\top (\mathbf{u} - \mathbf{u}^*) + o\left(\|\mathbf{u} - \mathbf{u}^*\|_2^2\right) \\ &= \|\nabla_{\mathbf{u}} \check{g}(\mathbf{u})\|_2 (\boldsymbol{\alpha}^\top \mathbf{u}^* - \boldsymbol{\alpha}^\top \mathbf{u}) + o\left(\|\mathbf{u} - \mathbf{u}^*\|_2^2\right) \end{aligned} \quad (1.40)$$

Using $\check{g}_1(\cdot)$ as an approximation of the LSF, the failure probability can be approximated as:

$$p_f \approx p_f^{\text{FORM}} = \mathbb{P}(-\boldsymbol{\alpha}^\top \mathbf{u} \leq -\beta) = \Phi(-\beta), \quad (1.41)$$

with $\Phi(\cdot)$ the CDF of the standard Gaussian. Depending on the properties of the LFS, this approximation will be more or less accurate. Note that for a purely linear LFS, $p_f = p_f^{\text{FORM}}$. When the function is nonlinear, adding a quadratic term to the Taylor expansion can help the approximation. The approximation method is then called SORM for *second order reliability method*. However, this added complexity implies the computation of Hessian matrices, which can be complicated (see the Chapter 1 from Bourinet 2018 for their estimation).

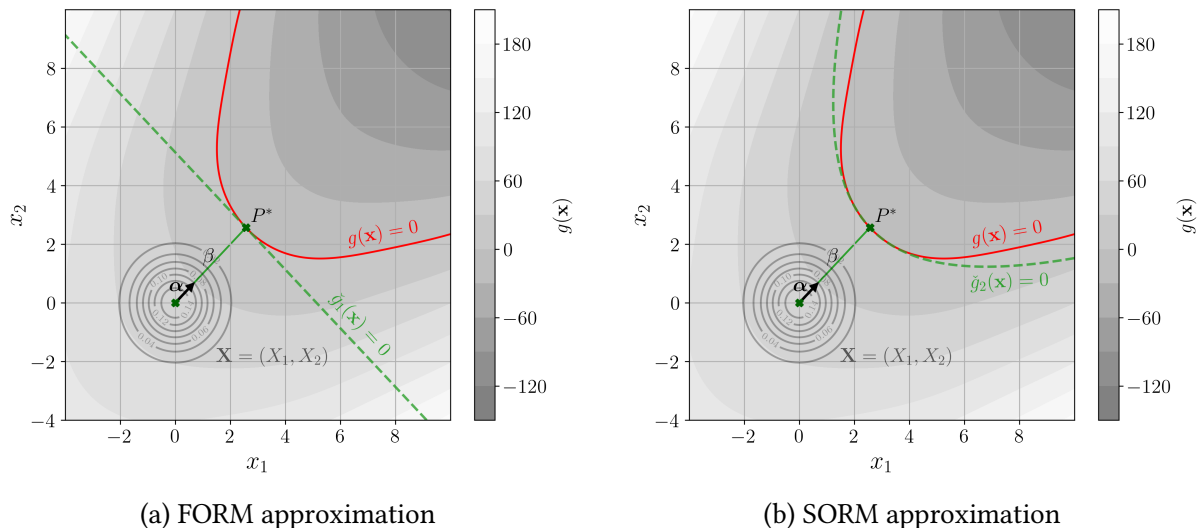


Figure 1.8 FORM and SORM approximation on a two-dimensional reliability problem

When the MPFP is not unique, the application of these methods might lead to important errors. From a geometrical point of view, having more than one MPFP means that more than one failure zones are at the same euclidean distance of the origin. Applying a FORM or SORM resolution in this particular case leads to the estimation of only one of the failure areas. The

muti-FORM algorithm (see [Der Kiureghian and Dakessian \(1998\)](#)) prevents this situation by applying successive FORM. Once the first MPFP $P^{*(1)}$ found, the LSS is modified by removing a nudge to find to following MPFP $P^{*(2)}$, positioned at a similar distance but in a different direction.

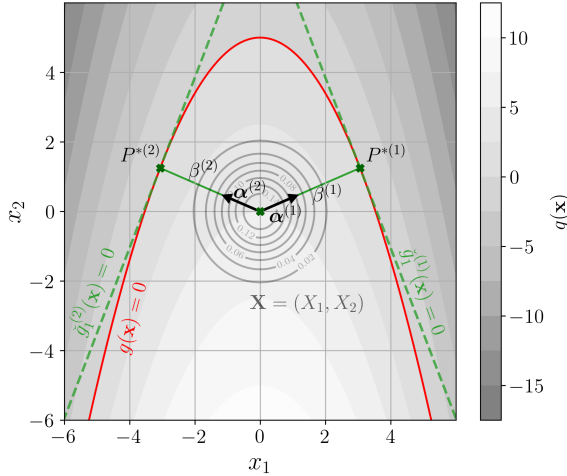


Figure 1.9 Multi-FORM approximation on an example with two MPFPs

Overall, FORM and SORM methods deliver a very efficient approximation of small probabilities for relatively simple problems (in terms of linearity and dimension). For this reason, they have been widely used in the practical context of limited simulation budget. [Straub \(2014\)](#) illustrates the efficiency of FORM approaches on industrial cases such as probabilistic fatigue damage. However, these methods present serious limits as the dimension increases (see the discussion in the Chapter 1 from [Chabridon 2018](#)). Additionally, their main drawback is the lack of complementary information concerning the confidence of the results. The textbook example illustrated in Fig. 1.9 shows that the method might miss some important areas of the failure domain, leading to poor estimations. As an alternative to approximation methods, simulation-based methods often provide to the analyst an assessment of the estimation's confidence.

Monte Carlo

Crude Monte Carlo sampling is a universal and empirical method for uncertainty propagation. As introduced earlier, it relies on the pseudo-random generation of i.i.d. samples $\{\mathbf{x}^{(i)}\}_{i=1}^n \stackrel{\text{i.i.d.}}{\sim} f_{\mathbf{X}}$. Only the estimator is now written using the indicator function applied to the LSF:

$$p_f \approx \hat{p}_f^{\text{MC}} = \frac{1}{n} \sum_{i=1}^n \mathbb{1}_{\mathcal{F}_x}(\mathbf{x}^{(i)}). \quad (1.42)$$

Provided that the failure probability is bounded, this estimator converges towards it almost surely according to the LLN. Once again, Monte Carlo offers an unbiased estimator, regardless of the problem's dimension or the regularity of the function $g(\cdot)$. Additionally, the variance of

this estimator is fully known:

$$\text{Var}(\widehat{p}_f^{\text{MC}}) = \frac{1}{n} p_f(1 - p_f). \quad (1.43)$$

The variance of this estimator can be used to build its confidence interval according to the central limit theorem (similarly to the ones from Eq. (1.17)). Because of the small scale of the quantities manipulated in rare event estimation, the estimator's coefficient of variation is also widely used:

$$\delta_{\widehat{p}_f^{\text{MC}}} = \frac{\sqrt{\text{Var}(\widehat{p}_f^{\text{MC}})}}{\mathbb{E}[\widehat{p}_f^{\text{MC}}]} = \sqrt{\frac{1 - p_f}{np_f}}. \quad (1.44)$$

In theory, Monte Carlo estimation presents multiple advantages for rare event estimation. First, this method can be applied directly in the physical space, without transformation (which is practical for complex input distributions). Second, it does not suffer from the curse of dimensionality. Third, it is qualified as embarrassingly parallel method since each of the numerical simulations are independent. Finally, it offers strong convergence guarantees and complementary information on the estimation confidence. These properties often make Monte Carlo the reference method in rare event estimation benchmarks.

However, the advantages of this estimator are shadowed by its slow convergence. To estimate a target failure probability $p_f = 10^{-\alpha}$, a Monte Carlo estimation with a convergence level $\delta_{\widehat{p}_f^{\text{MC}}} = 0.1$ famously requires $n = 10^{\alpha+2}$ simulations.

In the context of rare event estimation, Monte Carlo needs a number of simulation that is often prohibitive in practice. This excessive simulation budget comes from the fact that the vast majority of the samples drawn from the input distribution are not in the failure domain.

Importance sampling

Importance sampling (IS) is a variance reduction method, aiming at improving the performances of crude Monte Carlo sampling. In the context of rare event estimation, the main idea is to deliberately introduce a bias in the sampled density, shifting it towards the failure domain. If this shift actually goes towards the failure domain, it allows drawing more points in it, leading to a better estimate of our quantity.

The challenge in importance sampling is to pick a relevant *instrumental* distribution h_X (also called *auxiliary* distribution) to replace the distribution f_X . Then, by introducing the fully known *likelihood ratio* $w_X(x) = \frac{f_X(x)}{h_X(x)}$, one can rewrite $f_X(x) = w_X(x) h_X(x)$ and inject it in the failure probability expression:

$$p_f = \int_{\mathcal{D}_X} \mathbb{1}_{\mathcal{F}_X}(x) f_X(x) dx = \int_{\mathcal{D}_X} \mathbb{1}_{\mathcal{F}_X}(x) w_X(x) h_X(x) dx. \quad (1.45)$$

This simple writing trick allows us to integrate against the auxiliary distribution. With a Monte Carlo method, this task should be easier than integrating directly against the initial distribution.

The importance sampling estimator of the failure probability is defined for a sample drawn on the auxiliary distribution $\{\mathbf{x}^{(i)}\}_{i=1}^n \stackrel{\text{i.i.d.}}{\sim} h_{\mathbf{X}}$:

$$\hat{p}_f^{\text{IS}} = \frac{1}{n} \sum_{i=1}^n \mathbb{1}_{\mathcal{F}_{\mathbf{x}}}(\mathbf{x}^{(i)}) w_{\mathbf{X}}(\mathbf{x}^{(i)}). \quad (1.46)$$

Similarly to Monte Carlo, this estimator is unbiased, however, its variance is defined as:

$$\text{Var}(\hat{p}_f^{\text{IS}}) = \frac{1}{n} \left(\mathbb{E}_h \left[\left(\mathbb{1}_{\mathcal{F}_{\mathbf{x}}}(\mathbf{X}) \frac{f_{\mathbf{X}}(\mathbf{X})}{h_{\mathbf{X}}(\mathbf{X})} \right)^2 \right] - p_f^2 \right). \quad (1.47)$$

The quality of the variance reduction associated to this technique fully depends on the choice of the instrumental distribution. In fact, importance sampling can lead to higher variance than crude Monte Carlo when the instrumental distribution is poorly chosen (Owen and Zhou, 2000). However, an optimal instrumental distribution h_{opt} theoretically gives the smallest variance by setting it equal to zero in Eq. (1.47):

$$h_{\text{opt}}(\mathbf{x}) = \frac{\mathbb{1}_{\mathcal{F}_{\mathbf{x}}}(\mathbf{x}) f_{\mathbf{X}}(\mathbf{x})}{p_f}. \quad (1.48)$$

The optimal expression above is unfortunately not usable in practice since it includes the targeted quantity p_f . Considering this framework, various techniques intend to define instrumental distributions as close as possible to this theoretical result. An important review of the use of importance sampling in the context of reliability analysis was proposed by Tabandeh et al. (2022).

The most immediate solution is to combine the information provided by the results of FORM with importance sampling, simply called FORM-IS. In practice, the instrumental distribution is defined as the initial distribution centered on the design point resulting from FORM. Fig. 1.10 illustrates on the same two-dimensional case, the estimation by Monte Carlo and importance sampling centered on the design point. The points in red reached the failure domain and their number seem insufficient for Monte Carlo. Note that comparing the results from FORM and FORM-IS allows to assess the nonlinearity of the LSF in the vicinity of the design point. This strategy is simple to implement, but it inherits the main drawbacks of FORM, such as the limits related to multiple failure areas (see the example illustrated in Fig. 1.9). Finally, other importance sampling schemes integrate adaptive mechanisms, progressively leading the sampling towards the failure domain (Bugallo et al., 2017).

Adaptive importance sampling by cross-entropy

The *cross-entropy-based adaptive importance sampling* (CE-AIS) is an adaptive strategy, optimizing the IS variance reduction by searching the best instrumental distribution within a parametric

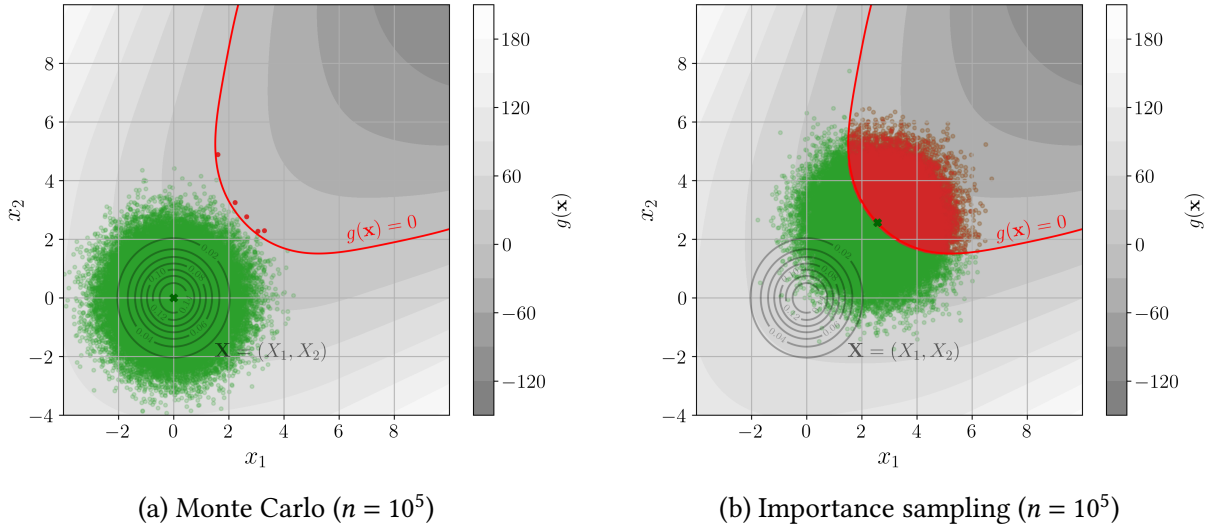


Figure 1.10 Illustration of a rare event estimation.

family. Let us consider the distribution h_λ , belonging to the parametric family \mathcal{H}_λ , defined as:

$$\mathcal{H}_\lambda = \left\{ \mathbf{x} \mapsto h_X(\mathbf{x}|\boldsymbol{\lambda}) = h_\lambda(\mathbf{x}), \quad \boldsymbol{\lambda} = (\lambda_1, \dots, \lambda_p) \in \mathcal{D}_\lambda \subseteq \mathbb{R}^p \right\}. \quad (1.49)$$

The early work of [Bucher \(1988\)](#) only included normal distributions to minimize the IS variance w.r.t. the parameter $\boldsymbol{\lambda}$, using Eq. (1.47) the optimization simplifies as:

$$\boldsymbol{\lambda}^* = \arg \min_{\boldsymbol{\lambda} \in \mathcal{D}_\lambda} \mathbb{E}_{h_\lambda} [\mathbb{1}_{\mathcal{F}_x}(X) w_X(X)^2]. \quad (1.50)$$

However, this optimization strategy requires sampling with respect to the instrumental distribution at each optimization iteration, which was overcome by a different approach.

The “cross-entropy” (CE) method uses Kullback-Leibler (KL) divergence to optimize importance sampling. KL divergence is a dissimilarity measure between distributions, expressed between the parametric instrumental distribution h_λ and the optimal one h_{opt} :

$$D_{\text{KL}}(h_{\text{opt}} || h_\lambda) = \int_{\mathcal{D}_x} \log \left(\frac{h_{\text{opt}}(\mathbf{x})}{h_\lambda(\mathbf{x})} \right) h_{\text{opt}}(\mathbf{x}) d\mathbf{x} \quad (1.51a)$$

$$= \int_{\mathcal{D}_x} \log(h_{\text{opt}}(\mathbf{x})) h_{\text{opt}}(\mathbf{x}) d\mathbf{x} - \int_{\mathcal{D}_x} \log(h_\lambda(\mathbf{x})) h_{\text{opt}}(\mathbf{x}) d\mathbf{x}. \quad (1.51b)$$

[Rubinstein and Kroese \(2004\)](#) simplify the expression of the optimization problem minimizing the KL divergence, which is most often convex and differentiable w.r.t. $\boldsymbol{\lambda}$:

$$\boldsymbol{\lambda}^* = \arg \min_{\boldsymbol{\lambda} \in \mathcal{D}_\lambda} D_{\text{KL}}(h_{\text{opt}} || h_\lambda). \quad (1.52)$$

By injecting the expression in Eq. (1.51b), the optimization problem simply becomes function of an expected value over the initial density f_X :

$$\lambda^* = \arg \max_{\lambda \in \mathcal{D}_\lambda} \int_{\mathcal{D}_x} \log(h_\lambda(\mathbf{x})) h_{\text{opt}}(\mathbf{x}) d\mathbf{x} = \arg \max_{\lambda \in \mathcal{D}_\lambda} \mathbb{E}_{f_X} [\mathbb{1}_{\mathcal{F}_X}(\mathbf{X}) \log(h_\lambda(\mathbf{X}))]. \quad (1.53)$$

To directly estimate this expected value, the failure probability p_f should not be too rare, which allows to use an empirical estimator of the expected value:

$$\lambda^* = \arg \max_{\lambda \in \mathcal{D}_\lambda} \sum_{i=1}^n \mathbb{1}_{\mathcal{F}_X}(\mathbf{x}^{(i)}) \log(h_\lambda(\mathbf{x}^{(i)})), \quad \{\mathbf{x}^{(i)}\}_{i=1}^n \stackrel{\text{i.i.d.}}{\sim} f_X. \quad (1.54)$$

Eventually, this optimization can be solved by cancelling the gradient:

$$\sum_{i=1}^n \mathbb{1}_{\mathcal{F}_X}(\mathbf{x}^{(i)}) [\nabla \log(h_{\lambda^*})](\mathbf{x}^{(i)}) = \mathbf{0}. \quad (1.55)$$

According to Rubinstein and Kroese (2004), this system of equations has a unique analytical solution when assuming that the instrumental distribution belongs to the “natural exponential family”.

However, when dealing with rare probabilities, the empirical estimation does not draw enough points in the failure domain to get an accurate estimate. The adaptive version of this technique, called *multilevel cross-entropy*, gradually builds a set of intermediate levels, decreasing towards the failure level (equal to zero). By working on a set of individually less rare events, the empirical estimation in Eq. (1.53) is made possible.

The algorithm starts by generating and evaluating an initial sample $\{g(\mathbf{X}_{[1]}^{(i)})\}_{i=1}^n$, on which a threshold level $q_{[1]}^{p_0}$ is computed as the empirical p_0 -quantile. Using the samples below the first threshold $q_{[1]}^{p_0}$, a first instrumental distribution $h_{\lambda_{[1]}^*}$ is optimized. At the next steps $k \in \{1, \dots, k_{\#}\}$, the sample $\{\mathbf{X}_{[k]}^{(i)}\}_{i=1}^n$ is generated from the density $h_{\lambda_{[k-1]}^*}$ and the rest of the process repeats until the estimated threshold level becomes negative, $q_{[k_{\#}]}^{p_0} \leq 0$.

The final instrumental density $h_{\lambda_{[k_{\#}]}^*}$ is then considered for importance sampling as defined in Eq. (1.46):

$$\hat{p}_f^{\text{CE-AIS}} = \frac{1}{n} \sum_{i=1}^n \mathbb{1}_{\{g(\mathbf{x}) \leq 0\}} \frac{f_X(\mathbf{x}_{[k_{\#}]}^{(i)})}{h_{\lambda_{[k_{\#}]}^*}(\mathbf{x}_{[k_{\#}]}^{(i)})}, \quad \{\mathbf{X}_{[k_{\#}]}^{(i)}\}_{i=1}^n \stackrel{\text{i.i.d.}}{\sim} h_{\lambda_{[k_{\#}]}^*}. \quad (1.56)$$

CE-AIS is widely used in rare event estimation, as it develops an adaptive technique while conserving the explicit IS variance given in Eq. (1.47). According to Rubinstein and Kroese (2004), the successive instrumental distributions $h_{\lambda_{[k]}^*}$ converge towards h_{opt} under a few hypotheses. The most important one is that the optimal density must belong to the parametric family considered, which should offer enough flexibility to describe a wide range of distributions.

When failure domain is composed of multiple regions, different improvements of the CE-AIS were proposed. [Kurtz and Song \(2013\)](#) proposed to optimize h_{λ^*} among a mixture of Gaussian distributions. This method was further studied by [Wang and Song \(2016\)](#) and [Papaioannou et al. \(2019\)](#) using advanced mixtures in the standard space. However, when using mixtures, the optimization problem does not have an analytical expression anymore ([Geyer et al., 2019](#)).

In the parametric framework, the family choice leads to a complicated trade-off between optimization complexity and flexibility allowed by the family. A similar mechanism is used by other importance sampling methods, inferring the optimal instrumental density by applying kernel density estimation to the points in the failure domain.

Nonparametric adaptive importance sampling

The use of multivariate kernel density estimation (KDE) to approximate the importance sampling optimal density h_{opt} was introduced in the context of structural reliability by [Ang et al. \(1992\)](#), latter followed by [Zhang \(1996\)](#). Let us first present the nonparametric importance sampling from [Zhang \(1996\)](#), considering the instrumental density h_0 (for now, $h_0 \neq f_X$), on which a sample $\{\mathbf{X}_{[1]}^{(i)}\}_{i=1}^n$ is generated. A first failure probability can be roughly estimated, assuming that enough samples lead to the failure domain:

$$\widehat{p}_{f[1]} = \frac{1}{n} \sum_{i=1}^n \mathbb{1}_{\{g(\mathbf{x}) \leq 0\}} \left(\mathbf{x}_{[1]}^{(i)} \right) \frac{f_X \left(\mathbf{x}_{[1]}^{(i)} \right)}{h_0 \left(\mathbf{x}_{[1]}^{(i)} \right)} = \frac{1}{n} \sum_{i=1}^n \mathbb{1}_{\{g(\mathbf{x}) \leq 0\}} \left(\mathbf{x}_{[1]}^{(i)} \right) w_{[1]}^{(i)}. \quad (1.57)$$

On this biased sample, another density can be fitted using KDE, using the previously defined $\widehat{p}_{f[1]}$ as a normalization term:

$$\widehat{h}_{[1]}(\mathbf{x}) = \frac{\det(\mathbf{H}_{[1]})^{-1/2}}{n \widehat{p}_{f[1]}} \sum_{i=1}^n \mathbb{1}_{\{g(\mathbf{x}) \leq 0\}} \left(\mathbf{x}_{[1]}^{(i)} \right) w_{[1]}^{(i)} K \left(\mathbf{H}_{[1]}^{-1/2} (\mathbf{x} - \mathbf{x}_{[1]}^{(i)}) \right). \quad (1.58)$$

Where the kernel K is commonly taken as the multivariate Gaussian centered density with the covariance matrix \mathbf{H} . The tuning of \mathbf{H} is usually done by minimizing an asymptotic mean integrated squared error (AMISE) criterion ([Glad et al., 2007](#)). In the previous expression, the normalization constant insures to build a probability density while the weights $w_{[1]}^{(i)}$, defined above, reflect the contribution of each point to $\widehat{p}_{f[1]}$. After performing this KDE, the estimated density can be used as instrumental density in Eq. (1.46).

As for the CE-IS methods, the risk is that barely any points sampled from the instrumental density h_0 hit the failure domain, leading to poor estimates. [Zhang \(1996\)](#) proposed to couple an adaptive mechanism with a nonparametric inference of the optimal density. This method is further referred to as NAIS for *nonparametric adaptive importance sampling*. Later, the NAIS method was adapted by [Morio \(2011\)](#) to the reliability analysis problem, using a similar mechanism to the CE-AIS method.

In this framework, a series of intermediate threshold are computed as empirical p_0 -quantiles $q_{[1]}^{p_0} > \dots > q_{[k_\#]}^{p_0}$ of the successive importance sampling steps. This algorithm is initiated by setting $h_0 = f_x$ and stops at the step $k_\#$, when $q_{[k_\#]}^{p_0} < 0$.

At the step k , the intermediate normalization constant is written as:

$$\widehat{p}_f[k] = \frac{1}{kn} \sum_{j=1}^k \sum_{i=1}^n \mathbb{1}_{\{g(\mathbf{x}) \leq q_{[j]}^{p_0}\}} \left(\mathbf{x}_{[j]}^{(i)} \right) \frac{f_x \left(\mathbf{x}_{[j]}^{(i)} \right)}{\widehat{h}_{[j-1]} \left(\mathbf{x}_{[j]}^{(i)} \right)} = \frac{1}{kn} \sum_{j=1}^k \sum_{i=1}^n \mathbb{1}_{\{g(\mathbf{x}) \leq q_{[j]}^{p_0}\}} \left(\mathbf{x}_{[j]}^{(i)} \right) w_{[j]}^{(i)}, \quad (1.59)$$

with $\left\{ \mathbf{x}_{[j]}^{(i)} \right\}_{i=1}^n \stackrel{\text{i.i.d.}}{\sim} h_{[j-1]}$. Then, an intermediate instrumental density is inferred by KDE on the samples exceeding the threshold $q_{[k]}^{p_0}$ such that:

$$\widehat{h}_{[k+1]}(\mathbf{x}) = \frac{\det(\mathbf{H}_{[k]})^{-1/2}}{kn \widehat{p}_f[k]} \sum_{j=1}^k \sum_{i=1}^n \mathbb{1}_{\{g(\mathbf{x}) \leq q_{[j]}^{p_0}\}} \left(\mathbf{x}_{[j]}^{(i)} \right) w_{[j]}^{(i)} K \left(\mathbf{H}_{[k]}^{-1/2} (\mathbf{x} - \mathbf{x}_{[j]}^{(i)}) \right). \quad (1.60)$$

The last instrumental density $\widehat{h}_{[k_\#]}$ is finally considered as an approximation of the optimal density for importance sampling introduced in Eq. (1.46):

$$\widehat{p}_f^{\text{NAIS}} = \frac{1}{n} \sum_{i=1}^n \mathbb{1}_{\{g(\mathbf{x}) \leq 0\}} \frac{f_x \left(\mathbf{x}_{[k_\#]}^{(i)} \right)}{\widehat{h}_{[k_\#]} \left(\mathbf{x}_{[k_\#]}^{(i)} \right)}, \quad \left\{ \mathbf{x}_{[k_\#]}^{(i)} \right\}_{i=1}^n \stackrel{\text{i.i.d.}}{\sim} h_{k_\#}. \quad (1.61)$$

Overall, the NAIS offers more flexibility to infer the optimal importance sampling density. This property might suit problems presenting highly nonlinear limit state function. Then, relying on importance sampling still provides an expression of the estimator's variance, by adapting Eq. (1.47) to the recurrent mechanism in NAIS. Because this approach depends on KDE, it inherits its drawbacks. As discussed in Morio (2011), tuning the KDE can create numerical issues and KDE famously suffers from the curse of dimension. In practice, the performances of NAIS seriously decrease for problems in dimension larger than ten.

Subset sampling

Although the concept of splitting already existed, the name of *subset sampling* (SS) was first introduced by Au and Beck (2001) in the structural reliability community. This concept was generalized as a sequential Monte Carlo method under the name of “adaptive multilevel splitting”, as reviewed by Cérou et al. (2019).

Subset sampling splits the failure event \mathcal{F}_x into an intersection of $k_\#$ intermediary events $\mathcal{F}_x = \cap_{k=1}^{k_\#} \mathcal{F}_{[k]}$. Each are nested such that $\mathcal{F}_{[1]} \supset \dots \supset \mathcal{F}_{[k_\#]} = \mathcal{F}_x$. The failure probability is then expressed as a product of conditional probabilities:

$$p_f = \mathbb{P}(\mathcal{F}_x) = \mathbb{P}(\cap_{k=1}^{k_\#} \mathcal{F}_{[k]}) = \prod_{k=1}^{k_\#} \mathbb{P}(\mathcal{F}_{[k]} | \mathcal{F}_{[k-1]}). \quad (1.62)$$

From a practical point of view, the analyst tunes the algorithm⁹ by setting the intermediary probabilities $\mathbb{P}(\mathcal{F}_{[k]} | \mathcal{F}_{[k-1]}) = p_0, \forall k \in \{1, \dots, k_{\#}\}$. Then, the corresponding quantiles $q_{[1]}^{p_0} > \dots > q_{[k_{\#}]}^{p_0}$ are estimated for each conditional subset samples $\mathbf{X}_{[k],N}$ of size N . Note that the initial quantile is estimated by crude Monte Carlo sampling on the input PDF f_X . Following conditional subset samples are generated by *Monte Carlo Markov Chain* (MCMC) sampling of $f_X(\mathbf{x} | \mathcal{F}_{[k-1]})$, using as seeds initialization points the $n = Np_0$ samples given by $\mathbf{A}_{[k],n} = \{\mathbf{X}_{[k-1]}^{(i)} \subset \mathbf{X}_{[k-1],N} | g(\mathbf{X}_{[k-1]}^{(i)}) > \hat{q}_{[k-1]}^{p_0}\}_{i=1}^n$. This process is repeated until an intermediary quantile becomes negative: $\hat{q}_{[k_{\#}]}^{p_0} < 0$. Finally, the failure probability is estimated by:

$$\hat{p}_f^{\text{SS}} = p_0^{k_{\#}-1} \frac{1}{N} \sum_{i=1}^n \mathbb{1}_{\{g(\mathbf{x}) \leq 0\}}(\mathbf{X}_{[k_{\#}],N}^{(i)}). \quad (1.63)$$

In practice, the subset sample size should be large enough to properly estimate intermediary quantiles, leading to the usual recommendation of $p_0 = 0.1$. Fig. 1.11 illustrates the consecutive subset samples moving towards the failure domain. At each step of the algorithm (corresponding to a color), a subset is generated and an intermediate quantile estimated.

Au and Beck (2001) also provide bounds to the coefficient of variation of \hat{p}_f^{SS} . The first one results from a first order Taylor expansion of Eq. (1.63) and is often considered as an upper bound. While the second assumes the estimations of the conditional probabilities to be independent, and tends to underestimate the coefficient of variation.

As discussed in (Papaioannou et al., 2015), the efficiency of the SS method depends on the choice and tuning of the MCMC algorithm. The Metropolis–Hastings (MH) algorithm is widely used as MCMC algorithm for subset sampling, however, it quickly becomes inefficient as the dimension increases. Different improvements of the MH are made possible by working in the standard space, such as the “component-wise” (or “modified M–H”). More recently, alternative MCMC methods including physical system dynamics (e.g., Hamiltonian MCMC) showed promising results in high-dimension reliability problems (Papakonstantinou et al., 2023).

The subset sampling is a versatile method, presenting consistent performances even for rare probabilities. Its flexibility allows dealing with highly nonlinear LSF, but its drawbacks arise from the use of MCMC sampling. The convergence of MCMC is complex to control and depends on its tuning, in addition, the MCMC samples are dependent. Unlike the methods derived from importance sampling, the variance of \hat{p}_f^{SS} is only approximated.

1.5.3 Summary and discussion

This section introduced the generic formulation and the main methods for rare event estimation. Even if the problem is generic rare event estimation requires tailored solutions. Depending on the properties of the problem tackled, some methods might outperform others. Beyond the one introduced previously, many more methods are worth mentioning in the field of reliability analysis, such as the *directional sampling* Bjerager (1988), or *line sampling* (Koutsourelakis,

⁹An algorithmic presentation of the generic subset sampling method is given in Appendix ??.

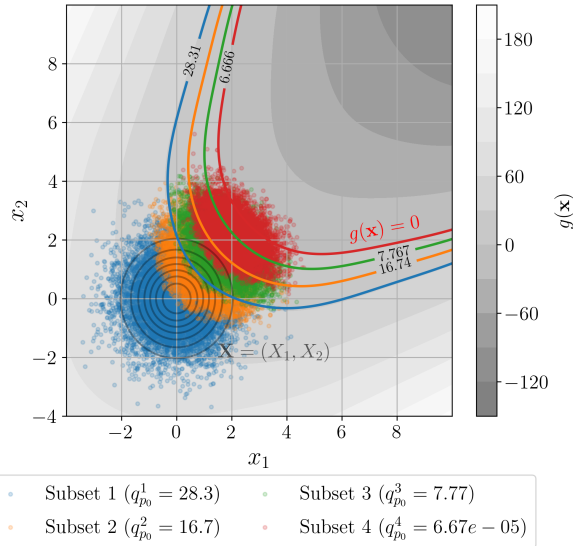


Figure 1.11 Illustration of a rare event estimation by subset sampling ($n = 4 \cdot 10^4, p_0 = 0.1$).

2004), moving particles (Walter, 2015). Morio and Balesdent (2015) compares the advantages and drawbacks of the most commonly used one, with corresponding algorithmic descriptions and numerical benchmarks.

Overall, the main properties increasing the complexity of reliability problems are related to:

- the computational cost of the limit-state function evaluation;
- the strong nonlinearity of the limit-state function;
- the rareness of the failure event.

In regard to the methods, the estimation is made easier by algorithms with simple tuning or allowing to work in the physical space (avoiding a possibly complex iso-probabilistic transform). Considering all these elements the analyst may set up a sampling strategy, possibly coupled with the use of a surrogate model (further discussed in Section 1.7).

Nevertheless, the unified formulation of reliability analysis problems (see 1.31) is an opportunity for the community to share standardized benchmark problems. Following the well-accepted benchmark platform for optimization “Comparing Continuous Optimizers” (COCO) (Hansen et al., 2021), an equivalent initiative was proposed for structural reliability. In 2019, the “black-box reliability challenge”, was organized as a hackathon by the Dutch organization for applied scientific research (TNO) (Rozsas and Slobbe, 2019). This platform proposed a large catalog of reliability problems with their respective solutions. Most of them were encapsulated as a Python package called `otbenchmark`¹⁰ (Fekhari et al., 2021), based on core OpenTURNS objects.

When working with computationally expensive numerical models, the direct use of rare event estimation methods is most often intractable. Many contributions were dedicated to the coupling of surrogate models with sampling methods for rare event estimation. Moustapha et al.

¹⁰<https://github.com/mbaudin47/otbenchmark/>

(2022) presented the results of a wide benchmark on the challenge from TNO, obtained by using surrogate models for reliability developed in the UQLab software (Marelli and Sudret, 2014).

In any case, risk assessment analysts should favor the methods offering convergence guarantees over punctual performance demonstrations. Finally, the robustness of the failure probability to the input uncertainty model is a major question, which was studied from probabilistic (Lemaître et al., 2015) and extra-probabilistic (Ajenjo et al., 2022) frameworks.

OpenTURNS 4 (Rare event estimation). The Python code available in Appendix ?? proposes a minimalistic OpenTURNS example to estimate rare event probabilities. Figures illustrating the present section may be reproduced, using the OpenTURNS scripts available on GitHub¹¹.

1.6 Global sensitivity analysis

The aim of sensitivity analysis (SA) is to determine the impact of a single (or a group of random inputs) on a random output(s). As described earlier, this step is qualified as an inverse analysis in the general UQ framework (illustrated in Fig. 1), in opposition with the forward uncertainty propagation step. In fact, the analyst studies the effect of the inputs at different scales, hence the distinction between “local” and “global” SA. Local SA focuses on the impact of small perturbations around nominal values of the inputs (i.e., derivative-based approaches), while global sensitivity analysis (GSA), typically studies the general variability (e.g., the variance) of the output. Two types of GSA methods exist in the literature, either proposing qualitative and quantitative approaches:

- *screening methods*: determines the non-influential variables in a UQ study (qualitative);
- *importance measures*: assess the contribution of inputs in the global variability of the output (quantitative).

Screening methods are typically used in a statistical learning process, to drop the irrelevant variables to the learning. In this context, *feature selection* serves the same purpose with a slight difference. Screening methods usually assume the inputs to be independent while feature selection does not. Moreover, feature selection not only looks for the irrelevant features to the learning but also the redundant features (Fan and Lv, 2010).

The global sensitivity of an output can be explained by different elements: the single variability of the inputs, their dependence, and their interactions. Two variables present interactions when their simultaneous effect on an output is not additive. Note that SA on dependent inputs is an active field of research and the inputs will mostly be considered as independent in the following.

¹¹https://github.com/efekhari27/thesis/blob/main/numerical_experiments/chapter1/reliability.ipynb

1.6.1 Screening methods

Many UQ methods suffer from the curse of dimensionality, thankfully, high-dimensional problems often only depend on a few variables. This observation was formalized with the concept of *effective dimension* introduced by [Owen \(2003\)](#). Screening methods allow to discriminate the non-influential variables, which can be considered afterwards as determinist to simplify the problem.

Morris method

The Morris method ([Morris, 1991](#)) is a screening method historically used in engineering applications. It starts by mapping the input domain \mathcal{D}_X into a unit hypercube $[0, 1]^d$, which is discretized as a regular grid with step $\Delta \in \mathbb{R}$. The algorithm computes local elementary sensitivity by building “one at a time” (OAT) local trajectories over the regular grid. Each OAT design starts at a random node $\mathbf{x}^{(t)} = (x_1^{(t)}, \dots, x_j^{(t)}, \dots, x_d^{(t)})$ of the grid, and moves only in one direction by an increment equal to the elementary step such that: $\mathbf{x}^{(t)} + \Delta_j = (x_1^{(t)}, \dots, x_j^{(t)} + \Delta, \dots, x_d^{(t)})$. The elementary effect in the direction of the variable i from a OAT trajectory t is expressed as a finite difference:

$$\text{EE}_j^{(t)} = \frac{g(\mathbf{x}^{(t)}) - g(\mathbf{x}^{(t)} + \Delta_j)}{\Delta}. \quad (1.64)$$

The Morris method generates $T \in \mathbb{N}$ OAT trajectories and computes theirs respective elementary effects in each direction i . To assess the global sensitivity of the function, the mean $\overline{\text{EE}}_j$ and variance $\widehat{\text{Var}}(\text{EE}_j)$ of the elementary effects are computed:

$$\overline{\text{EE}}_j = \frac{1}{n} \sum_{t=1}^T |\text{EE}_j^{(t)}|, \quad \widehat{\text{Var}}(\text{EE}_j) = \frac{1}{n-1} \sum_{t=1}^T \left(\text{EE}_j^{(t)} - \overline{\text{EE}}_j \right)^2. \quad (1.65)$$

It allows to divide the variables into three categories, regardless of any regularity hypothesis on the function: (i) negligible effects; (ii) linear effects without interaction; and (iii) nonlinear effects with possible interactions. This method is very intuitive but quickly shows its limits as the dimension increases since it relies on a discretization of the space by a regular grid. Another disadvantage of this method is that it does not distinguish interactions and nonlinear effects of inputs.

Derivative-based global sensitivity measures

The Derivative-based global sensitivity measures (DGSM) are a GSA method introduced in [Sobol and Gresham \(1995\)](#) and further studied in [Kucherenko et al. \(2009\)](#). As the Morris method, they study the mean value of local derivatives of the model output with regard to the inputs:

$$v_j = \int_{\mathcal{D}_X} \left(\frac{\partial g(\mathbf{x})}{\partial x_j} \right)^2 f_X(\mathbf{x}) d\mathbf{x} = \mathbb{E} \left[\left(\frac{\partial g(\mathbf{X})}{\partial X_j} \right)^2 \right]. \quad (1.66)$$

This continuous formulation does not require using OAT designs, which was proven to be more efficient when exploiting sampling methods such as quasi-Monte Carlo. The efficiency of the DGSMs for screening purposes was outlined in many papers (e.g., [Kucherenko and Iooss \(2017\)](#)). Since their value depends on the probability distribution of the input, a normalized version was developed. The connections between DGSM and variance-based GSA measures (i.e., Sobol' indices introduced hereafter), revealed bounding properties between DGSMs and Sobol' total indices ([Lamboni et al., 2013](#)).

1.6.2 Variance-based importance measures

Screening methods determine the non-influential variables in a UQ problem. Beyond this information, importance measures quantify the influence of inputs, allowing to rank the inputs according to their contribution to the output variability.

Functional variance decomposition and Sobol' indices

Sobol' indices are the most popular importance measure in GSA. Their universality comes from the functional decomposition of the output's variance, attributing variance share to the inputs. Considering a squared-integrable and measurable function $g(\cdot)$ and an independent random vector \mathbf{X} . The output random variable $Y = g(\mathbf{X})$ can be decomposed, according to [Hoeffding \(1948\)](#), as:

$$Y = g(\mathbf{X}) = g_0 + \sum_{j=1}^d g_j(X_j) + \sum_{j < l}^d g_{jl}(X_j, X_l) + \dots + g_{1\dots d}(\mathbf{X}), \quad (1.67)$$

with the previous terms defined according this recurrence:

$$g_0 = \mathbb{E}[g(\mathbf{X})] \quad (1.68a)$$

$$g_j(X_j) = \mathbb{E}[g(\mathbf{X})|X_j] - g_0 \quad (1.68b)$$

$$g_{jl}(X_j, X_l) = \mathbb{E}[g(\mathbf{X})|X_j, X_l] - g_j(X_j) - g_l(X_l) - g_0 \quad (1.68c)$$

$$\dots \quad (1.68d)$$

Sobol in [Sobol' \(1993\)](#) proved that this decomposition is unique by exploiting the orthogonality of the terms of the decomposition. Therefore, this decomposition can be transposed in terms of functional decomposition of variance (also called functional analysis of variance or FANOVA):

$$\text{Var}(Y) = \sum_{j=1}^d V_j(Y) + \sum_{j < l}^d V_{jl}(Y) + \dots + V_{1\dots d}(Y), \quad (1.69)$$

where the previous terms are defined in a recurrent way, in the same fashion as Eq. (1.68): $V_j(Y) = \text{Var}(\mathbb{E}[Y|X_j])$, $V_{jl}(Y) = \text{Var}(\mathbb{E}[Y|X_j, X_l]) - V_j(Y) - V_l(Y)$, and so on for higher order interaction

terms. The Sobol' indices of different order are defined as normalized shares of variance. The *first-order Sobol' index* S_j quantifies the share of variance of the output only explained by the marginal X_j (also called main effect). Second order S_{jl} (or higher order) Sobol' indices quantify the effect of the interactions between a group of marginals.

$$S_j = \frac{V_j(Y)}{\text{Var}(Y)} = \frac{\text{Var}(\mathbb{E}[Y|X_j])}{\text{Var}(Y)} \quad (1.70a)$$

$$S_{jl} = \frac{V_{jl}(Y)}{\text{Var}(Y)} = \frac{\text{Var}(\mathbb{E}[Y|X_j, X_l]) - V_j(Y) - V_l(Y)}{\text{Var}(Y)} \quad (1.70b)$$

$$\dots \quad (1.70c)$$

The generic definition of the Sobol' sensitivity indices associated to a subset of inputs $A \in \mathcal{P}_d$, with \mathcal{P}_d the set of all possible subsets of $\{1, \dots, d\}$, is given by:

$$S_A = \frac{V_A(Y)}{\text{Var}(Y)} = \frac{\sum_{B \subset A} (-1)^{|A|-|B|} \text{Var}(\mathbb{E}[Y|X_B])}{\text{Var}(Y)}. \quad (1.71)$$

By using the functional decomposition of variance in Eq. (1.69), one can show that the Sobol' indices add up to one:

$$\sum_{A \in \mathcal{P}_d} S_A = 1. \quad (1.72)$$

The so-called *closed Sobol' index* associated to a subset of inputs $A \in \mathcal{P}_d$ (equivalent to the first-order Sobol' index of A) is defined as:

$$S_A^{\text{clos}} = \sum_{A' \subset A} S_{A'} = \frac{\text{Var}(\mathbb{E}[Y|X_A])}{\text{Var}(Y)}. \quad (1.73)$$

Assessing Sobol' indices for every order becomes complex in medium to high dimension. The *total Sobol' index* S_j^T associated with the variable j , see Saltelli et al. (2008), quantifies the share of output variance which is explained by all the interactions of the variable X_j :

$$S_j^T = 1 - \frac{\text{Var}(\mathbb{E}[Y|X_{-j}])}{\text{Var}(Y)} = \frac{\mathbb{E}[\text{Var}(Y|X_{-j})]}{\text{Var}(Y)}, \quad (1.74)$$

where X_{-j} represents all the marginals from X but X_j . This definition can also be generalized for a subset of inputs $A \in \mathcal{P}_d$, such that:

$$S_A^T = 1 - S_{A^C}^{\text{clos}} = 1 - \frac{\text{Var}(\mathbb{E}[Y|X_{A^C}])}{\text{Var}(Y)}, \quad A^C = \mathcal{P}_d \setminus A \quad (1.75)$$

By analyzing jointly the first and total Sobol' indices, one can get an indication on the decomposition between the marginal and interaction effects. Note that the total indexes are only equal to the first indexes when the model does not present interactions (i.e., purely additive model).

Estimating Sobol' indices can be achieved in various ways, even if historically the *pick-freeze* scheme was the most popular. This method is based on two samples, but it often requires a prohibitive number of evaluations of the function. Many estimators using the pick-freeze generic scheme were developed to estimate Sobol' indices (e.g., Saltelli's, Jansen's, Martinez's etc.), see further details in the Chapter 3 of Da Veiga et al. (2021). Alternatively, the surrogate models were exploited to estimate such sensitivity measure. Using an input-output dataset, the analyst may build a *polynomial chaos expansion* (PCE) surrogate model, which gives an explicit expression of the Sobol' indices (Sudret, 2008). Authors such as Marrel et al. (2009) also studied the use of Gaussian processes for this purpose.

In the case of independent inputs, the first and total Sobol' indices is a complete tool for GSA. The main advantage of this approach is the quantitative nature of its results, allowing to objectively compare the effect of input variables. When the inputs present a dependence structure, it becomes complicated to distinguish its effects from possible interactions. However, many authors tried to adapt the Sobol's indices to this context. Chapter 5 of Da Veiga et al. (2021) reviews four of these approaches. For example, Mara and Tarantola (2012) proposed two extra Sobol' indices, called "full indices", detecting the contributions associated with the inputs' dependence. Note that the interpretation and estimation of this solution becomes complicated. Moreover, unlike the independent case, the four Sobol' indices do not divide the output variance between the inputs. Beyond Sobol' indices, another important GSA method was adapted from the theory of Shapley values by Owen (2014), allowing to work with dependent inputs.

OpenTURNS 5 (Sobol' indices). The Python code available in Appendix ?? gives a minimalist OpenTURNS implementation of the Sobol' indices to assess global sensitivity analysis on the Ishigami analytical problem. Further scripts are also available on GitHub¹².

Shapley effects

Shapley effects are an adaptation to GSA by Owen (2014) of the Shapley values from the cooperative games' theory (Shapley et al., 1953). This method is an alternative to the Sobol' indices in the case of dependent inputs, for which the natural interpretation of single interaction effects no longer holds. In the game theory, Shapley values act as a rule on how to share the value created by a team between its members (players). The Shapley value allocated to the player X_j is given considering the indices $\{1, \dots, d\} \setminus \{j\}$:

$$\varsigma_j = \sum_{A \subset \{1, \dots, d\} \setminus \{j\}} \binom{d-1}{\text{card}(A)}^{-1} (\text{val}(A \cup \{j\}) - \text{val}(A)), \quad (1.76)$$

where the value (or cost) function is denoted by $\text{val}(A)$, and A is a subset of $\{1, \dots, d\}$ with cardinality $\text{card}(A)$. The Shapley effects adapted this concept to perform a GSA by considering

¹²https://github.com/efekhari27/thesis/blob/main/numerical_experiments/chapter1/sensitivity_analysis.ipynb

the variables as players and the closed Sobol' indices for the value function:

$$Sh_j = \sum_{A \subset -\{j\}} \binom{d-1}{|A|}^{-1} \left(S_{A \cup \{j\}}^{\text{clos}} - S_A^{\text{clos}} \right). \quad (1.77)$$

Conceptually, this expression compares a performance defined by a cost function with or without the variable X_j , and averages it over all the possible combinations of inputs. This importance measure offers the following decomposition:

$$\sum_{j=1}^d Sh_j = 1. \quad (1.78)$$

In the case of independent inputs, the Shapley effects present properties related to the Sobol' indices. The following equation (see proof in [Owen \(2014\)](#)) reveal that the Shapley effects equally divide the interaction effects between the implicated variable:

$$S_j \leq Sh_j \leq S_j^T, \quad Sh_j = \sum_{A \in \mathcal{P}_d, j \in A} \frac{S_A}{\text{card}(A)}. \quad (1.79)$$

Unlike the Sobol' indices, Shapley effects are a nonnegative allocation of output variance with equitable division of the interaction effects. This method presents an interesting alternative in the dependent case, however, estimating Shapley effects creates computational difficulties. The reader may refer to the permutation-based algorithm from [Song et al. \(2016\)](#). Surrogate models were also coupled to estimate Shapley effects, using Gaussian processes in [Benoumechiara and Elie-Dit-Cosaque \(2019\)](#) and random forests in [Bénard et al. \(2022\)](#).

Shapley effects are a promising importance measure based on variance allocation. However, in some cases the variance of the output distribution does not represent well its variability (e.g., multimodal distribution). The following section introduces another family of GSA methods based on distances between distributions.

1.6.3 Moment-independent importance measures

Beyond variance-based GSA, many types of distances between distributions have been used to evaluate the dependence between the input and output distributions. Comparing the entire distributions instead of their moments might be more robust in some cases (e.g., when the variance is a poor indicator of the variability). The tools used to do so are generally called *dissimilarity measures* between distributions. Appendix ?? briefly introduces two families of dissimilarity measures: the class of f -Csiszár divergences (e.g., the Kullback-Leibler divergence, total variation distance) and the class of integral probability metrics (IPM) (e.g., Wasserstein distance, total variation distance, maximum mean discrepancy).

Considering the probability measures \mathbb{P}_{X_j} and \mathbb{P}_Y (associated with the random variables X_j and Y) and a dissimilarity measure $\Delta(\cdot, cdot)$, one can define two formulations for GSA:

- directly using a dissimilarity measure to assess $\Delta(\mathbb{P}_Y, \mathbb{P}_{Y|X_j})$;
- building a *dependence measures* evaluating $\Delta(\mathbb{P}_{(X_j, Y)}, \mathbb{P}_{X_j} \otimes \mathbb{P}_Y)$.

The first approach was studied in association with f -divergences in Da Veiga (2015); Rahman (2016). However, some f -divergences introduce estimation issues, and the resulting importance measures do not propose a functional decomposition of variance (also called FANOVA). Using kernel-based IPMs such as the maximum mean discrepancy (MMD), an alternative importance measure was proposed. The following section presents the *Hilbert-Schmidt Independence Criterion* (HSIC), which was initially introduced by Gretton et al. (2006) for dependence testing, and later adapted as a dependence measure in GSA by Da Veiga (2015).

Hilbert-Schmidt independence criterion

Let us first recall the definition of the maximum mean discrepancy (further discussed in Appendix ??). This distance between two probability distributions π and ζ can be defined as the worst-case error for any function within a unit ball of a function space \mathcal{H} :

$$\text{MMD}(\pi, \zeta) := \sup_{\|g\|_{\mathcal{H}(k)} \leq 1} \left| \int_{\mathcal{D}_X} g(\mathbf{x}) d\pi(\mathbf{x}) - \int_{\mathcal{D}_X} g(\mathbf{x}) d\zeta(\mathbf{x}) \right| \quad (1.80)$$

This quantity is a distance in the RKHS by taking a characteristic kernel (e.g., the Gaussian or Matérn kernel). After a calculation developed in Appendix ??, an unbiased one-sample estimator of the squared-MMD was proposed by Gretton et al. (2006), with a convergence rate of $O(n^{-1/2})$ in probability. Considering the two-samples $\{\pi^{(i)}\}_{i=1}^n \sim \pi$ and $\{\zeta^{(j)}\}_{j=1}^n \sim \zeta$:

$$\widehat{\text{MMD}}^2(\pi, \zeta) = \frac{1}{n(n-1)} \sum_{i=1}^n \sum_{j \neq i}^n k(\pi^{(i)}, \pi^{(j)}) - k(\pi^{(i)}, \zeta^{(j)}) - k(\zeta^{(i)}, \pi^{(j)}) + k(\zeta^{(i)}, \zeta^{(j)}), \quad (1.81)$$

In the context of GSA, a first option is to directly use this dissimilarity measure to define the unnormalized index:

$$S_j^{\text{MMD}} = \text{MMD}(\mathbb{P}_Y, \mathbb{P}_{Y|X_j}). \quad (1.82)$$

da Veiga (2021) remarked that the unnormalized first order Sobol' indices are recovered by taking the linear kernel on the output $k_Y(y, y') = yy'$. Using this non-characteristic kernel (see the definition in Appendix ??) brings us back to a moment-dependent importance measure.

Alternatively, the second option considers a couple of random variables (X_j, Y) , with probability distributions \mathbb{P}_{X_j} and \mathbb{P}_Y , and assumes the RKHS \mathcal{H} induced by the tensor product kernel $k((x_j, y), (x'_j, y')) = k_{X_j}(x_j, x'_j)k_Y(y_j, y'_j)$. The *Hilbert-Schmidt independence criterion* (HSIC) measures the dependence between \mathbb{P}_{X_j} and \mathbb{P}_Y by expressing the MMD between $\mathbb{P}_{(X_j, Y)}$ and $\mathbb{P}_{X_j} \otimes \mathbb{P}_Y$:

$$\text{HSIC}(X_j, Y) = \text{MMD}^2(\mathbb{P}_{(X_j, Y)}, \mathbb{P}_{X_j} \otimes \mathbb{P}_Y). \quad (1.83)$$

This technique showed very good results for screening, and corresponding independence tests were studied for screening in [De Lozzo and Marrel \(2016\)](#).

[da Veiga \(2021\)](#) proposed the functional decomposition of the two indices defined in Eq. (1.82) and Eq. (1.83), allowing to develop their respective normalized versions. Note that the HSIC decomposition requires a specific hypothesis on the structure of the kernel associated to the inputs.

1.6.4 Summary and discussion

This section introduced the GSA methods commonly used in uncertainty quantification. Either to reduce the dimension of a problem (screening) or to quantify the influence of inputs (with importance measures), GSA improves the understanding of an uncertainty quantification study. As for other steps of the generic UQ methodology, SA is made more complicated for computationally costly simulation models, hence the use of surrogates models. Additionally, the dependence between inputs still represents an important limit to interpret GSA results.

Alongside rare event estimation, a literature is dedicated to the influence of the random inputs on such tail statistics. The sensitivity is no more qualified as “global” but becomes “goal-oriented”. In the field of structural reliability, an overview of the reliability-oriented sensitivity analysis methods is presented in [Chabridon \(2018\)](#). Several techniques derive from rare event estimation (e.g., the FORM importance factors [Papaioannou and Straub \(2021\)](#)), or were adapted from GSA, like Sobol’ indices ([Ehre et al., 2020](#)), Target-HSIC ([Marrel and Chabridon, 2021](#)), or Shapley effects ([Demange-Chryst et al., 2023](#)).

Finally, sensitivity analysis may describe the effects of random inputs on the variation of the output, however, this study is done considering by assuming a model on the input uncertainties. The role of a regulatory agency auditing an uncertainty quantification approach for certification (i.e., a nuclear safety authority), might be to challenge the way to model the uncertainties on the inputs. In this case, various tools for *robustness analysis* exist to quantify the impact of misspecifying the random inputs on the quantity of interest studied. Among the methods to perturbate uncertainty models, some remain in the probabilistic framework, such as the “perturbed-law based indices” (PLI) ([Lemaître et al., 2015](#)), or on extra-probabilistic methods ([Ajenjo et al., 2022](#)).

1.7 Surrogate modeling

1.7.1 Common framework

The aim of *surrogate modeling* (or metamodeling) is to build a cheap-to-call statistical model, denoted by $\widehat{g}_n(\cdot)$, replacing a costly numerical model $g(\cdot)$ over the input domain \mathcal{D}_X . To do so, a statistical learning is performed on a finite number of observations of the costly function g . When manipulating computationally expensive simulations, its size can be limited (i.e.,

small-data context). This n -sized set is usually called *learning set* written:

$$\{\mathbf{X}_n, \mathbf{y}_n\} = \left\{ \mathbf{x}^{(i)}, y^{(i)} \right\}_{i=1}^n = \left\{ \mathbf{x}^{(i)}, g(\mathbf{x}^{(i)}) \right\}_{i=1}^n. \quad (1.84)$$

A very large catalog of regression methods exist, here is a list of the most encountered ones in the field of UQ: generalized linear regression, polynomial chaos expansion (PCE) (Soize and Ghanem, 2004; Blatman and Sudret, 2011), support vector machine (SVM) (Cortes and Vapnik, 1995), Gaussian processes (GP) (Rasmussen and Williams, 2006), low-rank tensor approximations (Grasedyck et al., 2013), and artificial neural network (ANN) (Hastie et al., 2009). The following section will provide a short focus on Gaussian process regression.

Validating the accuracy and precision of a surrogate model is an important step to guaranty its fidelity with regard to the numerical model. When an m -sized input-output set is dedicated to validating the surrogate model, independently of the learning set, it is called *test set* and denoted by $\{\mathbf{X}_m, \mathbf{y}_m\} = \left\{ \mathbf{x}^{(i)}, g(\mathbf{x}^{(i)}) \right\}_{i=1}^m$. Note that the analyst may work in two different frameworks, affecting the regression and validation method's choice:

- Given-data context: only using a fixed input-output dataset to build and validate the surrogate model.
- Computer experiment context: allowing to generate simulated data points (often at a certain cost).

Validating surrogate models in small-data context appears to be an important challenge. Different validation criteria and techniques exist. The *coefficient of validation*, denoted by R^2 , is a first validation metric that can be directly computed on the learning set:

$$R^2(\hat{g}_n) = 1 - \frac{\sum_{i=1}^n (y(\mathbf{x}^{(i)}) - \hat{g}(\mathbf{x}^{(i)}))^2}{\sum_{i=1}^n (y(\mathbf{x}^{(i)}) - \bar{y}_n)^2}, \quad (1.85)$$

where $\bar{y}_n = (1/n) \sum_{i=1}^n y^{(i)}$ denotes the empirical mean of the observations in the test sample. However, such metrics are not relevant for every regression method (typically, interpolant method have an $R^2 = 1$). The *predictivity coefficient* is an alternative defined as a normalized *integrated square error* (ISE):

$$Q^2(\hat{g}_n) = 1 - \frac{\text{ISE}(\hat{g}_n)}{\text{Var}(\hat{g}_n)}, \quad (1.86)$$

where

$$\text{ISE}(\hat{g}_n) = \int_{\mathcal{D}_X} (g(\mathbf{x}) - \hat{g}(\mathbf{x}))^2 d\mathbf{x}, \quad \text{Var}(\hat{g}_n) = \int_{\mathcal{D}_X} (g(\mathbf{x}) - \hat{g}(\mathbf{x}))^2 d\mathbf{x}. \quad (1.87)$$

This quantity can be estimated on a test set $\{\mathbf{X}_m, \mathbf{y}_m\}$:

$$\widehat{Q}^2(\hat{g}_n) = 1 - \frac{\sum_{i=1}^m (y(\mathbf{x}^{(i)}) - \hat{g}(\mathbf{x}^{(i)}))^2}{\sum_{i=1}^m (\bar{y}_m - y(\mathbf{x}^{(i)}))^2}. \quad (1.88)$$

Note that for either criteria, the higher the value, the better the quality of the fit.

Validating a surrogate model with an independent test-set is sometimes called *holdout* validation. In a small-data context, dedicating an independent test set to validation might be impossible. Then, *cross-validation* is a generic estimation strategy allowing to use only one sample for learning and testing. The most common cross-validation method is the *k-fold* validation, illustrated in Fig. 1.12. The idea is first to split the n -sized dataset in several equal parts, called folds. A first surrogate can be fitted on all the dataset but the first fold, on which a validation criterion is estimated (i.e., performance metric). The operation is repeated for each fold, providing a virtual validation on the entire dataset. Leave-One-Out validation (LOO) is an extreme case of *k*-fold cross-validation, for which $k = n - 1$. Note that multiple variations of these methods exist, for example by adding a permutation or shuffling step. The “bagging” validation method (for “bootstrap aggregating”) consists of a shuffled cross-validation repeated many times (Breiman, 1996).

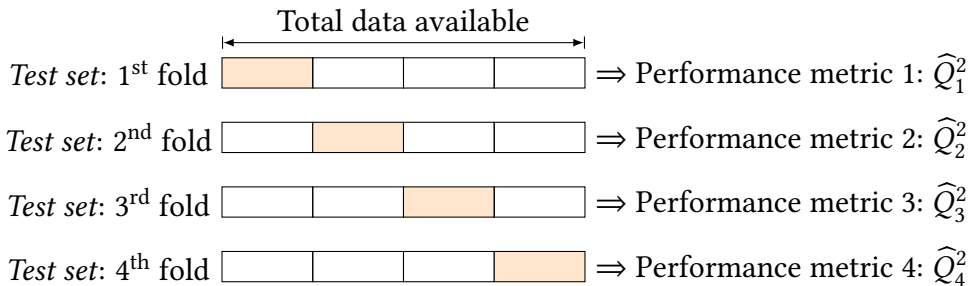


Figure 1.12 Illustration of a k -fold cross-validation (with $k = 4$)

1.7.2 General purposes surrogate model

In this section, a particular focus is dedicated to Gaussian process (GP) regression (also called kriging after the geostatistician D.G. Krige). Gaussian processes are a widely used regression method in UQ for their performance, flexibility and their associated confidence model. In a small-data context, the way of placing the few points forming the surrogate’s learning set is critical. Intuitively, to build a versatile surrogate model, the learning set should collect information over the entire domain uniformly. Which is why space-filling designs of experiments are commonly used to build learning sets. In practice, QMC and optimized LHS design introduced in Section 1.4 are widely used.

Gaussian process regression

Considering a learning set \mathbf{X}_n , the goal is to approximate the function $g(\cdot)$ by a scalar Gaussian process conditioned on a set of observations $\mathbf{y}_n = \left\{ g\left(\mathbf{x}^{(i)}\right) \right\}_{i=1}^n$. Let us first define a prior structure ξ on the function approximated $g(\cdot)$, taken as a Gaussian process with a mean function $m(\cdot)$ and covariance function $k(\cdot, \cdot)$:

$$\xi \sim \mathcal{GP}(m(\cdot), k(\cdot, \cdot)), \quad (1.89)$$

with a:

- *trend model*: $m(\mathbf{x}) = \mathbf{f}(\mathbf{x})^\top \boldsymbol{\beta}$, composed of a functional basis $\mathbf{f} = (f_1, \dots, f_d)^\top$ and a vector of coefficients $\boldsymbol{\beta} = (\beta_1, \dots, \beta_d)^\top$,
- *covariance model*: $k(\mathbf{x}, \mathbf{x}')$, usually taken stationary, such that $k(\mathbf{x}, \mathbf{x}') = \sigma^2 k_s(\mathbf{x} - \mathbf{x}', \boldsymbol{\theta})$ with $\sigma^2 > 0$ and $\boldsymbol{\theta} \in \mathcal{D}_X$.

The trend model of a GP defines its general tendency, while the covariance model influences its regularity. Gaussian process regression takes different names depending on the knowledge of the trend model. It is called “simple kriging” when the trend is fully known, “ordinary kriging”, when the trend is unknown but supposed constant and “universal kriging” otherwise. Note that [Schobi et al. \(2015\)](#) introduced a hybrid method named PC-Kriging setting a PCE as the trend of a kriging model.

To ease the presentation, let us first consider the hyperparameters $\sigma, \boldsymbol{\theta}$ fully known and a zero trend $\boldsymbol{\beta} = \mathbf{0}$. At a given point $\mathbf{x} \in \mathcal{D}_b X$ the realization of the GP is a Gaussian random variable $\xi(\mathbf{x}) \sim \mathcal{N}(m(\mathbf{x}), k(\mathbf{x}, \mathbf{x}))$. Working with Gaussian variables allows to easily write conditioning formulas between $\xi(\mathbf{x})$ and the observations \mathbf{y}_n . This Gaussian variable $\xi(\mathbf{x})$ conditioned on the observations \mathbf{y}_n is sometimes called conditional posterior $\xi_n(\mathbf{x}) := (\xi(\mathbf{x}) | \mathbf{y}_n) \sim \mathcal{N}(\eta_n(\mathbf{x}), s_n^2(\mathbf{x}))$. The well-known “Kriging equations” (see e.g., [Rasmussen and Williams 2006](#)) offer its explicit expression:

$$\begin{cases} \eta_n(\mathbf{x}) &:= \mathbf{k}^\top(\mathbf{x}) \mathbf{K}^{-1} \mathbf{y}_n \\ s_n^2(\mathbf{x}) &:= k(\mathbf{x}, \mathbf{x}) - \mathbf{k}^\top(\mathbf{x}) \mathbf{K}^{-1} \mathbf{k}(\mathbf{x}) \end{cases} \quad (1.90)$$

where $\mathbf{k}(\mathbf{x})$ is the column vector of the covariance kernel evaluations $[k(\mathbf{x}, \mathbf{x}^{(1)}), \dots, k(\mathbf{x}, \mathbf{x}^{(n)})]$ and \mathbf{K} is the $(n \times n)$ variance-covariance matrix such that the (i, j) -element is $\{\mathbf{K}\}_{i,j} = k(\mathbf{x}^{(i)}, \mathbf{x}^{(j)})$.

In practice the surrogate model is defined by the *predictor* function $\eta_n(\cdot)$. This regression model provides an important complementary information with the *kriging variance* $s_n^2(\mathbf{x})$, reaching zero at the learning points. Let us remark that the kriging variance fully depends on the covariance model (defined by its parametric structure and hyperparameters). In practice, the hyperparameters are unknown, therefore, their estimation is a key step in the construction of a kriging model. This estimation can be done using different approaches, most commonly using maximum likelihood estimation or a cross-validation.

The illustration in Fig. 1.13 is a typical one-dimensional representation of an ordinary kriging model. The mean of the conditioned process is plotted in red while its variability is represented by the many trajectories drawn on the process. In the simplest framework, the kriging model exactly interpolate the observations (black crosses).

Associated with kriging models, another validation criterion is relevant to evaluate the kriging variance $s_n^2(\mathbf{x})$. The predictive variance adequation (PVA) has been introduced by [Bachoc \(2013\)](#) to confirm that the kriging variance is reliable. For a validation performed by holdout,

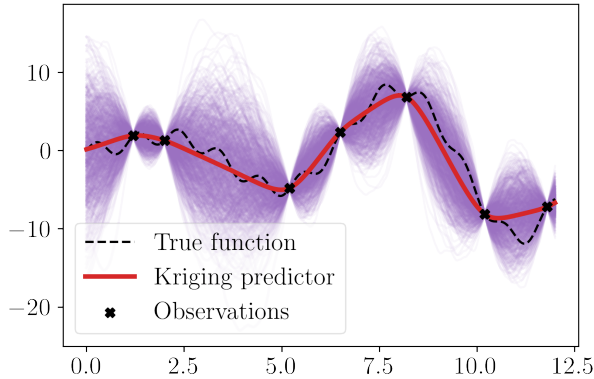


Figure 1.13 Illustration of an ordinary kriging model fitted on a limited set of observations ($n = 7$). The predictor is represented in and several trajectories of the conditioned Gaussian process are drawn represented in purple.

and using an independent m -sized test set, the PVA is defined as:

$$\text{PVA} = \left| \log \left(\frac{1}{m} \sum_{i=1}^n \frac{(y(\mathbf{x}^{(i)}) - \hat{g}(\mathbf{x}^{(i)}))^2}{s_n^2(\mathbf{x}^{(i)})} \right) \right|. \quad (1.91)$$

The smaller this quantity get, the better the quality of the kriging variance.

Gaussian process regression is an elegant solution, offering a lot of flexibility and an associated error model (i.e., the kriging variance). However, well known numerical issues appear during the estimation of the hyperparameters, especially as the learning size increases. More specifically, the computation and memory allocation for the variance-covariance matrix is a recurrent issue. Multiple techniques solve this issue by applying compression schemes on this matrix, e.g., based on sparse approximations (e.g., Hierarchical Matrices Geoga et al. 2020).

This section introduced a general purpose surrogate model, uniformly approximating a function on a domain, however surrogates are often used for specific purposes (e.g., contour finding for reliability analysis).

OpenTURNS 6 (Gaussian process regression). The Python code available in Appendix ?? proposes a minimalistic OpenTURNS example to fit an ordinary kriging model and active learning models. Figures illustrating the present section may be reproduced, using the OpenTURNS scripts available on GitHub^{13,14}.

1.7.3 Goal-oriented active surrogate model

Surrogates are often fitted for a specific purpose, requiring an accurate approximation over a limited subdomain only. In these cases, a more efficient approach might be to circumscribe

¹³https://github.com/efekhari27/thesis/blob/main/numerical_experiments/chapter1/surrogates.ipynb

¹⁴https://github.com/efekhari27/thesis/blob/main/numerical_experiments/chapter1/active_learning.ipynb

the learning to this subdomain (i.e., *goal-oriented learning*), rather than uniformly over the entire domain. For example, to fit a surrogate model for contour finding in reliability analysis, one should concentrate the learning set around the limit-state function. Similarly, to build a surrogate for a global optimization problem, one should focus the learning set around the optimum(s). Unfortunately, the area(s) of interest is usually unknown before evaluating the true function. *Active learning* is a general concept, aiming at iteratively increasing the learning set w.r.t. a *learning criterion* (also called “acquisition function”) depending on the surrogate’s goal to enhance the surrogate in the area(s) of interest. An exploration–exploitation trade-off arises in active learning, mostly sorted by the learning criterion.

Remark 1. This section introduces active learning methods in the computer experiment context, where the true function can be evaluated anywhere for a given computational cost. However, the “active learning” term is also used to handle big data frameworks in the machine learning community (Qiu et al., 2016). When datasets become so large that learning methods do not scale in practice, the analyst needs to select a relevant subset on which the learning is performed.

Active kriging for optimization

In the field of black-box optimization, many methods rely on approximating the function by a surrogate. The use of Gaussian processes as probabilistic surrogates for optimization was popularized by the *efficient global optimization* (EGO) algorithm (Jones et al., 1998). Ever since, many related methods were developed under the generic name of *Bayesian optimization*. The main idea is to exploit the uncertainty model from the GP to direct the point selection. Factually, the learning criterion depends on the Gaussian process variance model. Numerous reviews of this field were proposed by Shahriari et al. (2015); Gramacy (2020) and numerical benchmarks presented in Le Riche and Picheny (2021).

The generic black-box optimization problem tackled is defined as:

$$\mathbf{x}^* = \arg \min_{\mathbf{x} \in \mathcal{D}_X} g(\mathbf{x}) \approx \arg \min_{\mathbf{x} \in \mathcal{D}_X} \hat{g}(\mathbf{x}). \quad (1.92)$$

To illustrate Bayesian optimization, let us present the EGO algorithm, defined by its specific learning criterion: the “expected improvement”. Considering an initial learning set $\{\mathbf{X}_n, \mathbf{y}_n\}$ built on a space-filling input design \mathbf{X}_n to explore the domain. A first surrogate $\xi_n(\mathbf{x}) \sim \mathcal{N}(\eta_n(\mathbf{x}), s_n^2(\mathbf{x}))$ is fitted using Eq. (1.90). The expected improvement, to be maximized, is then written as:

$$\mathcal{A}^{EI}(\mathbf{x}; \mathbf{y}_n) = \mathbb{E}[\max(g_{\min} - \xi_n(\mathbf{x}))] \quad (1.93)$$

$$= (g_{\min} - \eta_n(\mathbf{x})) \Phi\left(\frac{g_{\min} - \eta_n(\mathbf{x})}{s_n(\mathbf{x})}\right) + s_n(\mathbf{x}) \phi\left(\frac{g_{\min} - \eta_n(\mathbf{x})}{s_n(\mathbf{x})}\right), \quad (1.94)$$

where $g_{\min} = \min(\mathbf{y}_n)$, ϕ and Φ respectively stand for the PDF and the CDF of the standard Gaussian distribution. This learning criterion is relatively inexpensive and allows to progressively enhance the Gaussian process to solve the optimization problem with a limited number of calls to the true function.

Three iterations of the EGO algorithm are represented in Fig. 1.14 to minimize a function (dashed line), knowing a few observations (black crosses). After fitting an initial kriging model (in red), the corresponding expected improvement function is represented underneath it (green line). This learning criterion determines the location of the observation to be added to the learning set to enhance the surrogate w.r.t. to the optimization problem.

Bayesian optimization is an active research field, with different open problems such as constrained Bayesian optimization (Petit, 2022), or Bayesian optimization on stochastic functions (Gramacy, 2020). Similarly, active learning was also adapted for structural reliability problems.

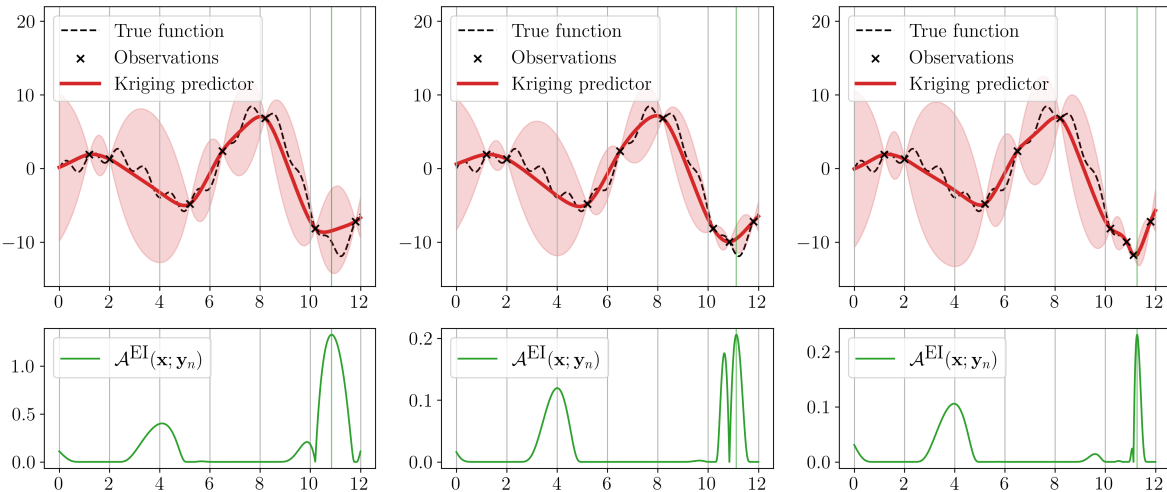


Figure 1.14 Illustration of the expected improvement learning criterion

Active kriging for reliability analysis

Rare event estimation often requires large amounts of evaluations of the limit-state function (becoming intractable for costly numerical models). Emulating this function by a surrogate model can drastically limit the number of calls to the LSF. This surrogate approximates the contour (i.e., border) of the failure domain. However, in most cases, the failure domain represents a very restricted area of the input domain. Active learning methods were proposed to iteratively concentrate the learning set around this border.

For rare event estimation, the surrogate only needs to be accurate near the limit state function. In other words, it should accurately discriminate the points leading to the safe domain from those leading to the failure domain. In fact, this problem can be seen as a binary classification. For example, active learning procedure using SVM classifiers were adapted to this specific goal (Bourinet, 2018).

The following paragraph introduces the most popular kriging-based learning criterion: the “deviation number” U (Echard et al., 2011). The reader may refer to Morio and Balesdent (2015) for further active learning techniques dedicated to rare event estimation. More recently, Teixeira et al. (2021) and Moustapha et al. (2022) reviewed this topic with the presentation of wide numerical benchmarks.

Considering an initial learning set $\{\mathbf{X}_n, \mathbf{y}_n\}$ built on a space-filling input design \mathbf{X}_n to explore the domain. A first Gaussian process $\xi_n(\mathbf{x}) \sim \mathcal{N}(\eta_n(\mathbf{x}), s_n^2(\mathbf{x}))$ is fitted using Eq. (1.90). The deviation number U is looking for points close to the limit-state function while presenting a high kriging variance. This criterion to be minimized, is defined as:

$$\mathcal{A}^U(\mathbf{x}; \mathbf{y}_n) = \frac{|y_{\text{th}} - \eta_n(\mathbf{x})|}{s_n^2(\mathbf{x})}, \quad (1.95)$$

where $y_{\text{th}} \in R$ is a threshold defining the failure domain.

Fig. 1.15 reuses the same one-dimensional function as in Fig. 1.14 to create a rare event problem. In this case, the failure domain is defined for output values below the threshold y_{th} . Once again, three iterations of the AK algorithm are illustrated, with the corresponding learning criterion U (to minimize). In this simple case, the LSF is defined by the two intersections of the function with the threshold. Therefore, the AK method selects points near these intersections.

Unlike optimization problems, the surrogate is used for uncertainty propagation, meaning that the rare event estimation is the result of the approximation of the LSF (i.e., contour finding) and a sampling techniques. AK methods were coupled with most sampling techniques introduced in Section 1.5 (e.g., AK-MCS, AK-IS, AK-SS, etc.). As an agnostic strategy, [Moustapha et al. \(2022\)](#) recommend to start by applying an AK method (using the learning function U) paired with a subset sampling (taking an intermediary probability $p_0 = 0.2$).

The AK methods present the advantages to be easily implemented and interpreted, however, their learning criterion rely on a local approach. Alternatively, the *stepwise uncertainty reduction* (SUR) chooses iterative points by reducing the future expected uncertainty related to the quantity of interest ([Bect et al., 2012](#)). If this method was proven to be theoretically more consistent ([Bect et al., 2019](#)), its scaling ability is still a bottleneck.

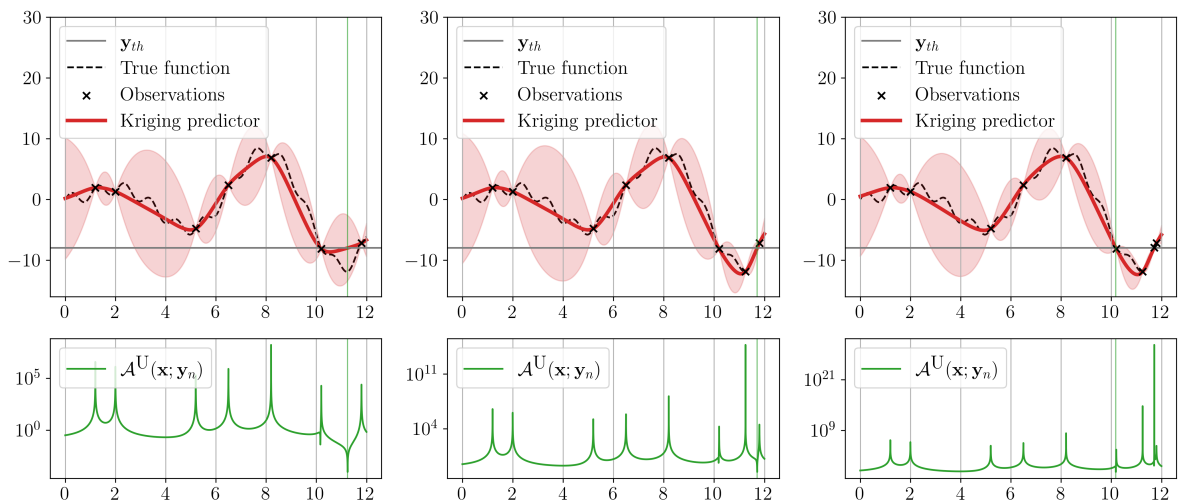


Figure 1.15 Illustration of the deviation number learning criterion

1.7.4 Summary and discussion

This section brought the attention on surrogate modeling in the context of computer experiments. Statistical learning in this framework is made specific by the capacity of the analyst to choose the repartition of the learning set and the small data constraint (mostly due to the costly numerical models manipulated). In this context, many methods are used, however Gaussian processes became popular in UQ as they consider a prior structure of uncertainty that is conditioned by observations (at the edge between a Bayesian and a frequentist approach). To enhance the learning for specific purposes (e.g., optimization or contour finding), active learning methods iteratively add learning points in the subdomain of interest. For some applications, the system studied might be modeled for different fidelities (each presenting different computational costs). Multi-fidelity surrogate modeling is an active field of research, associating observations from different fidelities to improve the learning (Fernández-Godino et al., 2016). Such methods are relevant for models with a very high computational cost (typically in computer fluid dynamics).

In UQ, surrogate models are used for uncertainty propagation (step C) and inverse analysis (step C'). Surrogate modeling is made difficult when the functions present discontinuities (or strong nonlinearities), high dimension, stochasticity, or nonscalar inputs or outputs. To deal with high dimensional problems, unimportant inputs can be screened using sensitivity analysis (see Section 1.6.1), otherwise, model order reduction methods might be used [ref ?]. When the function is stochastic, different approaches allow to fit the function and its intrinsic variability (Binois et al., 2019; Baker et al., 2020; X., 2022).

Provided a strict validation process, surrogate models are a great opportunity for uncertainty quantification. However, many regulatory authorities are still reluctant to the use of surrogates, although their error is often much smaller than the modeling error (i.e., the error between the actual physical behavior and its numerical modeling).

1.8 Conclusion

This section gives a literature overview of the main steps in uncertainty quantification. From uncertainty modeling, uncertainty propagation, sensitivity analysis to surrogate modeling. To ease the methodological presentation, all the illustrations from this section are reproducible using the Python/OpenTURNS scripts available on the GitHub repository mentioned earlier.

Finally this work, the numerical models exploited are supposed to be accurate, but they obviously carry some modeling uncertainty (Oberkampf and Roy, 2010). In fact, prior to uncertainty quantification the model should be calibrated to make it match some physical information (e.g., measurements). Numerical model calibration is also called data assimilation when a stream of measured data is available.

The aim of this work is to apply the tools presented in this chapter to offshore wind turbine models, therefore the next chapter introduces the numerical models manipulated in this thesis.

Chapter **2**

Introduction to wind turbine modeling and design

2.1	Introduction	62
2.2	Metocean conditions simulation	62
2.2.1	Turbulent wind generation	63
2.2.2	Wake modeling	66
2.2.3	Irregular wave generation	67
2.3	Wind turbine multi-physics modeling	68
2.3.1	Aerodynamics of horizontal axis wind turbines	69
2.3.2	Hydrodynamics	71
2.3.3	Control	72
2.3.4	Structural dynamics	72
2.3.5	Fatigue damage	73
2.4	Design and operation practices	76
2.4.1	Types of technologies and preliminary design	77
2.4.2	Further design considerations	78
2.5	Uncertain inputs	81
2.5.1	Environmental inputs	82
2.5.2	System inputs	82
2.5.3	Probabilistic fatigue assessment	83
2.6	Conclusion	85

2.1 Introduction

Wind energy is a highly competitive industry with increasing regulations regarding its impact on ecosystems, land and sea-use, landscapes, or air traffic management (Beauregard et al., 2022). During the long process to win calls for tenders, obtain construction permits, or through the wind farm exploitation, an advanced technical understanding of such systems might offer a competitive advantage.

The operation of offshore wind turbines (OWTs) is driven by multiple physics coupled. This behavior results from different external solicitations which are highly turbulent and uncertain. Among them, the *metocean* (abbreviation of “meteorology” and “oceanography”) environmental conditions play a primary role. Yet, many other types of solicitations affect the exploitation of offshore wind turbines e.g.: the corrosion of the structure, global scour, marine growth, stress concentration factor induced by the manufacturing quality, etc.

In this context, numerical models have been developed to certify the structural integrity of OWTs with respect to their solicitations. A wind farm project planned at given location should pass different validation procedures established by international standards such as the International Electrotechnical Commission ([IEC-61400-1, 2019](#)). As wind turbine structures face a large amount of stress cycles in their lifetime (up to 10^8 for 20 years of operation), this chapter will particularly focus on fatigue damage assessment.

The present thesis studied different steps of uncertainty quantification on two wind farm projects. First the Teesside wind farm, operating since 2014 in the North Sea, second the theoretical wind farm of south Brittany, currently at the stage of calls for tenders.

Considering the standard uncertainty quantification diagram presented in Fig. 1, the material of this chapter is related to the step A (problem specification) and the step B (uncertainty quantification). It briefly introduces wind turbine modeling and design, in the following layout: Section 2.2 presents the methods used for wind and wave generation and wake simulation at a farm scale; Section 2.3 recalls elements of theory associated with wind turbine modeling; Section 2.4 introduces recommended practices regarding design and operation; finally, Section 2.5 gives a description of the various sources of uncertainties considered in this thesis.

2.2 Metocean conditions simulation

In the atmosphere, the wind represents the air movements caused by the heterogeneous solar heating of Earth’s surface. Winds usually move from high-pressure to low-pressure regions. Earth’s rotation also impacts large-scale climate patterns, including winds by the intermediate of the well-known Coriolis effect. The wind is a highly variable resource, making its exploitation for energy production uncertain. This variability is both expressed in space and time with different behaviors depending on the scales studied.

Regarding large timescales, yearly seasonal fluctuations of wind conditions are well-defined using probability distributions (typically Weibull distributions). However, predictions at a

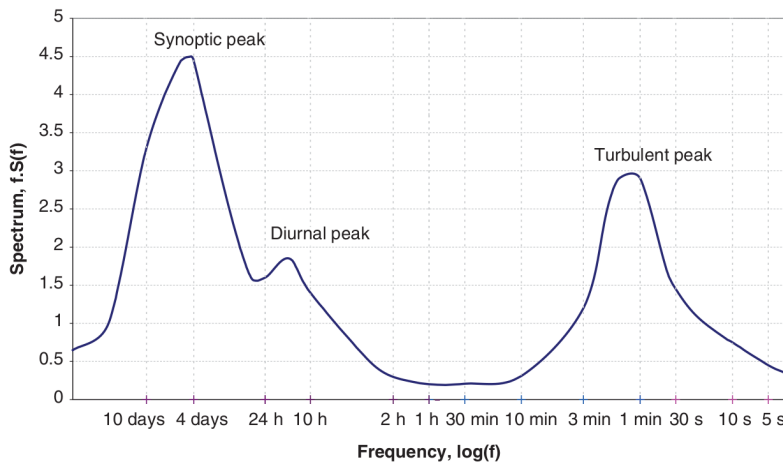


Figure 2.1 Wind spectrum from Brookhaven, USA (source: Burton et al. 2021)

shorter timescale are usually unreliable beyond a few days ahead. Under a few days, the spectral wind energy distribution per time unit is represented by its power spectral density (PSD). Historically, the spectral study of horizontal wind by [Van der Hoven \(1957\)](#) for timescales between a few seconds and ten days revealed distinct ranges of behaviors. The PSD, such as the one illustrated in Fig. 2.1, presents three main separated peaks, explaining how the wind energy is split. The two first peaks are named “synoptic” and “diurnal” peak, which respectively correspond to return periods around four days and one day. While these two peaks are relatively close together, the third peak is completely separated. This third peak describes the energy related to wind turbulence, which evolves in a range below ten minutes. Considering this typical energy distribution, wind behaviors are often referred to as “short-term” (for turbulent wind) and “long-term” (otherwise). In wind turbine simulation, ten minutes simulations became a common practice to fully consider turbulent winds.

Remark that the spectrum presented in the research paper of [Van der Hoven \(1957\)](#) (represented in Fig. 2.1) was build from wind measures near New York, USA. The same pattern between the three peaks is rather constant between sites, however, the geography (including the surface roughness, the topology, the proximity to the coast, etc.) may affect this distribution.

At a larger timescale than one year, assessing trends becomes more complicated. Additionally, wind resource assessment over decades is made more uncertain by climate change [Nagababu et al. \(2023\)](#), disrupting large weather trends and increasing the occurrence of extreme events.

2.2.1 Turbulent wind generation

Wind turbulence is a complex and aleatory process, often described as chaotic, since a small perturbation of its initial conditions might have an important impact on the response. However, the wind over short-term periods (i.e., ten minutes periods) is usually assumed to be a Gaussian process with constant mean \bar{U} and standard deviation σ_U ([Burton et al., 2021](#)). Its mean is modeled by the long-term wind conditions (i.e., mean wind speed), often described by a probabilistic model such as a Weibull distribution. [This short-term / long-term modeling

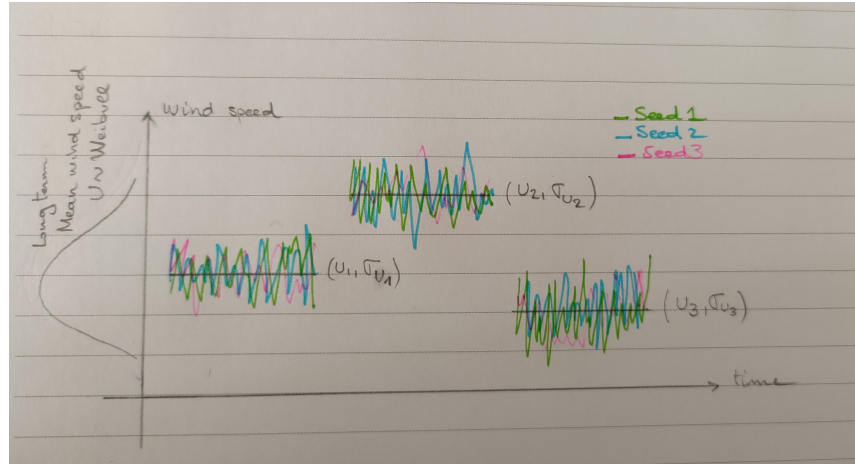


Figure 2.2 [Should we keep this representation? If so, it will be done properly.]

hypothesis is represented in Fig. ??.] Note that this assumption is based on the bimodal wind energy distribution observed in Fig. 2.1, which might vary at some specific locations.

The *turbulence intensity* is a commonly used normalized statistic of the wind variability:

$$I = \frac{\sigma_U}{\bar{U}}. \quad (2.1)$$

As the wind depends on differences between pressure, humidity, air density, different models exist to represent vertical wind profiles. The vertical change in wind conditions is referred to as *vertical wind shear*. Assuming a constant standard deviation over the altitude, the power law is a widely used model to approximate vertical shear ([IEC-61400-1, 2019](#)):

$$\bar{U}(z) = \bar{U}_0 \left(\frac{z}{z_0} \right)^\alpha, \quad (2.2)$$

with \bar{U}_0 a well-defined mean wind speed at the height z_0 (typically corresponding to a measurement height), z the studied height (e.g., the turbine's hub-height), and α the vertical shear coefficient (defined according to measures or standards' recommendations).

To generate a turbulent wind field on a mesh around the turbine, the general mechanism is to apply inverse Fourier transforms on a turbulent wind spectrum. Two types of parametric spectrums are commonly used in wind energy: the *Kaimal model* ([Kaimal et al., 1972](#)) and the *Mann model* ([Mann, 1998](#)). In this thesis, the Kaimal spectrum as defined in [IEC-61400-1 \(2019\)](#) is used for turbulent wind generation over the Cartesian component $k \in \{u, v, w\}$:

$$S_k(f) = \frac{4\sigma_k^2 \frac{L_k}{\bar{U}}}{\left(1 + 6f \frac{L_k}{\bar{U}}\right)^{5/3}}, \quad (2.3)$$

such that f is the frequency, \bar{U} is the longitudinal mean speed at hub-height, L_k are the Kaimal length scales, and σ_k standard deviations. Along with the Kaimal wind speed spectrum, a spacial

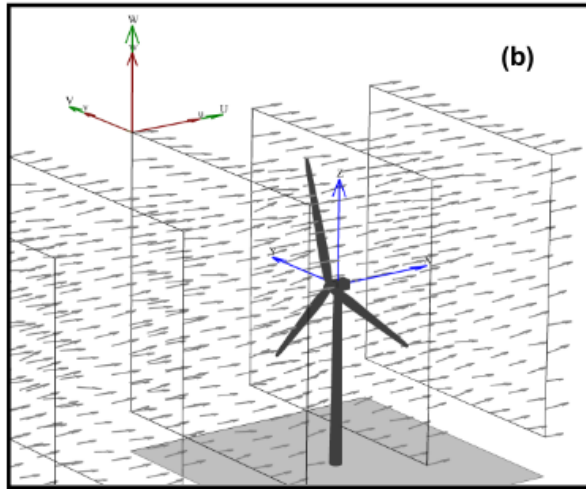


Figure 2.3 Example of a turbulent wind field generated by TurbSim (source: [Jonkman 2009](#))

coherence model is usually defined in the frequency domain. Each couples of nodes in the mesh are correlated, for example, using an exponential coherence model (see the complete definition in Annex C of [IEC-61400-1 2019](#)).

In this thesis, the full-field turbulent wind fields (i.e., over a regular mesh) are generated using TurbSim, a software developed by the National Renewable Energy Laboratory (NREL) ([Jonkman, 2009](#)). TurbSim generates time realizations by adapting the spectral method proposed in [Veers \(1988\)](#) (relying on the inverse Fourier transforms of each axial component). Considering a wind spectrum (e.g., Kaimal model) and a vertical shear model (e.g., power law), TurbSim takes as inputs a mean wind speed, a turbulence standard deviation and a mean wind orientation. Fig. 2.3 illustrates the corresponding wind field generated by a ten-minutes TurbSim simulation, considering a set of input long-term conditions.

In their recent review of the challenges in wind energy, ([Veers et al., 2019](#)) list some limits of the two spectral turbulence models recommended by the standards. First, their parameters were fitted using a restricted amount of data ([Dimitrov et al., 2017](#)). Second, the spacial coherence models associated with Kaimal models showed differences with turbulence measured on site ([Saranyasoontorn et al., 2004](#)). Finally, recent studies showed that the choice of spectral model impacts the resulting wind turbines loads ([Doubrawa et al., 2019](#)). These approximations generally tend to overestimate wind flows, leading to conservative designs.

To ensure more realistic turbulent wind field generation, two research perspectives are actively explored. Authors recently developed hybrid methods, including measurement data to enhance spectral models ([Dimitrov and Natarajan, 2017](#)). Alternatively, higher fidelity models were studied in this domain, see for example the use of vortex methods ([Branlard, 2017](#)) and large eddy simulations (LES) ([Doubrawa et al., 2019; Bui and Bakhoday-Paskyabi, 2022](#)). Such complex models allow the simulation of mesoscale conditions (e.g., at the farm scale), and extreme transient events (e.g., gusts and storms). However, their computational cost is often prohibitive for uncertainty quantification studies. When studying the wind resources at a wind farm scale, modeling wind energy losses induced by the turbines' wake becomes essential.

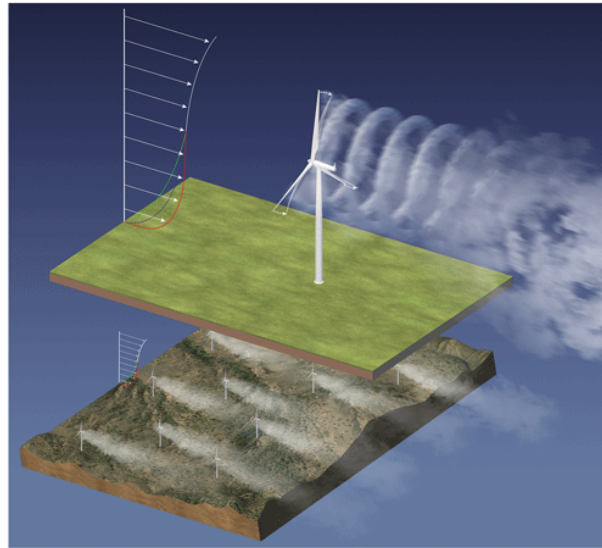


Figure 2.4 Illustration of the wake created downstream a wind farm (source: [Veers et al. 2019](#))

2.2.2 Wake modeling

The wake is caused by the extraction of the wind kinetic energy, reducing the wind speed and increasing the turbulence downstream of the turbines (see the illustration in Fig. 2.4). In a wind farm, this effect depends on the spacing between turbines, as well as the ambient wind speed and turbulence intensity. The turbines positioned at the center of the farm are indeed the most impacted by the wake. As a wind farm owner, the consequence of the wake is twofold: a loss of energy production (in the range of 10 to 20 percents depending on the farm), and an increase of fatigue loads (due to the asymmetric loading from the created turbulences).

The initiation of the wake is a complex physical mechanism, however, the wake almost becomes axisymmetric after two turbine diameters downstream. At this stage, the wind speed deficit often presents a Gaussian profile centered on the hub ([Burton et al., 2021](#)). Numerical models of different fidelities aim at simulating the wake. For example, computational fluid dynamics (CFD) models give a detailed description of the wake (including near the turbine) but require high computational efforts. In practice, simple analytical models (often called “engineering models”) are widely used and recommended by standards (see e.g., Annex E in [IEC-61400-1 2019](#)). These models mostly rely on the equivalence between the thrust load and the turbine wind energy deficit. Since the seminal engineering model proposed by [Jensen \(1983\)](#), multiple enhancements were proposed. A wide benchmark of the wake modeling solutions for different fidelities was performed in [Doubrava et al. \(2020\)](#) and [Ardillon et al. \(2023\)](#). The optimal tuning of these engineering models was studied using measurements from a Doppler wind lidar in [Zhan et al. \(2020\)](#). Different software programs propose wake engineering models, such as: FLORIS (developed by the NREL [Fleming et al. \(2020\)](#)), FarmShadow (developed by IFPEN).

To take into account the wake effect, control strategies increasingly move from the turbine scale to the farm scale. This concept, called “active wake control”, introduces small yaw

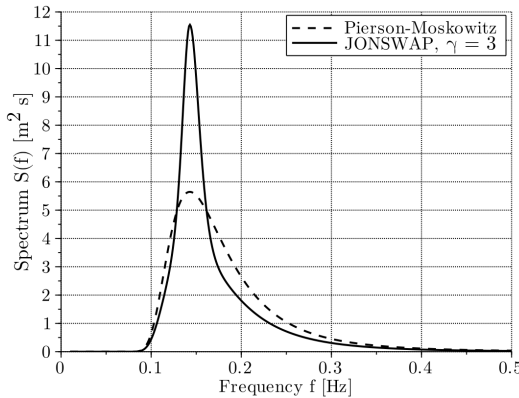


Figure 2.5 Peirson-Moskowitz and JONSWAP spectra at significant wave height $H_s = 3$ m and peak period $T_p = 7$ s (source: [Milano 2021](#))

misalignments (making the control of turbines individually suboptimal) to optimize the global wake inside the farm ([Rott et al., 2018](#); [Simley et al., 2020](#); [Meyers et al., 2022](#)).

2.2.3 Irregular wave generation

The propagation of wind generated waves has long been studied in hydrodynamics under the prism of different theories such as Airy's, and Stokes'. Airy's wave theory (also referred to as the linear wave theory) models sea states under the hypothesis of small waves relatively to the water depth. This spectral approach superposes many regular waves, following the same wave spectrum, to model irregular waves. Two standard statistics are used in oceanography to represent sea states and their corresponding wave spectra: the wave period T_p (with the corresponding frequency f_p), and the significant wave height H_s (average over the highest third of the waves measured).

The most commonly used parametric wave spectrum is named JONSWAP, after the “Joint North Sea Wave Project” ([Hasselmann et al., 1973](#)):

$$S(f) = \delta \frac{H_s^2}{f} \left(\frac{f_p}{f} \right)^4 \exp \left[-\frac{5}{4} \left(\frac{f_p}{f} \right)^4 \right] \gamma^\alpha. \quad (2.4)$$

The JONSWAP spectrum is a corrected version of the Pierson-Moskowitz spectrum (developed in 1964), adding a peak enhancement factor γ^α . Further details regarding the numerical values to choose in Eq. (2.4) are given in [Burton et al. \(2021\)](#). An illustration of the two spectra is presented in Fig. 2.5, revealing the enhancement factor proposed in the JONSWAP model to better fit sea states measurements.

Swell waves are the result of weather conditions occurring far away from the location studied. Such waves usually present long wavelength, allowing them to propagate over long distances with little dissipation. To take them into account, the unimodal wave spectra introduced in Eq. (2.4) was improved. Different methods allow to build a parametric bimodal distribution,

with a mode in the low frequencies corresponding to the swell. [Ewans et al. \(2004\)](#) reviews different bimodal wave spectra, and compares their adequacy with measured sea states.

2.3 Wind turbine multi-physics modeling

Offshore wind turbine models are coupling multiple physics such as aerodynamics, hydrodynamics, mechanical elasticity, control and mooring dynamics for floating OWT. Similarly to the usual practices from the offshore oil & gas industry, OWT have been first modeled in the frequency domain. At an early design stage, a study in the frequency domain gives a rough idea of the system's feasibility by computing its natural frequencies. An OWT should not have its natural frequencies in the same range as the main frequencies of the wave energy spectra. Otherwise, such systems can be subject to critical dynamic resonance, leading to their failure.

Beyond this preliminary check, frequency-domain approaches present limits for OWT modeling. As they rely on linear assumptions, they are unable to model the nonlinearities and transient loading phases ([Matha et al., 2011](#)). These aspects happen to be essential in the design of OWTs ([Cordle and Jonkman, 2011](#)). As an alternative, the behavior of OWT systems are also simulated in the time domain.

In the time domain, such systems may be models for different fidelities. The diagram in Fig. 2.7 illustrates the increasing complexities for two physics involved in OWT modeling (aerodynamics and structural dynamics). Generally, the computational cost increases with the model fidelity, making uncertainty quantification intractable at some point. In the present work, the numerical model of an OWT studied is actually a chain of three models executed sequentially (as illustrated in Fig. 2.6):

- **TurbSim:** a turbulent wind generator (see Section 2.2.1);
- **DIEGO:** a multiphysics wind turbine model in the time domain (see Section 2.3);
- **Fatigue assessment:** a post-processing computing fatigue damage (see Section 2.3.5).

DIEGO is a numerical model developed by EDF R&D to simulate the aero-hydro-servo-elastic behavior of OWTs in the time domain. Different extensive code-to-code comparisons between DIEGO and other aero-hydro-servo-elastic models showed close results. Considering bottom-fixed OWT ([Popko et al., 2021](#)) or floating OWT ([Robertson et al., 2020; Kim et al., 2022](#)), DIEGO was compared to “FAST” (developed by NREL), “HAWC2” (developed by DTU), “BLADED” (developed by DNV), and “DeepLines Wind” (developed by IFPEN).

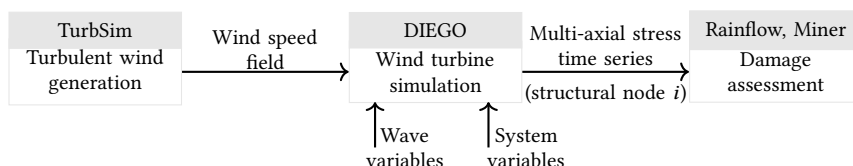


Figure 2.6 Chained numerical model of offshore wind turbine.

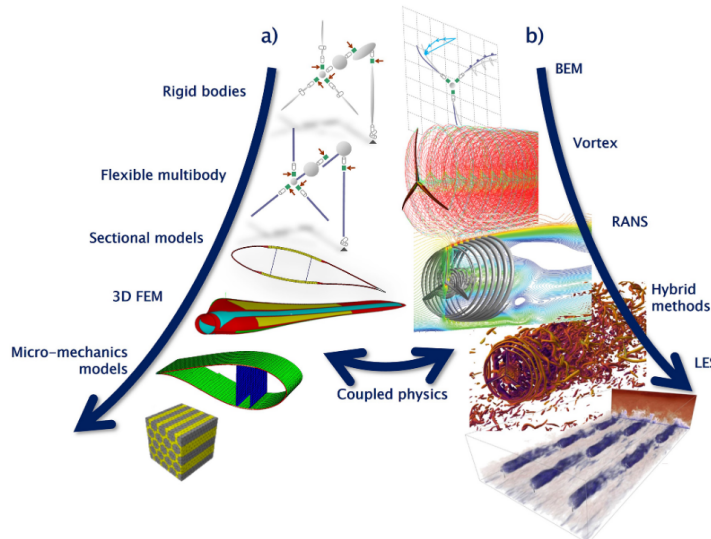


Figure 2.7 Hierarchy of structural (a) and aerodynamic (b) wind energy systems models (source: Veers et al. 2019)

2.3.1 Aerodynamics of horizontal axis wind turbines

The blade element momentum theory mixes different concepts to compute the aerodynamic forces on the rotating blades of the wind turbine. In this coupled physics models, the aerodynamics affects the structural response and vice-versa. To solve this problem, algorithms used in DIEGO first assess displacement of elementary blades, to recover the lift and drag coefficients. The elementary loads are then integrated over each blade and communicated to the structural model.

Momentum theory. At the core of wind turbine's aerodynamics, the concept of *momentum theory*, also called *actuator disk theory* assumes that the air stream passing thought the rotor disk is bounded by a stream tube of circular surface (not mixing with the ambient air). Fig. 2.8 is a longitudinal representation of the actuator disk and the way it affects the air upstream and downstream the rotor. The associated momentum theory assumes the conservation of airflow at any cross-section (of area A) during a time period. Passing through the actuator disk, the wind speed slows down and a drop in static pressure is at the origin of the wake. This pressure drop generates an axial force (called *axial thrust force*) and a torque on the actuator disk.

Considering the upstream flow, the flow at the rotor disk and the airflow in the wake, respectively denoted by the subscripts $\{\infty, d, \text{wake}\}$, the following equality comes:

$$\rho A_\infty U_\infty = \rho A_d U_d = \rho A_{\text{wake}} U_{\text{wake}}, \quad (2.5)$$

where U is the wind speed, A the stream-tube area, and ρ the air density. The wind speed in at the rotor disk can be expressed using the induction factor a in the following expression:

$$U_d = U_\infty(1 - a), \quad 0 \leq a \leq 1. \quad (2.6)$$

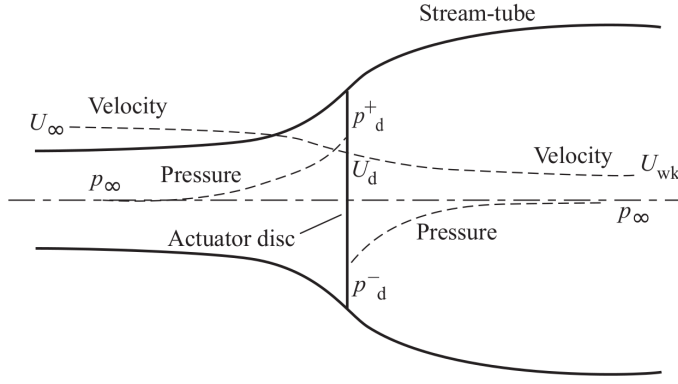


Figure 2.8 Actuator disk model of the energy extraction (source: Burton et al. 2021). Longitudinal evolution of the air pressure and wind speed along the wind stream.

Using the momentum theory and Bernoulli's incompressible flow equation, one can express the aerodynamic thrust T and power P (see Milano 2021):

$$T = (p_d^+ - p_d^-)A_d = 2\rho A_d U_\infty^2 a(1-a) \quad (2.7a)$$

$$P = TU_d = 2\rho A_d U_\infty^3 a(1-a)^2 \quad (2.7b)$$

The widely used power coefficient (respectively thrust coefficient) is the ratio of the power captured by the turbine against to the total kinetic wind power available in the stream tube:

$$C_P = \frac{P}{\frac{1}{2}\rho A_d U_\infty^3} = 4a(1-a)^2, \quad (2.8a)$$

$$C_T = \frac{T}{\frac{1}{2}\rho A_d U_\infty^2} = 4a(1-a). \quad (2.8b)$$

Betz's law is a theoretical limit value of the power coefficient, obtained by cancelling the power coefficient gradient. To this day, no wind turbine has exceeded this limit value: $C_P^{\text{Betz}} = 0.593$ (Burton et al., 2021).

Blade element theory. Assuming a purely two-dimensional flow (meaning that the forces are only determined by the lift and drag coefficients), the blade element theory expresses the thrust dT and torque dQ applied on a blade element.

Let us consider a wind turbine with B blades, a pitch length R and a pitch angle β . Assuming the blade element represented in Fig. 2.9 at the blade length r , with airfoil chord c , angle of attack α , lift C_L and drag C_D coefficients, lift L and drag D forces, and the axial and tangential induction factors a and a' . Under these assumptions, the axial thrust and torque exerted on a blade element are:

$$dT = \frac{1}{2}\rho W^2 B c (C_L \cos(\varphi) + C_D \cos(\varphi)) dr, \quad (2.9a)$$

$$dQ = \frac{1}{2}\rho W^2 B c (C_L \sin(\varphi) + C_D \sin(\varphi)) dr. \quad (2.9b)$$

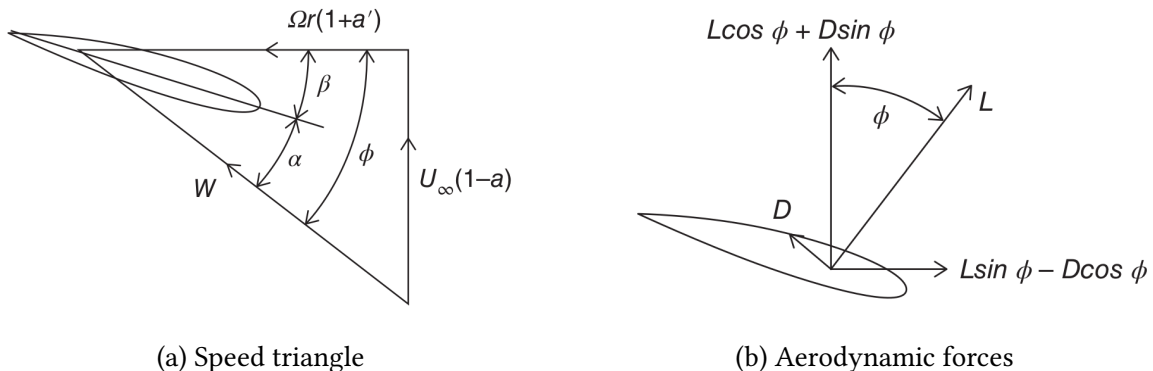


Figure 2.9 Blade element forces. With the lift and drag forces L and D , the flow angle ϕ , the pitch angle β and the angle of attack α (source: [Burton et al. 2021](#)).

Blade element momentum theory (BEMT) combines the results from blade element theory in Eq. (2.9) with the results from momentum theory in Eq. (2.7) to obtain the induction factors a and a' . The resolution of this system of equations is often solved by iterative approaches (e.g., Dai et al. 2011). Global axial thrust over the blade are then computed by integrating the elementary loads over all the elements. Note that various corrections are applied to the BEMT model, for example to take into account the non-homogeneous loss of momentum over the rotor disk. The BEMT also fails to model non-linear aerodynamic effects, occurring with sudden change of angle of attack. Such effects are sometimes called “dynamic stall” and are represented in DIEGO by the Beddoes-Leishman model (see Burton et al. 2021 for further details).

2.3.2 Hydrodynamics

Morison's equations are a widely-used semi-empirical model to assess the hydrodynamic forces on thin fixed structures such as offshore oil platforms and wind turbines. Considering a slender cylindrical structure of diameter D , a flow velocity $u(t)$, the drag and inertial coefficients C_m and C_D , the axial force (parallel to the flow direction) is given by:

$$F = C_m \rho \frac{\pi}{4} D^2 \frac{du}{dt} + C_d \frac{1}{2} \rho D u |u|. \quad (2.10)$$

Standard values for the drag and inertial coefficients are often considered (DNV-OS-J103, 2013). DIEGO uses Morison's equation together with first order potential solution to perform hydrodynamical simulations in the time domain. An extended introduction to hydrodynamics of fixed slender structures, as well as large floating structures is given in the Chapter 1 from (Milano, 2021).

To design floating structures, more complex wave loading modeling should be considered. For this purpose, Rongé et al. (2023) reviews nonlinear theories applied to the fluid-structure interactions of FOWT and compares them to CFD results.

2.3.3 Control

To maximize their energy production under turbulent wind conditions, wind turbines rely on their control systems. This aspect of wind turbines is usually kept confidential by manufacturers, as it gives them a competitive advantage. Nevertheless, the general control mode of a wind turbine depends on the wind speed. Two main ranges of operation are usually defined: first between the cut-in and rated wind speed, second between the rated and cut-off wind speed. These characteristic wind speed values are given by the turbine manufacturer, for example a turbine may present a cut-in at 4 m s^{-1} , a rated at 13 m s^{-1} and a cut-off at 25 m s^{-1} . Let us then recall the wind turbine power derived from the momentum theory:

$$P = \frac{1}{2} \rho A_d U_\infty^3 C_p(\lambda, \beta), \quad (2.11)$$

with the power coefficient C_p , function of the pitch angle β and the blade tip speed ratio λ , defined between the tangential speed on top of the blade and the wind speed: $\lambda = \frac{\Omega R}{U_\infty}$, for the rotation speed Ω and a rotor radius R .

Below the rated wind speed. The goal of the control system is to extract as much power as available. A control strategy among the family of the *maximum power point tracking* can be deployed (Abdullah et al., 2012). For example, the “power signal feedback” uses the electromagnetic torque to control the power. This method first computes the maxima of the extracted power as a function of the rotation speed (using Eq. (2.11)), for different speed values. Then, for a measured wind rotation speed, the system can determine the reference maximal power. Considering this reference power, a controller (such as a proportional integral controller) intends to match the generated power with the reference by acting on the electromagnetic torque.

Above the rated wind speed. The control system switches to a *power limiting* mode by increasing the blades’ pitch angles. By operating on the pitch, the rotation speed and the power produced are kept at their nominal values. This control is also often realized by a proportional integral system (Bossanyi, 2003).

A more exhaustive description of wind turbines control systems is available in Chapter 8 from Burton et al. (2021). More recent strategies often consider the control at the farm scale. As explained earlier, the operation of one turbine affects the others via the effect of its wake. Moreover, since the wind energy production becomes important in the electric mix, its production might be constrained to respect the stability of the grid (e.g., quality of the utility frequency). The work of Gionfra (2018) studied the optimal control of wind farms considering the effects of the wake and the grid restrictions.

2.3.4 Structural dynamics

The structural elements of modern wind turbines, such as the tower and the blades, compose a dynamic system subject to important elastic deformations. Modeling an operating wind

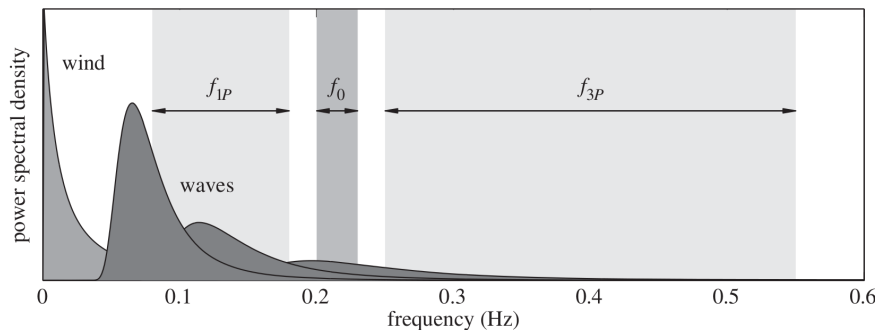


Figure 2.10 Illustration of a soft-stiff design strategy, placing the structure's natural frequency f_0 away from the wind and wave power spectra, and the rotor excitation frequencies f_{1P} and f_{3P} (source: Kallehave et al. 2015).

turbine therefore requires rigid body dynamics and nonlinear elastic deformations. All together, various approaches were developed to model the structural dynamics of wind turbines: modal analysis, multibody methods and finite element methods (FEM). At the stage of preliminary designs, modal approaches can be used to represent the dynamics under linear assumptions (Hegseth and Bachynski, 2019). Then, the tower's natural frequencies assessed by a modal analysis can be compared with the wind, waves, and the rotor's frequencies. As illustrated in Fig. 2.10, the structure's natural frequency (denoted by f_0) should not coincide with the main excitation frequencies to avoid critical dynamic resonance. In the case of a wind turbine, the rotor imbalance creates a first dynamic load of frequency f_{1P} , while the blades passing in front of the tower generate a second excitation of frequency f_{3P} . The *soft-stiff* design strategy places the structure's natural frequency between the two rotor frequencies (i.e., $f_{1P} < f_0 < f_{3P}$ as described in Fig. 2.10) and avoids main frequencies of the wind and waves.

However, modal analysis does not model transient loading phases and their corresponding non-linearities, which is crucial beyond early design. For a higher fidelity, simulations in the time domain using flexible multibody approaches are commonly used to describe the nonlinear dynamics (Holm-Jørgensen, 2009; Al-Solihat and Nahon, 2018). DIEGO implements such an approach by combining rigid multibody dynamics with a deflection model based on Lagrangian equations (Milano, 2021). Note that for floating wind turbines modeling, a preliminary step of rigid body dynamics is added to define the coordinate system of the floater. Otter et al. (2022) reviews the state-of-the-art of numerical and experimental modelling techniques for multi-physics OWT systems.

2.3.5 Fatigue damage

Mechanical fatigue damage is an important phenomenon to consider when designing wind turbines. It refers to the progressive weakening of a material when subjected to cyclic or repeated loading, which may be significantly lower than the material's ultimate strength. Understanding the mechanisms behind mechanical fatigue damage is essential for designing durable and reliable structures. To quantify the fatigue damage on offshore wind turbine structures, standards (DNV-

RP-C203, 2016) recommend simulating the stresses in the time domain and identifying a series of stress cycles. Then, the *stress-number of cycles curve* of a specific material (S-N curve) gives the number of cycles before failure at a given constant stress amplitude. As the stress cycles identified on the results of the OWT simulation are not constant, a linear aggregation method called *Miner's rule* gathers the elementary damages over the stress time series studied.

Stress cycles identification. Offshore wind turbine simulators as DIEGO, deliver a time-dependent stress tensor. To ease the manipulation of this tensor, the equivalent Von Mises stress is computed, turning a multiaxial stress into an equivalent uniaxial stress. One can also consider a “plane strain” hypothesis on the Cauchy stress tensor $\underline{\sigma}$, which is expressed as:

$$\underline{\sigma} = \begin{pmatrix} \sigma_{11} & \sigma_{12} & 0 \\ \sigma_{21} & \sigma_{22} & 0 \\ 0 & 0 & \sigma_{33} \end{pmatrix}. \quad (2.12)$$

This assumption simplifies the expression of the equivalent Von Mises stress:

$$\sigma_{VM} = \sqrt{\frac{1}{2} [(\sigma_{11} - \sigma_{22})^2 + (\sigma_{22} - \sigma_{33})^2 + (\sigma_{33} - \sigma_{11})^2] + 3\sigma_{12}^2}. \quad (2.13)$$

Stress cycles can now be identified on the equivalent Von Mises stress time series. The usual method to identify fatigue stress cycles is called *rainflow counting* (Dowling, 1972). In this approach, fatigue stress cycles are only defined by their amplitude (also called “range”) and mean value, regardless of their chronology. Rainflow counting returns a list of stress ranges identified denoted by s in the following.

S-N curve. The S-N curve is also called the “Wöhler curve” after the pioneer work of August Wöhler, who demonstrated that fatigue damage was at the origin of railway accidents in the mid-19th century (Schütz, 1996). As a result of repeated fatigue experiments, this tool determines the number of similar stress cycles necessary to reach a fatigue ruin for a defined stress cycle amplitude. Its values depend on the material studied and on external conditions (i.e., in the offshore industry, the S-N curves distinguish the fatigue in the air vs. underwater).

A well admitted simplification of the S-N curve is to consider it as log-linear¹ on two segments:

$$\log(N_c(s)) = \begin{cases} \log(a_1) - m_1 \log(s), & \text{for } s \in [s_{\min}, s_e] \\ \log(a_2) - m_2 \log(s), & \text{for } s \in [s_e, s_{\max}] \end{cases} \quad (2.14)$$

Where N_c is the predicted number of cycles to failure for stress range s , m is the negative inverse slope of the S-N curve, $\log(a)$ is the intercept of log N-axis by the S-N curve, s_{\min} is the minimal (resp. maximal) stress range identified by the rainflow counting, and s_e is the stress range axis of the intersection of the two log-lines formed by the S-N curve.

¹The logarithms related to the S-N curves in this document are logarithms in base 10.

The expression of this curve in two linear segments arise from the concept of endurance limit of a material, s_e , under which the effect of fatigue on a material should be considerably smaller. According to DNV-RP-C203 (2016), the S-N curve is altered for welded tubular joints by taking into account the tube's thickness:

$$N_c(s) = \begin{cases} a_1 \left(s \left(\frac{t}{t_{\text{ref}}} \right)^h \right)^{-m_1}, & \text{for } s \in [s_{\min}, s_e] \\ a_2 \left(s \left(\frac{t}{t_{\text{ref}}} \right)^h \right)^{-m_2}, & \text{for } s \in [s_e, s_{\max}] \end{cases} \quad (2.15)$$

With t_{ref} the reference thickness (for tubular welded joints $t_{\text{ref}} = 25$ mm); t the plate thickness, and h the thickness exponent. The numerical values considered in the present work derive from the Section 2.4.6 of DNV-RP-C203 (2016), reproduced in Table 2.1.

Table 2.1 S-N curve numerical values of welded tubular joints in different environmental conditions (source: DNV-RP-C203 2016)

Environment	m_1	$\log(a_1)$	m_2	$\log(a_2)$	h
Air	3.0	12.48	5.0	16.13	0.25
Seawater with cathodic protection	3.0	12.18	5.0	16.13	0.25
Seawater free corrosion	3.0	12.03	3.0	12.03	0.25

Non-zero mean correction. Most S-N curves are built over zero mean stress cycles, however, different empirical models were developed to consider different stress mean s_m (Suresh, 1998). The S-N curve becomes a three-dimensional envelope depending on the number of cycles N_c , the stress amplitude s , and the mean stress s_m . The “Goodman line” and the “Gerber parabola” are two models relating the stress amplitude s to the mean stress s_m :

$$\text{Goodman : } \frac{s}{s_e} + \frac{s_m}{R_m} = 1 \quad (2.16)$$

$$\text{Gerber : } \frac{s}{s_e} + \left(\frac{s_m}{R_m} \right)^2 = 1 \quad (2.17)$$

Where the material’s yield stress is denoted by R_m and the endurance limit by s_e . The Haigh diagram represented in the Fig. 2.11 is a slice of the three-dimensional envelope for fixed values of fatigue endurance (i.e., number of cycles). By comparing the two models visually, the Goodman line is more conservative and is mostly used in the literature. Further discussion in the field of wind turbines was proposed in the early 2000s with a focus on the fatigue endurance of glass fiber materials (Sutherland, 2000). In the present work, the non-zero correction presented above are not considered as the values of mean stress were found to be negligible compared to the yield stress of the steel material studied.

Cumulative damage theory. A popular approach to assess the damage cumulated on a stress time series is to consider the fatigue contribution of each stress cycle according to the S-N curve. Palmgren-Miner’s rule defines the *cumulative damage* d_c by summing the fatigue

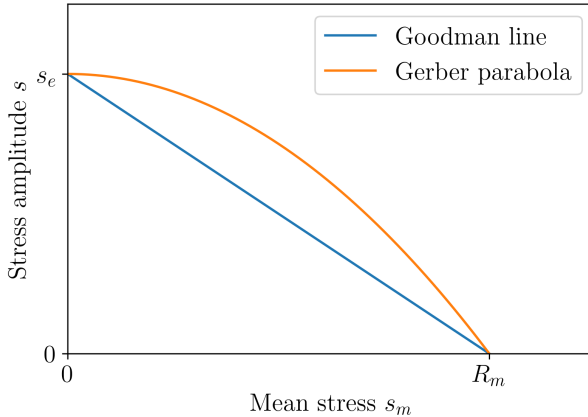


Figure 2.11 Illustration of the Haigh diagram representing the combination of stress mean and amplitude leading to the same fatigue endurance.

contributions of each stress cycle k , regardless of their order of appearance:

$$d_c = \sum_{j=1}^k \frac{1}{N_c(s^{(j)})}. \quad (2.18)$$

In this theory, the material reaches fatigue ruin when the cumulative damage exceeds one. A common practice when using Palmgren-Miner's rule is to gather the stress cycles in a set of bins. This practice induces an integration error, which becomes significant as the number of bins is reduced. In the following, the cumulative damage is computed without binning, as defined in Eq. (2.18).

Spectral methods were also introduced to quantify fatigue damage in the late 80s. The main idea is to infer a PDF over the amplitudes of the stress cycles identified by rainflow counting, typically using a mixture of parametric distributions. From this PDF, one can derive the fatigue endurance and therefore a cumulated damage (see further details in the review of [Dirlik and Benasciutti 2021](#)). In the context of wind turbine fatigue assessment, spectral approaches showed to be unsuited in some cases (e.g., for blades' fatigue [Ragan and Manuel 2007](#)). Overall, fatigue estimation in the time-domain does not represent important computational effort compared to the simulation of the wind turbine's physics.

Nonlinear fatigue models were developed in the 90s ([Fatemi and Yang, 1998](#)) to take into account the order in which the loading cycles were applied to the structure. For offshore wind turbine applications, the recent work of [Rocher et al. \(2020\)](#) studied a probabilistic version of a nonlinear fatigue models. Unfortunately, this refined approach requires a larger computational effort and the calibration over experimental tests of various parameters ([Freyssinet et al., 2023](#)).

2.4 Design and operation practices

The design and operation of offshore wind turbines is at the intersection of various engineering, environmental and social considerations. Regardless of the different bottom-fixed or floating

technologies, OWTs are dynamically excited structures evolving in a harsh offshore environment. To operate such assets over up to 25 years of lifespan, multiple aspects should be assessed, from soil modeling, studies of environmental impact, grid integration, manufacturing quality, port logistics, to marine growth management, and maintenance. This section resumes the main types of OWT technologies, as well as the main design and operation practices.

2.4.1 Types of technologies and preliminary design

The multiple OWTs technologies developed over the last two decades can be gathered into two groups: bottom-fixed or floating technologies. Fig. 2.12a and 2.12b respectively illustrates the different types of bottom-fixed or floating technologies. At this stage, the bottom-fixed solutions present more maturity while floating technologies are still transitioning from the phase of large demonstrators to industrial wind farms. In France, the current development of offshore wind energy lead to the construction of the two first industrial projects (both managed by EDF Renewables). On the coast of Saint-Nazaire, 80 bottom-fixed wind turbines were built on monopile foundations, altogether producing up to 480 MW. On the Mediterranean coast, the first French industrial floating project was recently installed 20 km offshore the coast of Marseille. This pilot project, called “*Provence grand large*”, is composed of three turbines operating on so called “tension-leg platforms”, delivering 25 MW of nominal power.

In order to lift water depth limitations associated with bottom fixed technologies (technical limit around 60 meters), floating pilot projects emerge across the world. However, the wind energy industry still tests different floating technologies in terms of cost efficiency and durability (as listed in [MacKinnon et al. 2022](#)). An example of some farm projects with different types of technologies is described hereafter:

- **Semi-submersible:** a pilot project of three 10MW turbines called “*les éoliennes du Golfe du Lion*” in the south of France relies on a semi-submersible technology developed by the company Principle Power ([Cermelli et al., 2018](#)).
- **Tension-leg:** a pilot project of three 8MW turbines called “*Provence grand large*” exploits tension-leg platforms co-developed between the IFPEN national laboratory and the company SBM ([Caillé et al., 2017](#)).
- **Barge:** a pilot project of three 10MW turbines called “EOLMED” uses the floater developed by the company Ideol ([Guignier et al., 2016](#)).
- **Spar:** the Norwegian oil and gas company Equinor chose the spar technology ([Driscoll et al., 2016](#)) to equip its floating wind farm of 88MW, named “Hywind Tampen”.

The turbines installed offshore over bottom-fixed foundations or floating structures present the same properties and components. As described in Fig. 2.13, the structure of a wind turbine is composed of blades made in composite materials, while the tower, the transition piece and foundation (e.g., monopile) are made out of steel. The steels used for the foundation and the tower are typical structural steels (i.e., steels with low carbon concentration such as the S355).

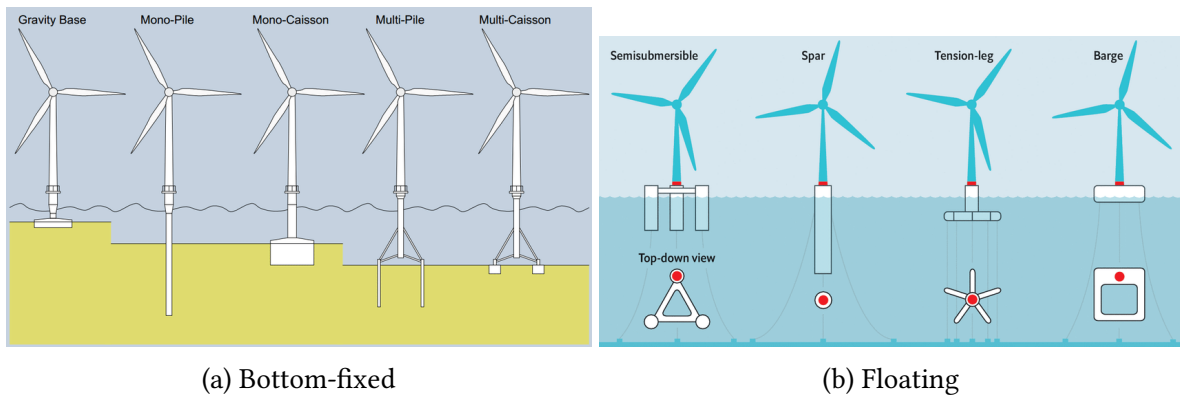


Figure 2.12 Main offshore wind turbine technologies (sources: Ahmed et al. 2015; Mei and Xiong 2021).

Inside the nacelle, the gearbox adapts the rotation speed to suit the energy conversion system (i.e., generator). To improve the reliability of the components, manufacturers offer without gearboxes, called “direct-drive”. This technology is relevant offshore, as the maintenance constraints are higher. However, the corresponding generators used in this situation operate at lower rotation speed. Adapting the generators significantly increase their weight and requires the use of larger permanent magnets increasing their price.

The construction of an offshore wind farm requires several years of project planning, administrative procedures, consultation of the public opinion, and design. Internationals standards define the recommended practices and requirements related to the design and operation of OWTs. Among them, the IEC 61400 is subdivided in many parts, including the general one ([IEC-61400-1, 2019](#)) and other parts detailing specific topics. To validate the structural integrity of a wind turbine design, the standards recommend simulating the behavior of the OWT (using the methods described in Section 2.3) for many environmental conditions, called “design load cases” (DLC). As the environmental conditions depend on the site studied, the standards provide generic DLCs depending on a rough classification of the environmental conditions. Following the terminology in civil engineering, the structure is designed for “fatigue limit states” (FLS) and “ultimate limit states” (ULS) with respect to the environmental conditions. For fatigue, advanced sampling methods relying on environmental data measured on site will be introduced in Chapter 4. Beyond the main solicitations resulting from environmental loading, various aspects should be considered around offshore wind turbines.

2.4.2 Further design considerations

The present section focuses on different topics to be addressed ahead of, or during the design and operation of offshore wind turbines.

Soil modeling. The accurate geotechnical description of an offshore site plays an important role in the design and stability of bottom-fixed offshore wind turbines. The seabed soil properties are far from uniform in a wind farm, forcing the designer to adapt the foundations within a

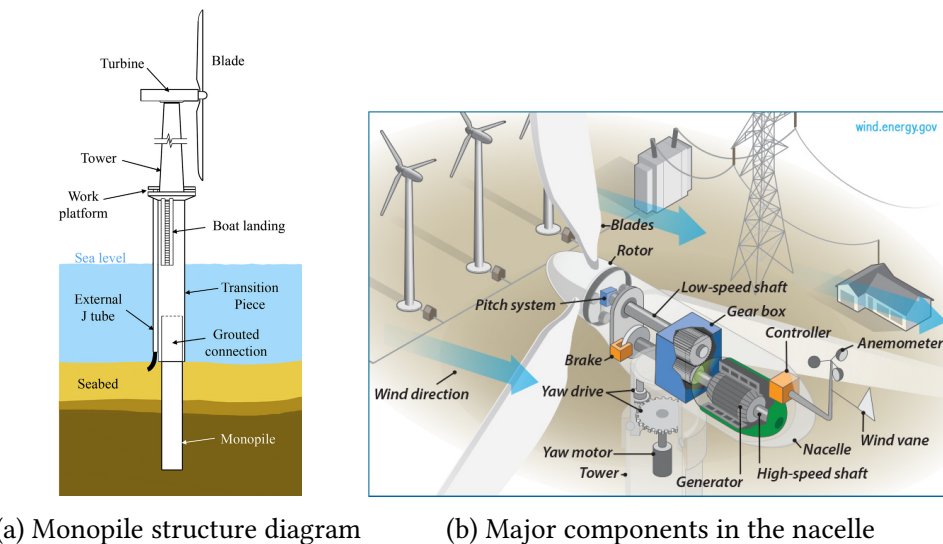


Figure 2.13 Diagrams of an offshore wind turbine structure (source: (Chen et al., 2018)) and nacelle (source: US ODE).

farm. Prior to the installation, geotechnical surveys and soil testing are conducted to assess parameters such as soil composition, density, strength, and seabed stability.

To model the dynamic behavior of foundations, certification companies adapted their methods from the oil & gas industry to the offshore wind energy (DNV-ST-0126, 2018). For monopile foundations, the “ $p - y$ ” method is often used to model soil-structure interactions. Assuming that these interactions are purely lateral, this method defines a set of non-linear lateral springs along the foundation’s height. Together, the springs model the relation between the soil resistance “ p ” and the lateral displacement “ y ”. Generally speaking, monopile foundations for OWT tend to be more rigid than for oil & gas platforms, as the cyclic loading on wind turbines induces more fatigue (see the case-study presented in Le et al. (2014)). However, various contributions in wind energy extended the use of $p - y$ curves to the case of multidirectional and irreversible displacements (Lovera, 2019). In summary, geotechnical considerations are essential for offshore wind turbine design, and the variability of soil properties within a wind farm necessitates a tailored approach to foundation design. Finally, the consideration of uncertainties in this field is still an open research topic (Reale et al., 2021).

Marine growth. The bio-colonization of offshore structures and submarine cables is a significant concern in the maintenance and operation of OWTs. Elements exposed to the colonization of marine organisms, such as mussels, can cause several adverse effects. Firstly, the added weight increases the mass of the turbine and its foundation, potentially changing the dynamics of the systems and its structural integrity (Ameryoun et al., 2019; Schoefs and Tran, 2022). Secondly, marine growth changes the surface’s roughness of the submerged components, which can create fluctuating hydrodynamic loads and vibrations (Marty et al., 2021). To limit its impact on the reliability of OWTs, this phenomenon is addressed with regular preventive cleaning measures as part of the maintenance planning.

Global scour. The large-scale erosion of seabed sediment around bottom-fixed offshore wind turbine foundations, also called “global scour”, poses different problems. The stability of the foundation is first reduced, potentially leading to tilting. Moreover, the load distributions changes, causing uneven stresses and increased fatigue. Finally, submarine cable exposure increases the risk of damage and electrical faults. As global scour is a critical element of the long-term OWT reliability, various mitigation measures are reviewed in [Fazeres-Ferradosa et al. \(2021\)](#), including scour protection, and scour-robust foundation design.

Port logistics. In the installation and maintenance of such large scale systems, port logistics plays an important role considering the international supply chain involved. The coordination, transportation and assembly of massive wind turbine components, foundations, and supporting infrastructure requires meticulous planning and execution. In accordance, the costs of handling operations and maintenance represent an important share of the *levelized cost of energy* (LCOE) ([Shields et al., 2021](#)).

In his review of OWT installation techniques, [Jiang \(2021\)](#) describes the foundations’ and components’ installation processes depending on the OWT technology. Because of their large scale, most structural assembly (e.g., blades, or floater) are done on dedicated port docks, making the port choice critical. The assembled turbines are then transferred offshore with specialized vessels, such as installation jack-ups. Timing and synchronization are critical, as weather windows for handling operations can be limited.

Grid integration. Unlike traditional centralized energy production plants (i.e., nuclear and fossil), wind energy has considerable impact on the grid management. The intermittency of offshore wind generation is driven by variable wind conditions, which disrupts the electricity supply ([Heier, 2014](#)). Then, grid balancing becomes more complex as variable and distributed production sources are introduced. Wind turbine integration often require more flexibility from the grid, resulting in grid infrastructure upgrades (e.g., energy storage) and advanced grid management.

Environmental impact and social acceptance. The fast development of offshore wind turbines in Europe raises questions regarding environmental and social impact. In their review, [Galparsoro et al. \(2022\)](#) showed that the installation and operation was shown to disrupt marine ecosystems. Further studies should be realized to better understand the reliance of the ecosystems to this change. This industry also affects other marine activities (e.g., fishing or tourism), and coastal landscapes, which need to be discussed during the regional marine spatial planning. Finally, social acceptance of offshore wind projects varies across Europe, often split between local disturbances and the regional economic activity generated.

Manufacturing quality. The manufacturing of structural wind turbine components is subject to several uncertainties that can affect the overall quality and performance of OWTs. For example, the manufacturing process of composite blades can lead to inconsistencies in the final

product. Imperfections in the composite material, like air pockets or delamination, can weaken the blades and reduce their lifespan. Additionally, variations in manufacturing processes can result in differences in blade weight, which impacts the turbine's performance. Regarding steel components, OWTs are mostly assembled by bolted and soldered joint. Inconsistent soldering, variations in material properties, and potential flaws in the joints can compromise the structural integrity of OWTs (Veers et al., 2019). These uncertainties in manufacturing quality can pose significant challenges in ensuring the reliability and longevity of the structures. Note that at the design phase, *stress concentration factors* are defined by standards to take into account the local change in material properties created by soldering. Rigorous quality control, material testing, and manufacturing standards are essential to maintain the safety and efficiency of wind energy installations.

Maintenance and end-of-life management. To ensure the continued performance and availability of wind turbines, advanced maintenance planning is essential. Maintenance activities involve inspections, repairs, component replacements, and addressing issues as corrosion, or electrical faults. Preventive maintenance strategies (reviewed by Ren et al. (2021)) minimize the asset's unavailability and extends its lifespan.

Once the wind farms reach their planned lifetime (typically between 20–25 years), the operator has the choice between decommissioning, “repowering”, or “revamping” the assets. Usually, revamping implies an intermediate renovation of the WT. In most cases, the underperforming major components are replaced while the structural components are kept. Alternatively, repowering is a strategy reusing the foundations of a wind farm to install brand new turbines. This approach is often an opportunity to increase the scale and performances of the old turbines.

As the first generation of wind farms currently reach their end-of-life, an important problematic raises from recycling large amounts of blades made out of composite materials. Different processes for recycling composite material are reviewed in Jensen and Skelton (2018), including mechanical, pyrolysis and chemical techniques. However, recycling composites is a complex and energy-consuming operation, that needs to be further studied. The recent lifecycle study of floating OWT in the Mediterranean region by Pulselli et al. (2022) showed that effective maintenance and proper decommissioning planning are essential for ensuring cost-effective yet durable lifecycle management.

2.5 Uncertain inputs

Following the general diagram of uncertainty quantification in Fig. 1, this section focuses on the definition of the uncertain inputs and their corresponding probabilistic model (step B). In our case, the generic term of “inputs” refers to the inputs to the wind turbine numerical model illustrated in Fig. 2.6, which will be considered as random afterwards.

The random variables studied in this work are split into two groups (assumed independent) which are respectively called *environmental variables* and *system variables*. First, the

environmental variables are a collection of variables characterizing the long-term metocean conditions near a wind farm. Even if the associated random vector presents a complex dependence structure, this source of variability is well-defined after the wind potential measurement campaigns.

The second group of uncertain inputs is related to the wind turbine system. A wide range of uncertainties can be taken into account in such systems, such as material properties, manufacturing quality, soil conditions, control error, corrosion, marine growth, aerodynamic damping, etc. Among them, a restricted list of four variables are kept according to sensitivity analysis results from the literature and expert knowledge.

2.5.1 Environmental inputs

During the planning and operation of a wind farm project, the metocean conditions are studied using different sources of information. At the early stage, datasets generated by fine mesoscale numerical simulation can be used to assess the wind potential. This was typically the case during the call for tenders² issued by the French government regarding the construction of two floating offshore wind farm in the south coast of Brittany (of respectively 250 and 500 MW of nominal power). Open-access environmental data of the sea-states in this reagion were available, as a result of mesoscale simulations (Raoult et al., 2018) realized by EDF R&D. In a second time, the local conditions are measured using a meteorological mast with wind speed cup anemometers at different heights and wave boys are generally installed in the vicinity of the future farm. As a cheaper alternative to met masts, new measurement technologies such as floating LIDARs (standing for “light detection and ranging”) were studied by Gottschall et al. (2017). Then, different adequation methods between the local measures and the data obtained by mesoscale simulations were reviewed in Sempreviva et al. (2008). Finally, after the installation of the turbines, the acquisition system (usually called SCADA, for “supervisory control and data acquisition”) measures wind conditions with a sampling period of ten minutes.

In the present work, two wind farms projects are partially studied: the Teesside wind farm, operating in the North Sea, and the south Brittany floating project, at the stage of tenders call. Table 2.2 summarizes the variables considered as random hereafter. The inference of such data will be discussed in Chapter 3 of this manuscript. Note that the environmental data resulting from the SCADA system of the Teesside wind farm is confidential, and will be represented as anonymized data in the following.

2.5.2 System inputs

As mentioned earlier, multiple parameters in a wind turbine system can be considered as uncertain. Our study focuses on the effects of uncertainties on the fatigue damage over the structure. Therefore, the literature review of the sensitivity analysis on offshore wind turbine fatigue helped us narrow down a few system variables. Petrovska (2022) explored the sensitivity

²<https://eolbretsud.debatpublic.fr/>

Name	Notation	Description
Mean wind speed	U	10-min. average horizontal at 10m
Turbulence	σ_s	10-min. standard deviation
Wind direction	θ_{wind}	Wind directions
Significant wave height	H_s	Significant wave height per hour
Peak wave period	T_p	Peak 1-hour spectral wave period
Wave direction	θ_{wave}	Wave directions

Table 2.2 Marginal distributions of the environmental random variables

analysis of many variables on the fatigue of a wind turbine in Teesside. Even if the use of the Morris method is questionable, the results allowed to screen out some variables. For example, the uncertainties related to the corrosion, the wind shear exponent, or the nacelle mass showed a limited impact on the fatigue. By crossing the conclusions of various research with the expert knowledge among partners from the HIPERWIND European project, the system variables considered uncertain in the following are summarized in Table 2.3. Each of them is assumed independent, with a marginal probabilistic model arising from the literature.

Name	Notation	Marginal model	Description
Soil coefficient	S	Normal ($\mu = 1., \sigma = 0.3$)	Applied to the soil stiffness matrix
Yaw misalignment	θ_m	Normal ($\mu = 0., \sigma = 0.3$)	Error in wind alignment
SN curve coefficient	a	Log-normal ($\mu = 1, \sigma = 0.3$)	See Guédé et al. (2007)
Critical damage	D_{cr}	Log-normal ($\mu = 1, \sigma = 0.3$)	See Drexler and Muskulus (2021)

Table 2.3 Marginal distributions of the system random variables

2.5.3 Probabilistic fatigue assessment

The definition of a fatigue endurance model has a main impact on fatigue damage assessment. However, the S-N curves usually describing the endurance of a material are built on repeated laboratory experiments. Even if the need for random S-N curves has long been expressed in the field of fatigue experiments (Lieudarde, 1982), their probabilistic description was better formalized in (Guédé et al., 2007; Sudret, 2013).

The models proposed in Guédé et al. (2007) are based on the experimental procedure used to build the S-N curves. For identical steel specimens, a cyclic loading with fixed amplitude is repeated until fatigue ruin. Because of variations in the material's microstructure, the fatigue endurance for the same cyclic solicitation is random. This variation is commonly assumed to follow a log-normal distribution in the literature. A probabilistic model of the S-N curve naturally comes:

$$\log(N_c(s, \omega)) = \log(a) - m \log(s) + \log(\varepsilon(\omega)) \quad (2.19a)$$

$$\Rightarrow N_c(s, \omega) = a s^{-m} \varepsilon(\omega), \quad (2.19b)$$

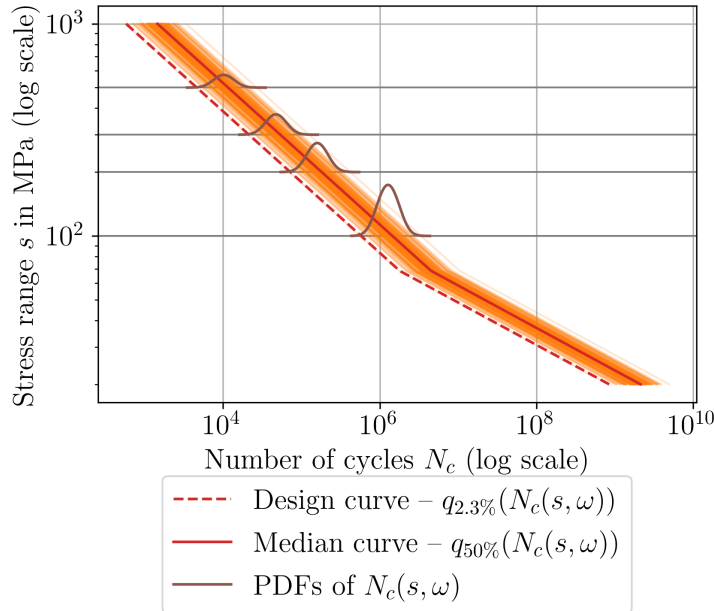


Figure 2.14 Illustration of a probabilistic S-N curve according to the model defined in Guédé et al. (2007).

where $\log(\varepsilon(\omega)) \sim \mathcal{N}(0, \sigma_{N_c} = 0.2)$ is assumed when no measurement is available (according to Appendix F.5 from DNV-RP-C203 2016).

This uncertainty can be injected in the Miner-Palmgren rule defined in Eq. (2.18):

$$d_c(\omega) = \sum_{j=1}^k \frac{1}{N_c(s^{(j)}, \omega)} = \sum_{j=1}^k \frac{1}{a (s^{(j)})^{-m} \varepsilon(\omega)} = \frac{1}{\varepsilon(\omega)} \sum_{j=1}^k \frac{1}{a (s^{(j)})^{-m}} \quad (2.20)$$

Then, this uncertainty can be assessed as a pure post-processing of fatigue damage results computed with a single deterministic S-N curve.

In wind energy standards, S-N curves for design are actually a conservative envelope of the measured fatigue endurance. Annex F.7 from DNV-RP-C203 (2016) describes how to define a design S-N curve from fatigue measures. Assuming that the fatigue endurance follows a Gaussian distribution (on logarithmic scale), the design S-N curve $N_c^{\text{design}}(s)$ is the curve at two standard deviations σ_{N_c} below the median curve.

Using the design S-N curve given in Section 2.4.6 DNV-RP-C203 (2016) and the normality assumption, one can reconstruct the median S-N curve by taking:

$$q_{50\%}[\log(N_c(s, \omega))] = \log(N_c^{\text{design}}(s)) + 2 \sigma_{N_c}. \quad (2.21)$$

Fig. 2.14 illustrates the design curve defined by DNV for tubular joints (in Section 2.4.6) and the reconstructed probabilistic model according to the previous assumptions.

2.6 Conclusion

This chapter proposed an overview on offshore wind turbine modeling and design. It introduced concepts related to the description and simulation of metocean conditions. The impact of the wake on the performance and on unsymmetrical fatigue loading was also explained. Then, the different theories considered in OWT modeling were introduced such as aerodynamics, hydrodynamics, structural dynamics and control. A variety of softwares implementations exist for this purpose, but a special attention was brought on DIEGO a numerical model developed by EDF R&D. As a perspective, uncertainty quantification could benefit from the different fidelities proposed to model OWT systems presenting very nonlinear transient phases.

To understand the design of OWTs, the most common technologies of bottom-fixed and floating turbines were presented. Then, a focus on a few critical topics to be considered during design and exploitation was proposed. In the light of the previous elements, the variables considered as random in this work were listed with a particular focus on probabilistic fatigue.

This growing industry faces various challenges, for example related to the important use of primary commodities, the cohabitation of offshore dynamic structures with an ecosystem, composite materials recycling, etc. Uncertainty quantification is a tool to understanding some of these problematics, however, many uncertainties are hard to characterize and quantify. For example, manufacturing quality issues were revealed by Siemens Gamesa³ regarding wrinkles on the surface of some blades.

³L. Pitel and R.Millard. (August 7 2023). Siemens Energy warns of €4.5bn loss from ailing wind turbine division. *Financial Times*. <https://www.ft.com/content/df8947cd-4bab-46ff-804e-b28de4b5a0f0>

PART II:

CONTRIBUTIONS TO UNCERTAINTY QUANTIFICATION AND PROPAGATION

*Le doute est un état mental désagréable,
mais la certitude est ridicule.*

VOLTAIRE

Chapter **3**

Kernel-based uncertainty quantification

3.1	Introduction	90
3.2	Dependence modeling with nonparametric copula	91
3.2.1	Preliminary definitions and properties	92
3.2.2	Empirical and checkerboard copula	94
3.2.3	Empirical Bernstein and Beta copula	94
3.3	<i>Copulogram</i> : a tool for multivariate data visualization	99
3.3.1	From pairwise plot to copulogram	99
3.3.2	Implementation in a Python package	99
3.4	Semiparametric inference of the South Brittany metocean conditions	102
3.4.1	Inference of the marginals	102
3.4.2	Nonparametric inference of the dependence	102
3.4.3	Goodness-of-fit and discussion	102
3.5	Quantifying and clustering the wake-induced perturbations within a wind farm	105
3.5.1	Uncertainty propagation in a wake model	106
3.5.2	Statistical metric of wake-induced perturbations	107
3.5.3	Summary and discussion	110
3.6	Conclusion	111

Parts of this chapter are adapted from the following references:

A. Lovera, E. Fekhari, B. Jézéquel, M. Dupoiron, M. Guiton and E. Ardillon (2023). “Quantifying and clustering the wake-induced perturbations within a wind farm for load analysis”. In: *Journal of Physics: Conference Series (WAKE 2023)*.

E. Vanem, E. Fekhari, N. Dimitrov, M. Kelly, A. Cousin and M. Guiton (2023). “A joint probability distribution model for multivariate wind and wave conditions”. In: *Proceedings of the ASME 2023 42th International Conference on Ocean, Offshore and Arctic Engineering (OMAE 2023)*.

3.1 Introduction

The main sources of solicitation in offshore design reside in the metocean conditions. To accurately verify a structural design against the joint wind and wave conditions, these random excitations must be carefully modelled. Offshore structures are usually certified against ultimate limit states (related to the occurrence of extreme metocean conditions) and fatigue limit states (related to the average fatigue over the metocean conditions). In this context, the probabilistic framework is typically used to model the joint distribution of random variables describing the metocean conditions (listed in Section 2.5).

Note that a given probabilistic model might describe well the central behavior of the environmental distribution but not its tail behavior (and vice-versa). Extreme value theory develops specific methods to model the far tails of distributions (Beirlant et al., 2006). Modeling the tails is not the priority in the present work since the focus is on mean fatigue estimation.

The environmental random variables studied present different particularities. First, an offshore wind turbine project leads to the collection of an important amount of metocean data (possibly merged with data from mesoscale simulations). Second, their dependence structure is complex, making the probabilistic modeling more complicated.

This chapter explores different aspects of the environmental conditions’ uncertainty quantification. The theory of some nonparametric copulas is introduced before their use in metocean conditions inference. A semiparametric approach is applied on the South Brittany data, mixing parametric modeling of the marginals with nonparametric modeling of the copula. To visually analyze multivariate distributions, the *copulogram* is a new tool that decomposes the marginal effects and the dependence structure of a joint distribution.

At the scale of a wind farm, each turbine perceives different metocean conditions as the wake of other turbines creates wind perturbations. To study this perturbation, an engineering wake model (see Section 2.2.2) was used to obtain one perturbed environmental distribution per turbine. This work applies a kernel-based discrepancy (the maximum mean discrepancy) to compare wake induced perturbations. In a second time, this discrepancy is used to gather wind

turbines perceiving similar perturbations. This clustering can be used to perform uncertainty propagation at the farm scale by considering a few turbines with are representative of a cluster.

3.2 Dependence modeling with nonparametric copula

In uncertainty quantification, the lack of knowledge can lead to rough assumptions regarding the dependence modeling. However, an accurate representation of the uncertain inputs is of prime importance. For example, the work of [Torre et al. \(2019\)](#) demonstrates the influence of the dependence model on the estimation of rare event probabilities by studying the same problem with different copula models.

When inferring a probabilistic model over a multivariate dataset, one can decompose the problem into the fit of a set of marginals and the fit of a copula (see the Sklar Theorem 1). In the case of metocean conditions, the fit of the marginals is not problematic considering the amounts of data available. However, the complex dependence structure appears to be more challenging. Different strategies to model the dependence for multivariate distributions are shortly summarized hereafter:

- **Vine copulas** (also known as pair copula) decompose the joint distribution as a product of conditioned bivariate copulas organized in a tree-like structure called a vine. This approach proved to be very efficient, but it requires the definition of the vine and the bivariate parametric copulas ([Joe and Kurowicka, 2011](#)).
- **Conditional modeling** defines the joint distribution as a product of univariate conditional distributions. In practice, the parameter of a marginal are defined as a function of other marginals (see e.g., [Vanem et al. 2023](#)).
- **Multivariate KDE** is another way to capture the dependence together with marginal effects. As the dimension and the size of the dataset increase, this method become less tractable ([Wand and Jones, 1994](#)).
- **Nonparametric copulas** are methods uniformly approximating an empirical copula without any assumption on a dependence structure. They will be further described and used for metocean conditions inference in the present chapter.

Remark 2. The strategy referred as “conditional modeling” can in fact be expressed as a copula ([Vanem, 2016](#)) for continuous variables. For example, in the bivariate case of a continuous random vector $\mathbf{X} = (X_1, X_2)$ with PDF $f_{\mathbf{X}}(\mathbf{x})$, CDF $F_{\mathbf{X}}(\mathbf{x})$ and density copula c :

$$f_{\mathbf{X}}(\mathbf{x}) = f_{X_1}(x_1) f_{X_2|X_1}(x_2|x_1) = f_{X_1}(x_1) f_{X_2}(x_2) c(F_{X_1}(x_1), F_{X_2}(x_2)) \quad (3.1a)$$

$$\Leftrightarrow c(F_{X_1}(x_1), F_{X_2}(x_2)) = \frac{f_{X_1}(x_1) f_{X_2|X_1}(x_2|x_1)}{f_{X_1}(x_1) f_{X_2}(x_2)} \quad (3.1b)$$

The notions related to the copula theory are further introduced in the monographs of [Nelsen \(2006\)](#); [Joe \(2014\)](#); [Durante and Sempi \(2015\)](#) while the key properties are introduced hereafter.

3.2.1 Preliminary definitions and properties

Let us consider a random vector $\mathbf{X} \in \mathcal{D}_x \subseteq \mathbb{R}^d$ defined on a probability space $(\Omega, \mathcal{A}, \mathbb{P})$. Its probability distribution $\mathbb{P}_{\mathbf{X}}$ can be represented by a CDF $F_{\mathbf{X}}$ and PDF $f_{\mathbf{X}}$. The functional definition of a *d-dimensional copula* (or simply “d-copula”) is a density function $C : [0, 1]^d \mapsto [0, 1]$ whose marginals are uniformly distributed on $[0, 1]$.

Theorem 3 (Copula). *A function $C : [0, 1]^d \mapsto [0, 1]$ is a d-copula if, and only if, it presents the following properties:*

- *The function C is “grounded” (also called “anchored”):*

$$C(u_1, \dots, u_d) = 0 \text{ if } u_j = 0, \forall j \in \{1, \dots, d\};$$
- *The marginals of C are uniform, then:* $C(1, \dots, u_j, \dots, 1) = u_j, \forall j \in \{1, \dots, d\}$;
- *The function C is “d-increasing”, meaning that for any hyperrectangle $A \subset [0, 1]^d$, the corresponding volume induced by C is positive (see [Durante and Sempi \(2015\)](#) p.7).*

A copula is bounded by two functions according to the Fréchet-Hoeffding bounds.

Theorem 4 (Fréchet-Hoeffding bounds). *If a function $C : [0, 1]^d \mapsto [0, 1]$ is a d-copula, then it respects the following bounds for all $\mathbf{u} \in [0, 1]^d$:*

$$W(\mathbf{u}) = \max(1 - d + u_1 + \dots + u_d, 0) \leq C(\mathbf{u}) \leq M(\mathbf{u}) = \min(u_1, \dots, u_d). \quad (3.2)$$

Where the upper bound M is still a copula while the lower bound W is only one for $d = 2$.

The rank transform plays an essential role to understand copulas. Considering a continuous random vector $\mathbf{X} \in \mathcal{D}_x$ and the sample $\mathbf{X}_n = \{\mathbf{x}^{(1)}, \dots, \mathbf{x}^{(n)}\} \sim \mathbf{X}$, its *ranks* $\mathbf{R}_n = \{\mathbf{r}^{(1)}, \dots, \mathbf{r}^{(n)}\} \in \mathbb{N}^n$ correspond to the indexes of its order statistics:

$$r_j^{(i)} = n \widehat{F}_{X_j}(x_j^{(i)}) = \sum_{l=1}^n \mathbb{1}_{\{x_j^{(l)} \leq x_j^{(i)}\}}, \quad \forall j \in \{1, \dots, d\}, i \in \{1, \dots, n\}, \quad (3.3)$$

where \widehat{F}_{X_j} stands for the marginal empirical CDF associated to the random variable X_j .

Theorem 5 (Rank-invariance). *Considering a random vector $\mathbf{X} = (X_1, \dots, X_d)$, a set of mappings $\{r_j(\cdot)\}_{j=1}^d$, and the image random vector $\mathbf{R} = (r_1 \circ X_1, \dots, r_d \circ X_d)$. If the mappings are strictly increasing (which is the case for the rank transform introduced in Eq. (3.3)), then, the copula associated to \mathbf{R} is invariant by transformation: $C_{\mathbf{X}} = C_{\mathbf{R}}$. A proof is presented in [Durante and Sempi \(2015\)](#) p. 57.*

Transforming in the ranks generally reduces the effect of outliers and ensures more robust estimates. The invariance by rank transform of copulas allows the estimation of different *dependence measures* in the ranked space.

Spearman's rho. Is a well-known dependence measure, also called the “Spearman's rank correlation coefficient”, which is defined for two random variables X_i, X_j as:

$$\rho^S(X_i, X_j) = \frac{\text{Cov}(r_i(X_i), r_j(X_j))}{\sigma_{r_i(X_i)} \sigma_{r_j(X_j)}}, \quad (3.4)$$

an equivalent definition exists, using the copula C between the joint distribution of X_i and X_j and the independent copula $\Pi(u_i, u_j) = u_i u_j$:

$$\rho^S(X_i, X_j) = 12 \int_{[0,1]^2} C(u_i, u_j) du_i du_j - 3 = 12 \int_{[0,1]^2} (C(u_i, u_j) - \Pi(u_i, u_j)) du_i du_j. \quad (3.5)$$

Kendall's tau. Also referred to as the “Kendall's rank correlation coefficient”, is defined for a pair of random variables (X_i, X_j) and their respective independent copies (X'_i, X'_j) as:

$$\tau(X_i, X_j) = \mathbb{P}\left((X_i - X'_i)(X_j - X'_j) > 0\right) - \mathbb{P}\left((X_i - X'_i)(X_j - X'_j) < 0\right), \quad (3.6)$$

and can also be defined using the copula C between the joint distribution of the two random variables:

$$\tau(X_i, X_j) = 4 \int_{[0,1]^2} C(u_i, u_j) dC(u_i, u_j) - 1 = 1 - 4 \int_{[0,1]^2} \frac{\partial C(u_i, u_j)}{\partial u_i} \frac{\partial C(u_i, u_j)}{\partial u_j} du_i du_j \quad (3.7)$$

These dependence measures fully rely on the copula and are both bounded between -1 and 1. Further properties and estimators of Spearman's rho and Kendall's tau are presented in [Durante and Sempi \(2015\)](#) Section 2.4.

Upper/lower tail dependence. Considering the random vector $\mathbf{X} = (X_i, X_j)$ and the copula C underlying their joint distribution. The *upper/lower tail dependence* coefficients are defined as:

$$\lambda_U(X_i, X_j) = \lim_{\substack{u \rightarrow 1 \\ u < 1}} \mathbb{P}\left(X_i > F_{X_i}^{-1}(u) | X_j > F_{X_j}^{-1}(u)\right) = \lim_{\substack{u \rightarrow 1 \\ u < 1}} \left(2 - \frac{1 - C(u, u)}{1 - u}\right) \quad (3.8a)$$

$$\lambda_L(X_i, X_j) = \lim_{\substack{u \rightarrow 0 \\ u > 0}} \mathbb{P}\left(X_i \leq F_{X_i}^{-1}(u) | X_j \leq F_{X_j}^{-1}(u)\right) = \lim_{\substack{u \rightarrow 0 \\ u > 0}} \left(\frac{C(u, u)}{1 - u}\right) \quad (3.8b)$$

[Joe \(2014\)](#) further discusses asymptotic limit and outlines the particular case of the bivariate Gaussian copula, for which the tail dependence measures are null, $\lambda_U = \lambda_L = 0$. Note that Kendall's tau and the tail dependence coefficients both have their associated plots, allowing to compare the dependence of two distributions [\[add ref\]](#).

3.2.2 Empirical and checkerboard copula

The *empirical copula* was introduced by [Deheuvels \(1979\)](#), as an estimator of the copula C associated with the random vector \mathbf{X} . Since the normalized ranks are a creasing mapping that present uniform marginals by construction, they are a natural empirical representation of the density copula. Considering a sample $\mathbf{X}_n = \{\mathbf{x}^{(1)}, \dots, \mathbf{x}^{(n)}\} \sim \mathbf{X}$ with the respective ranks $\mathbf{R}_n = \{\mathbf{r}^{(1)}, \dots, \mathbf{r}^{(n)}\}$, a definition of the empirical copula is:

$$C_n(u_1, \dots, u_d) = \frac{1}{n} \sum_{i=1}^n \prod_{j=1}^d \mathbb{1} \left\{ \frac{r_j^{(i)}}{n} \leq u_j \right\}, \quad \mathbf{u} = (u_1, \dots, u_d) \in [0, 1]^d \quad (3.9)$$

Even if this function converges uniformly towards the copula C (according to the Glivenko-Cantelli theorem), it does not fulfill the conditions to be a copula (see e.g., [González-Barrios and Hoyos-Argüelles 2021](#)).

In this context, different methods may be applied to smooth the empirical copula into a genuine copula. This problem can be perceived as a functional approximation of the underlying copula C , which is unique for continuous variables (according to Sklar's Theorem 1). Let us consider a discretization of the unit hypercube as a grid:

$$G = \left\{ \frac{0}{m_1}, \dots, \frac{m_1}{m_1} \right\} \times \cdots \times \left\{ \frac{0}{m_d}, \dots, \frac{m_d}{m_d} \right\}, \quad \mathbf{m} = (m_1, \dots, m_d) \in \mathbb{N}^d. \quad (3.10)$$

The *checkerboard copula* is a simple approximation of the empirical copula using the discretization G . This method is comparable to a multivariate histogram of the empirical density copula c_n (see the formal multivariate definition proposed by [Cottin and Pfeifer 2014](#)). In the particular case for which $m_j = m, \forall j \in \{1, \dots, d\}$, the checkerboard copula is called the “rook” copula, and expressed by [Segers et al. \(2017\)](#) as:

$$C_n^{\#m}(u_1, \dots, u_d) = \frac{1}{n} \sum_{i=1}^n \prod_{j=1}^d \min \left(\max(nu_j - r_j^{(i)} + 1, 0), 1 \right). \quad (3.11)$$

This empirical copula has a low complexity (see [Rose 2015](#)) and efficient results for large samples ([González-Barrios and Hoyos-Argüelles, 2021](#)), however, its variance is comparable to the empirical copula for small-sized samples ([Segers et al., 2017](#)). It is proven to be a genuine copula and its asymptotic behavior was studied by various authors such as [Li et al. \(1998\)](#); [Genest et al. \(2017\)](#). In the following, an approximation of the empirical copula with Bernstein polynomials is presented.

3.2.3 Empirical Bernstein and Beta copula

A few elements on Bernstein polynomials and their corresponding approximation is reminded before introducing the empirical Bernstein copula.

Bernstein polynomials and approximation

Let us first define the *Bernstein basis polynomial* of order $m \in \mathbb{N}$ as:

$$b_{m,t}(u) = \binom{m}{t} u^t (1-u)^{m-t}, \quad t \in \{0, \dots, m\}. \quad (3.12)$$

These polynomials present various interesting properties, such as their nonnegativity over $[0, 1]$, being bounded by one, and offering a partition of unity on $[0, 1]$ ([Lasserre, 2023](#)):

$$1 = \sum_{t=0}^n b_{m,t}(u)(x), \quad \forall x \in \mathbb{R}, \quad \forall n \in \mathbb{N}. \quad (3.13)$$

Bernstein's polynomials allow us to uniformly approximate any continuous and real-valued function defined on a compact set $f : [0, 1]^d \mapsto \mathbb{R}$ (as they were used to demonstrate the Weierstrass approximation theorem). In the multivariate case, the *Bernstein approximation* of the function f can be written on a grid over the unit hypercube $G = \left\{ \frac{0}{m_1}, \dots, \frac{m_1}{m_1} \right\} \times \dots \times \left\{ \frac{0}{m_d}, \dots, \frac{m_d}{m_d} \right\}$, $\mathbf{m} = (m_1, \dots, m_d) \in \mathbb{N}^d$, as:

$$B_{\mathbf{m}}(f)(\mathbf{u}) = \sum_{t_1=0}^{m_1} \dots \sum_{t_d=0}^{m_d} f\left(\frac{t_1}{m_1}, \dots, \frac{t_d}{m_d}\right) \prod_{j=1}^d b_{m_j, t_j}(u_j), \quad \mathbf{u} = (u_1, \dots, u_d) \in [0, 1]^d. \quad (3.14)$$

The Bernstein polynomials approximate f such that $\lim_{m \rightarrow \infty} B_m(f) = f$ uniformly on $[0, 1]$.

Bernstein polynomials for copula approximation

Copulas are continuous and bounded functions defined on a compact set (the unit hypercube). Therefore, they are good candidates to be approximated by Bernstein polynomials. The Bernstein approximation applied on an empirical copula C_n was introduced as *empirical Bernstein copula* (EBC) by [Sancetta and Satchell \(2004\)](#) for applications in economics and risk management:

$$B_{\mathbf{m}}(C_n)(\mathbf{u}) = \sum_{t_1=0}^{m_1} \dots \sum_{t_d=0}^{m_d} C_n\left(\frac{t_1}{m_1}, \dots, \frac{t_d}{m_d}\right) \prod_{j=1}^d b_{m_j, t_j}(u_j), \quad \mathbf{u} = (u_1, \dots, u_d) \in [0, 1]^d. \quad (3.15)$$

In this expression, the evaluations of the empirical copula on the vertices of the grid are smoothed by the product of Bernstein polynomials. A respective approximation of the copula density can be directly expressed by deriving the previous formula. The EBC delivers a genuine copula, if and only if all the polynomial degrees $\{m_j\}_{j=1}^d$ are divisors of n (see [Segers et al. 2017](#), Proposition 2.5).

In the particular case of regular grids, $\{m_j = m\}_{j=1}^d$, the EBC can be expressed as a mixture of beta distributions ([Segers et al., 2017](#)). Let us consider an n -sized rank sample, $\mathbf{R} = (\mathbf{r}_1, \dots, \mathbf{r}_d) \in \mathbb{N}^n$, and the degree m taken as divisor of n . Note that the r^{th} order statistic of an n -sized sample following a uniform $[0, 1]$ is distributed according to the beta distribution $\mathcal{B}(r, n - r + 1)$.

Considering these hypotheses, the EBC can be written as:

$$B_m(C_n)(\mathbf{u}) = \frac{1}{n} \sum_{i=1}^n \prod_{j=1}^d F_{m,r_j^{(i)}}, \quad \mathbf{u} = (u_1, \dots, u_d) \in [0, 1]^d, \quad (3.16)$$

where $F_{m,r}$ is the CDF of the beta distribution $\mathcal{B}(r, m-r+1)$ (also called the “regularized incomplete beta function”):

$$F_{m,r} = \sum_{t=r}^m \binom{m}{t} u^t (1-u)^{m-t}, \quad u \in [0, 1], \quad r \in \{1, \dots, m\}. \quad (3.17)$$

Overall, the EBC is a very versatile tool which able to approximate complex dependence patterns. Moreover, Monte Carlo sampling on an EBC is straightforward and licit since it is a genuine copula. As a drawback, the estimation accuracy of this nonparametric method heavily relies on the polynomial order tuning.

Asymptotic behavior of the empirical Bernstein copula

In practice, the choice of polynomial degree for an EBC leads to a challenging bias-variance tradeoff. For example, the particular case of $\{m = n\}$, introduced as the *empirical Beta copula* by Segers et al. (2017), tends to reduce the bias while increasing the variance. In this paper, the beta copula presents interesting results compared to the Bernstein or the checkerboard copula for small sample sizes (i.e., $n < 100$). Theoretically, the tuning of the degree was first optimized to minimize an “Asymptotic Mean Integrated Squared Error” (AMISE) of $B_m(C_n)$:

$$\text{AMISE}(B_m(C_n)) = \mathbb{E}[\|B_m(C_n) - C\|_2^2] = \mathbb{E}\left[\int_{\mathbb{R}^d} (B_m(C_n)(\mathbf{u}) - C(\mathbf{u})) d\mathbf{u}\right]^2. \quad (3.18)$$

The seminal work of Sancetta and Satchell (2004) proves in Theorem 3 that:

- $B_m(C_n)(\mathbf{u}) \rightarrow C(\mathbf{u})$ for any $u_j \in]0, 1[$ if $\frac{m^{d/2}}{n} \rightarrow 0$, when $m, n \rightarrow \infty$.
- The optimal polynomial order in terms of AMISE is¹: $m \lesssim m_{\text{AIMSE}} = n^{2/(d+4)}$, $\forall u_j \in]0, 1[$.

To illustrate the previous theorem, Fig. 3.1 represents the evolution of the m_{AMISE} for different dimensions and sample sizes (adapted from Lasserre 2022). In medium dimension, the values of m_{IMSE} tend towards one, which is equivalent to the independent copula. Therefore, high-dimensional problems should rather be divided into a product of smaller problems on which the EBC is tractable.

The polynomial order for EBC estimation is still a bottleneck which was studied over the years by different authors (see e.g., Janssen et al. 2012; Bouezmarni et al. 2013; Rose 2015; Segers et al. 2017). Meanwhile, other nonparametric approaches such as the “penalized Bernstein” and the “penalized B-spline” estimators were compared to the EBC and vine copulas in a

¹The sign \lesssim stands for “less than or approximately”.

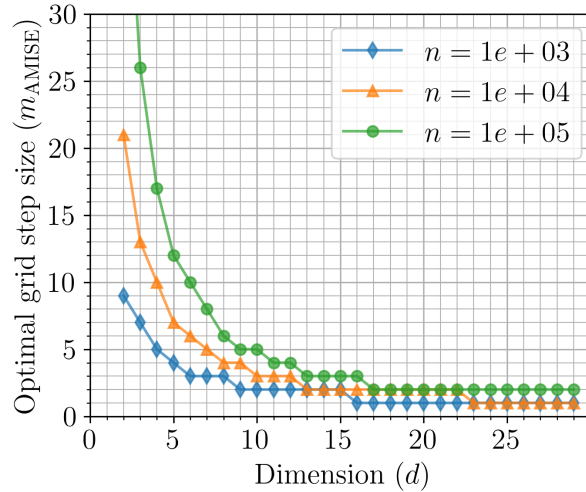


Figure 3.1 Evolution of m_{IMSE} for different dimensions and sample sizes.

benchmark realized by Nagler et al. (2017). The results showed that the most performant methods vary depending on the problem studied (for different dimension, sample sizes, strength of dependence). Regarding tail dependence modeling, nonparametric approaches are generally limited, but recent contributions introduced Bootstrap procedures to better this aspect (Kiriliouk et al., 2021).

Illustrative example on a Clayton copula

Let us consider a bivariate Clayton copula C with parameter $\theta = 2.5$ (see Nelsen 2006) A Monte Carlo sample with size $n = 10$ is generated on it, which is then used to build an empirical copula C_n as defined in Eq. (3.9). Fig. 3.2 (a) illustrates the empirical copula corresponding to the sample, with the shade of grey matching the CDF values. Then, the Bernstein approximation of the empirical copula (i.e., the EBC) is represented in Fig. 3.2 (b), (c), (d) according to the Eq. (3.15). The three versions of the EBC correspond to different polynomial orders, assuming that ($m_1 = m_2$).

As the order increases, the bias between the EBC and the copula C tends to be reduced. Note that the second EBC in Fig. 3.2 (c) where ($m_1 = m_2 = n$) is equivalent to the Beta copula. Moreover, increasing the order beyond the sample size definitely overfits of the copula.

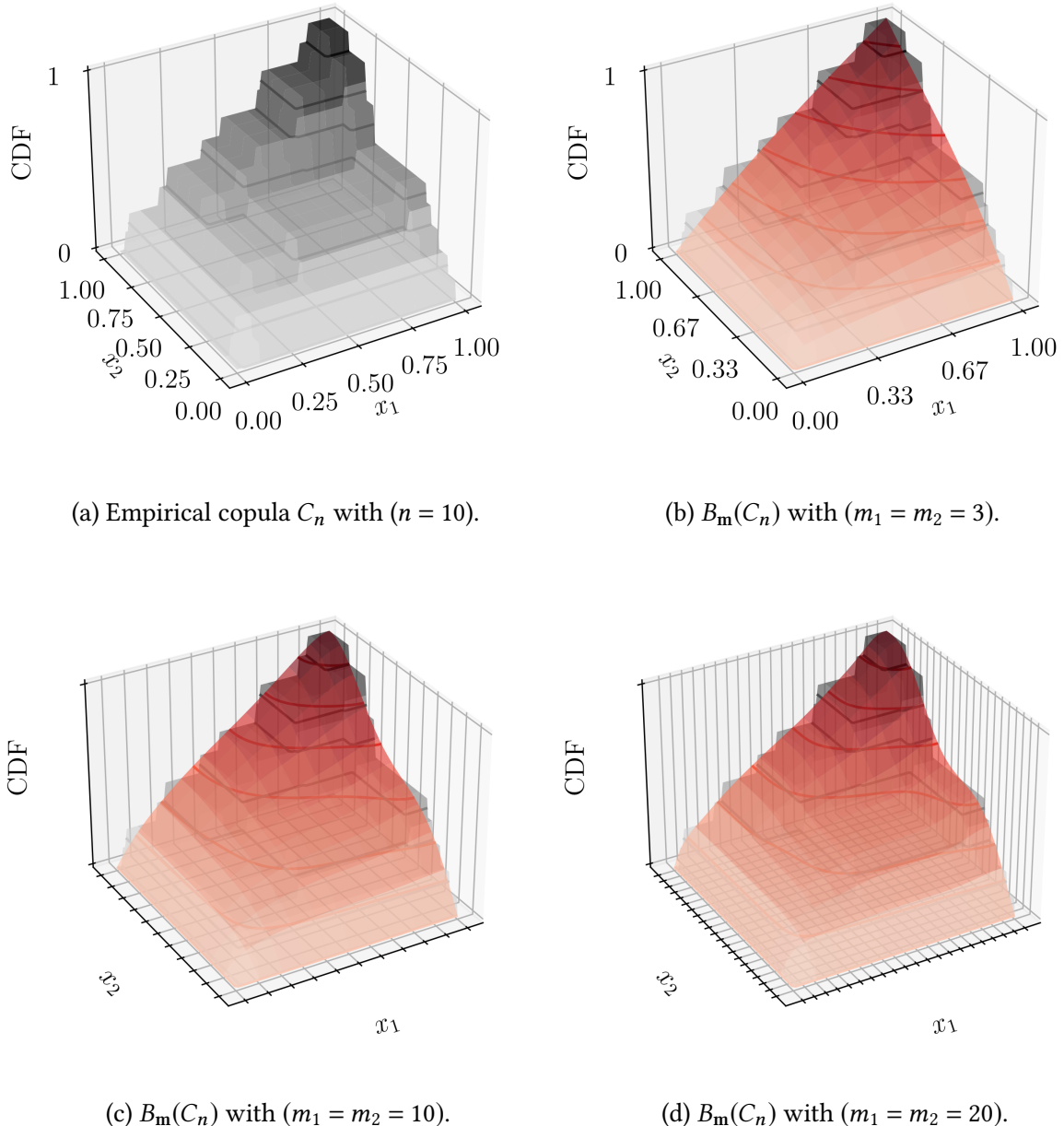


Figure 3.2 Bernstein approximations of the empirical copula C_n (with size $n = 10$) of a Clayton copula (with parameter $\theta = 2.5$). The polynomial orders are assumed equal in the two dimensions $m_1 = m_2 \in \{3, 10, 20\}$.

3.3 *Copulogram*: a tool for multivariate data visualization

In statistics, data visualization offers a wide set of tools to analyze data. Multivariate data visualization is of great help to apprehend problems with dimension higher than two. In the context of continuous variables, let us consider the n -sized sample $\mathbf{X}_n = \{\mathbf{x}^{(1)}, \dots, \mathbf{x}^{(n)}\} \sim \mathbf{X} \in \mathcal{D}_{\mathbf{x}} \subseteq \mathbb{R}^d$. The marginal samples of \mathbf{X}_n are denoted by $X_{n,j} = \{x_j^{(1)}, \dots, x_j^{(n)}\}, j \in \{1, \dots, d\}$.

Various techniques exist to represent multivariate data, such as the “parallel coordinate plot”, also called “cobweb plot” (see e.g., (Heinrich and Weiskopf, 2013)). For each sample $\mathbf{x}^{(i)} \in \mathbf{X}_n$, this plot draws a line passing by the values of $\mathbf{x}^{(i)} = [x_1^{(i)}, \dots, x_d^{(i)}]$. This representation was used in sensitivity analysis to illustrate the connections between a set of inputs and an output, however, it does not provide a good representation of the dependence structure between the inputs.

3.3.1 From pairwise plot to copulogram

Alternatively, the “pairwise plot”, also named “generalized draftsman plot”, was initially introduced by Hartigan (1975) to draw a matrix of scatter-plots between all the pairs of marginal samples $\{X_{n,i}, X_{n,j}\}, i \neq j \in \{1, \dots, d\}$ ². Because of the symmetry, the pairwise plot is usually represented on the lower triangle of the matrix. Later on, statisticians improved the pairwise plot by adding a histogram (or KDE) of the marginal samples $X_{n,j}, j \in \{1, \dots, d\}$ on the diagonal. Additionally, the upper triangle was completed with the values of linear correlation for each pairs of marginal sample $\{X_{n,i}, X_{n,j}\}, i \neq j$. This matrix of correlation coefficients is also known as “correlogram”. Altogether, this matrix plot became known as the “scatter plot of matrices” (SPLOM).

However, the linear correlation coefficient is known to give a poor description of the dependence in nonlinear cases. When analyzing a continuous sample $\mathbf{X}_n \sim \mathbf{X}$, the Sklar theorem states that the dependence structure within the random vector \mathbf{X} has a unique expression with its d -copula C . As mentioned in Section 3.2.1, the component wise normalized ranks of the original sample \mathbf{X}_n define the empirical copula density c_n (converging towards C as n increases).

To the best of our knowledge, the *copulogram* is a new multivariate data visualization tool improving the SPLOM by representing the empirical copula density c_n on the upper triangle of the matrix plot. This plot is an empirical decomposition of a multivariate sample in the vein of the Sklar theorem between marginals on the diagonal and copula on the upper triangle.

3.3.2 Implementation in a Python package

An open-source implementation is proposed in the python package `copulogram`. This code mostly relies on the Python package for data visualization `seaborn` (Waskom, 2021). The developments are tracked and archived in a GitHub repository² and the package can be installed from the package-management system “PyPI”.

Multiple visual options are offered by the `copulogram` package, as illustrated in the GitHub repository. For example, the user can represent the univariate samples on the diagonal, or the bivariate samples in the triangles with kernel density estimation. Categorical variables can be used to assign different colors depending on the data class. The colors can also vary depending on a continuous variable after defining a mapping between the values of this variable and a set of color (also called colorbar).

Example #1: Iris flower dataset

The first example illustrates the copulogram on a widely used dataset in the machine learning community. The iris flower dataset was first introduced by Fisher and became a reference dataset for classification techniques. In the following lines of Python code, the dataset is loaded and the `copulogram` package is used to draw the new plot. The resulting copulogram applied to the iris flower data is represented in Fig. 3.3.

```

1  #!/usr/bin/python3
2  import seaborn as sns
3  import copulogram as cp
4  data = sns.load_dataset("iris")
5  copulogram = cp.Copulogram(data)
6  copulogram.draw(hue="species")
```

Since this data mostly presents linear dependencies, the copulogram is not very instructive. In other cases, the role of the dependence in the joint distribution is more important.

Example #2: Ishigami function

The Ishigami function is commonly used as a benchmark problem for global sensitivity analysis (GSA):

$$y = g(x_1, x_2, x_3) = \sin(x_1) + 7 \sin(x_2)^2 + 0.1 x_3^4 * \sin(x_1). \quad (3.19)$$

This uncertainty quantification problem considers an independent random input vector $\mathbf{X} = \prod_{j=1}^3 X_j$. While the marginals in GSA benchmarks are usually assumed to be uniform, they will be considered Gaussian hereafter to distinguish the different elements of the joint distribution. Therefore, let us define $X_j \sim \mathcal{N}(0, 1) \forall j \in \{1, 2, 3\}$. In this setup, the random inputs are independent but they each present interesting dependencies with the random output $Y = g(\mathbf{X})$.

A Monte Carlo sample with size $n = 10^3$ is generated, $\mathbf{X}_n \stackrel{\text{i.i.d.}}{\sim} \mathbf{X}$, and evaluated such that $Y_n = g(\mathbf{x}_n)$. The copulogram of the input-output sample (\mathbf{X}_n, Y_n) is represented in Fig. 3.4. As expected, the scatter-plots between the inputs in the upper triangle are uniform (representing an independent density copula).

In GSA, the work of Póczos et al. (2012) studied the discrepancy between the empirical density copula $c_n(X_j, Y), j \in \{1, \dots, d\}$ and the independent copula to qualitatively assess the importance of X_j . In the same vein, the paper of Plischke and Borgonovo (2019) attempted to formalize a link between different GSA approaches based on copulas and to quantitative approaches as the Sobol' indices.

²GitHub repository: <https://github.com/efekhari27/copulogram>

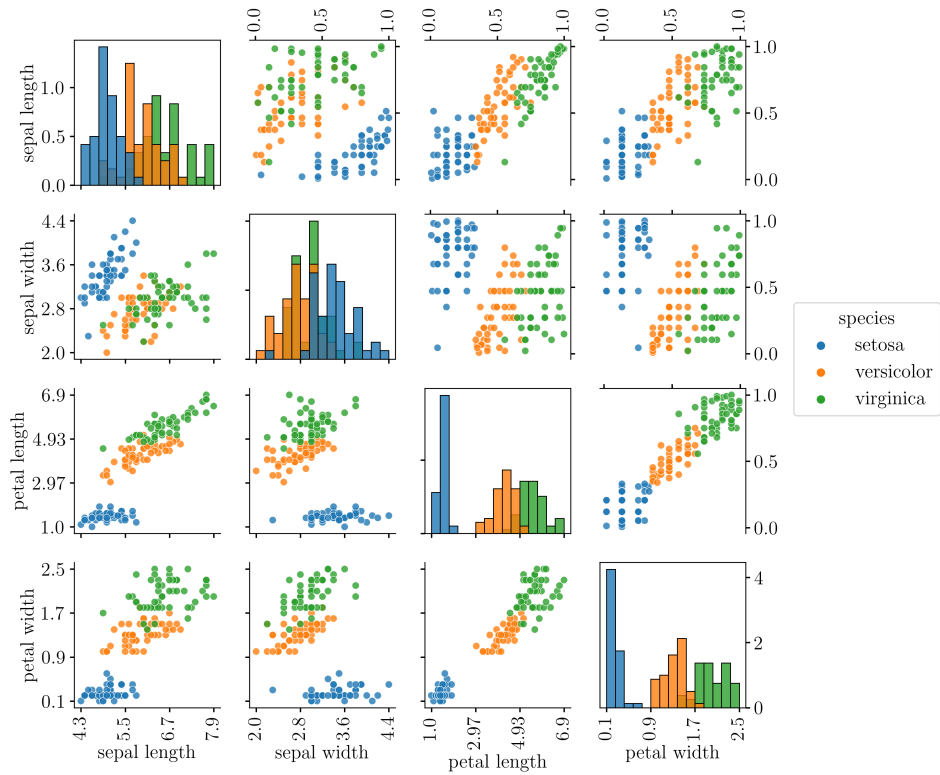


Figure 3.3 Copulogram of the iris flower dataset with colors assigned by the iris species.

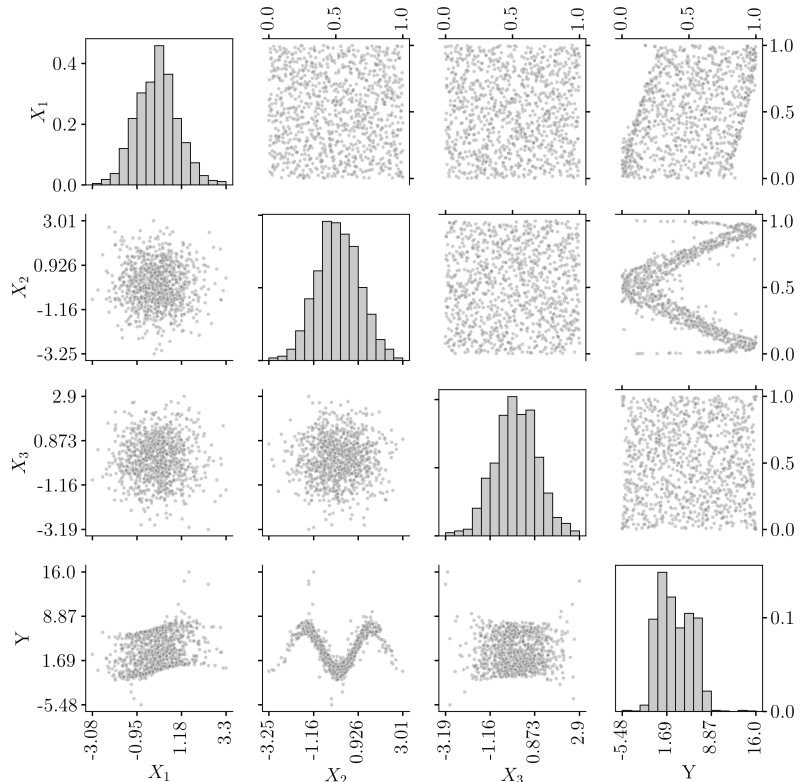


Figure 3.4 Copulogram of Monte Carlo sample (with size $n = 10^3$) of the inputs and outputs of the modified Ishigami problem.

3.4 Semiparametric inference of the South Brittany metocean conditions

Metocean conditions have been long studied in costal and offshore engineering. Inferring multivariate probabilistic models on metocean data became essential in wind energy.

Numerous approaches are proposed in the literature to fit a model on environmental data. Among them, let us mention the use of parametric methods as the conditional modeling (e.g., Bitner-Gregersen 2015; Vanem et al. 2023), or the construction of vine copulas (e.g., Vanem 2016; Montes-Iturriaga and Heredia-Zavoni 2016; Lin and Dong 2019,?). Nonparametric methods as the KDE were also applied in this context (e.g., Han et al. 2018). The nonparametric techniques generally struggle to model the distributions' tails, even if the tails are essential to qualify structures for ultimate events. However, they are highly flexible and often easier to implement than parametric methods.

In this section, a semiparametric inference strategy is presented, composing some well-known parametric models for the marginals (e.g., Weibull distribution for the wind speed), with a highly flexible dependence modeling by the EBC. A metocean dataset is used to showcase the empirical Bernstein copula and its representation by the copulogram. This dataset from the ANEMOC (Digital Atlas of Ocean and Coastal Sea States atlas, Raoult et al., 2018) gathers 32 years of preprocessed data (at an hourly resolution) from a location off the coast of South Brittany, France. A subset of 10^4 points is randomly selected among the ANEMOC data, which will be used to realize the semiparametric inference.

3.4.1 Inference of the marginals

The variables studied to describe the environmental conditions match the ones defined in Table 2.2. Unfortunately, the turbulence is provided by the ANEMOC database and is therefore not fitted. A straightforward inference is performed on the data, resulting in the models presented in Table 3.1. The wind and wave directions are fitted by KDE to catch their multimodal behavior while the other variables by MLE on various parametric models. Note that some variations of KDE with kernels specific to circular data could be interesting to ensure the continuity of the model at the bounds (Bai et al., 1989).

The results of the marginals' inferences, plotted in Fig. 3.5 against histograms, are visually satisfying. Statistical testing is not necessary in our case since the actual topic of discussion is related to the inference of the dependence. Considering these marginals, a study of the copula inference can be developed.

3.4.2 Nonparametric inference of the dependence

3.4.3 Goodness-of-fit and discussion

[When should we use nonparametric copula inference?]

Name	Notation	Fitted model
Wind speed	U	Weibull ($\beta = 11.4, \alpha = 2.2, \gamma = 0$)
Wind direction	θ_{wind}	KDE
Significant wave height	H_s	Weibull ($\beta = 2.1, \alpha = 1.5, \gamma = 0.5$)
Wave period	T_p	Inverse Normal ($\mu = 8, \lambda = 140$)
Wave direction	θ_{wave}	KDE

Table 3.1 Marginal inference results of the South Brittany metocean data.

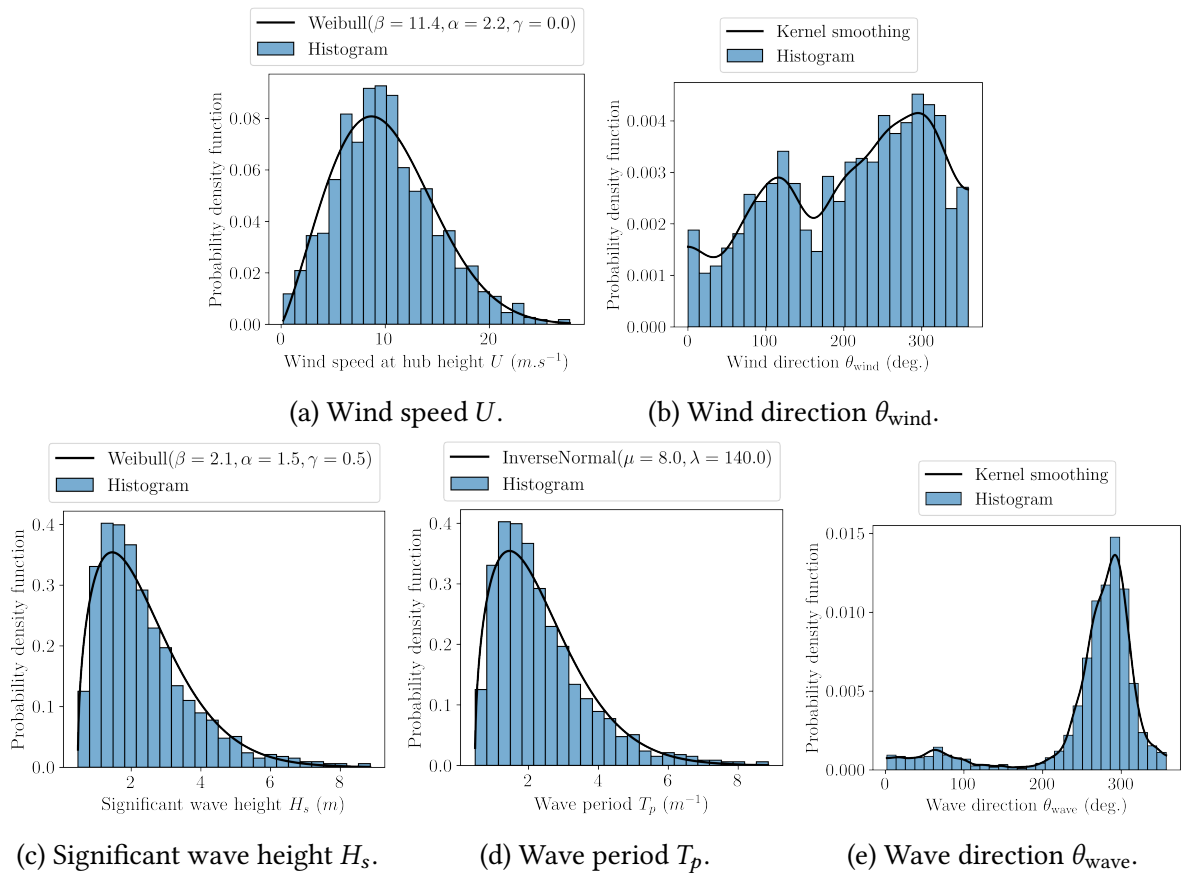


Figure 3.5 Marginal inference results of the South Brittany metocean data.

[Joe \(2014\)](#), p.250 discusses the use of nonparametric methods for multivariate inference. According to the author,

“Non-parametric estimation of a copula is desirable if univariate margins are well-behaved and can be fit with parametric families, and the multivariate dependence structure is more complex than monotone relations among variables. If the univariate margins are also not simple, then multivariate non-parametric estimation approaches can be applied to the multivariate distribution directly, rather than estimation of non-parametric univariate margins with a non-parametric copula. ”

3.5 Quantifying and clustering the wake-induced perturbations within a wind farm

[add ref: “Difference in load predictions obtained with effective turbulence vs. a dynamic wake meandering modeling approach”]

In the offshore wind industry, the wake effect is considered crucial for electricity production and structural fatigue of turbine components. For instance, the standards developed by the International Electrotechnical Commission (see appendix E in ?) review some analytical ?, and numerical models (e.g., the dynamic wake meandering approach by ?) to simulate the wind speed deficit and the wake added turbulence. Since the pioneering work of ?, several wake models were developed and compared in a benchmark by ?. This work takes advantage of the low computational cost of steady-state wake models to propagate the uncertainty from ambient to wake-induced wind conditions seen on a farm. It is worth noting that the wake creates a heterogeneous wind field in a wind farm, resulting in different loading conditions which should be considered at the stage of reliability based design (RBD). Such heterogeneity is not taken into account by the design load cases of international standards (see e.g., ??) where wind and wave conditions are derived from scenarios occurring over long-term periods. Wake models allow us to simulate the wind conditions’ distribution at each turbine, however, the RBD step is too costly to be performed for each turbine. For further details regarding the RBD, one may refer to the work of [Huchet \(2019\)](#); [Slot et al. \(2020\)](#); [Stieng and Muskulus \(2020\)](#); [Wilkie and Galasso \(2021\)](#), proposing several approaches to reduce the computational cost of this step. In order to speed up the RBD at the scale of a wind farm, the present work aims at building clusters of WT similarly affected by the wake. Then, the RBD over a wind farm can be computed only on a few WT, each representing a cluster of turbines enduring similar wake-modified wind loading. This clustering is done on two wind parameters, following the conclusions of the global sensitivity analysis of ?. In order to discriminate the wake-perturbed distributions of wind parameters, the maximum mean discrepancy (MMD) is used as a statistical metric between multivariate distributions (as reviewed by ?). To illustrate this novel approach, a theoretical wind farm for the ongoing tenders off the coast of South Brittany in France is studied, with a modified version of the floating offshore wind turbine (FOWT) IEA-15MW (initially proposed in ??). Figure 3.6 illustrates the layout of the 25 FOWT considered in the following. This layout is regular with an inter-turbine distance of seven times the rotor diameter in the dominant wind direction and five times the rotor diameter in the orthogonal (crosswind) direction. More details regarding the FOWT modifications and theoretical wind farm can be found in ??.

Based on the results of previous numerical studies, with either dynamic wake meandering ? or LES ?, we retain the time-averaged floater position (translation and rotation) as the main effect of the floater motion on the far wake. It was shown that this effect is small, both on the wake-added turbulence and on the wind speed deficit. However, noticeable uplift of the wake may influence the fatigue design.

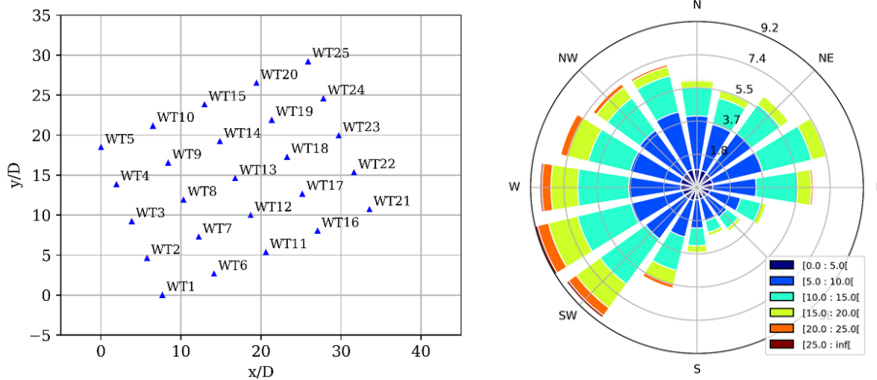


Figure 3.6 South Brittany wind farm layout (left). South Brittany wind rose from the ANEMOC data (right, source: ?).

The key idea in this paper to reduce the number of cases for RBD is to employ clustering techniques on the wake-induced wind parameters, to constitute groups of WT that are exposed to similar design load conditions. To do so, the present work is divided into four sections. First, the wake model used in this work is presented in section ???. Then, section 3.5.1 describes the uncertainty propagation through the wake model, from the probabilistic distribution of ambient wind parameters to the wake-modified wind parameters distribution within the farm. In order to regroup the similar wake-modified distributions, an adapted statistical metric on multivariate distributions is introduced in section 3.5.2. Finally, the application of several clustering methods to the South Brittany case study is compared in section ???. The main conclusion suggests four clusters among the 25 FOWT which can then be used for RBD analysis of the farm.

3.5.1 Uncertainty propagation in a wake model

The wake model described in section ?? takes as input a set of variables describing the ambient wind conditions $\mathbf{x} \in \mathbb{R}^3$ and computes the perturbed wind conditions at each WT represented by the vector $\mathbf{x}'_l, l \in (1, \dots, n_{WT})$, where n_{WT} is the total number of turbines in the farm:

$$g : \mathbb{R}^3 \rightarrow \mathbb{R}^{3n_{WT}} \quad (3.20)$$

$$\mathbf{x} \longmapsto g(\mathbf{x}) = (\mathbf{x}'_1, \dots, \mathbf{x}'_{n_{WT}}) \quad (3.21)$$

The uncertainties associated with the ambient wind conditions are represented by a random vector \mathbf{X} following the distribution p_0 . Note that the index 0 is a reference to the fact that these conditions are not perturbed by the wake. A parametric model has been fitted in Vanem et al. (2023) using conditional probability density functions to capture the dependence structure, with an approach similar to the one presented in Kelly and Vanem (2022). The random vector \mathbf{X} is described by the following input random variables:

- Mean wind speed (u) is the 10-min average horizontal wind speed at hub height.

- Wind turbulence intensity (TI) is the 10-min wind speed turbulence intensity at hub height.
- Wind direction (θ) is the 10-min average wind direction.

In the following, we assume the wind orientation variable θ to be unaffected by the wake. When perturbed by the wake of the wind farm, the WT l sees a wind flow represented by the random vector $\mathbf{X}'_l, l \in (1, \dots, n_{WT})$, following the distribution p'_l . Then, the two remaining parameters are u_{rotor} and TI_{rotor} to represent this modified wind flow on a vertical plane located at each WT. These two quantities of interest are averaged over the rotor while the input parameters are given at hub height. For the sake of simplicity, we will neglect this difference in what follows in order to consider the transformation $\mathbf{X}' = g(\mathbf{X})$ as a simple perturbation of \mathbf{X} . We will abusively denote u and TI both the input and output quantities. The output of the uncertainty propagation is a set of perturbed environmental distributions $p'_l, l \in (1, \dots, n_{WT})$. A Monte-Carlo sample $\mathbf{X}_n = \mathbf{x}^{(1)}, \dots, \mathbf{x}^{(n)}$ of the three random input variables is generated. Then, considering the farm layout illustrated in Figure 3.6 and a constant wind shear exponent of 0.1 like in section ??, a wake simulation is run for every wind condition of the Monte Carlo design of experiments. The code output consists in a multivariate joint distribution of modified u and TI for each WT. As the Monte Carlo procedure is known to converge slowly but surely, it was chosen to perform this uncertainty propagation with a number of simulations of size $n = 6\,000$ because of its simplicity and the low computational cost of the simulations.

We can plot a preview of the wake perturbations on the joint distribution for given WT in the two dimensions u and TI . Figure 3.7 illustrates this perturbation for three WT differently affected by the wake depending on their position in the farm (cf. Figure 3.6). One can notice that the WT 25 distribution (in orange) is very close to the ambient distribution (in black), as expected, this WT being located on the edge of the farm and facing the dominant wind direction. Meanwhile, the WT 13 distribution (in red) seems more affected by the wake, by getting a higher wind turbulence with lower wind speed. This analysis can be completed with the two marginals in Figure 3.8 and Figure 3.9, both describing the ambient marginal distributions (in black) and wake-disturbed distributions. In general, a small wind speed deficit is noticed as indicated by the small shifts of the probability density functions to the left on Figure 3.8. Also, a small added turbulence is indicated by the small shifts of the curves to the right on Figure 3.9. Ideally, a tool should allow us to quantify the perturbation between the ambient and perturbed distributions.

3.5.2 Statistical metric of wake-induced perturbations

Maximum mean discrepancy: a distance between distributions In the literature, the maximum mean discrepancy was introduced by [Gretton et al. \(2006\)](#) as a statistical test to discriminate two distinct distributions. After further work on this tool, authors such as [Sriperumbudur et al. \(2010\)](#) showed that the MMD is a distance between two distributions embedded in a specific function space. Therefore, this concept relies on the embedding of distributions

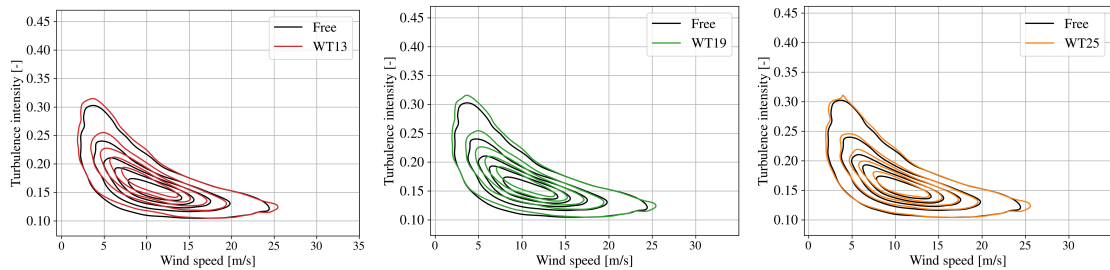


Figure 3.7 Joint perturbation at WT 13, 19, and 25

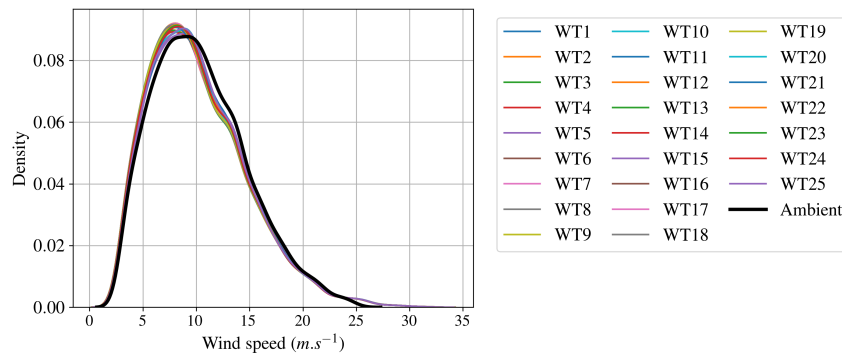


Figure 3.8 Ambient and wake-disturbed distributions of the wind speed

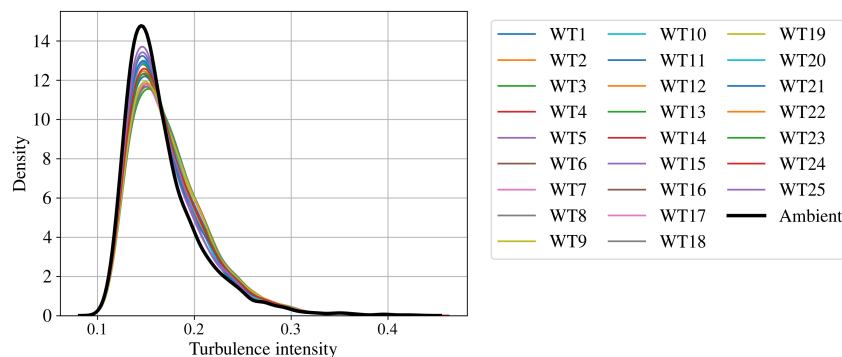


Figure 3.9 Ambient and wake-disturbed distributions of the turbulence intensity

in a convenient Hilbert space. Considering a positive-definite kernel $k : \mathbb{R}^d \times \mathbb{R}^d \rightarrow \mathbb{R}, d \in \mathbb{N}$ generating a unique Hilbert space \mathcal{H}_k of functions equipped with inner products $\langle \cdot, \cdot \rangle_{\mathcal{H}_k}$ and norms $\|\cdot\|_{\mathcal{H}_k}$ (also called Reproducing Kernel Hilbert Space (RKHS) when the function $k(\mathbf{x}, \cdot)$ satisfies the reproducing property). Then, let us define the kernel mean embedding of the distribution P in the function space \mathcal{H}_k :

$$\mu_P(\mathbf{x}) := \int_{\mathbb{R}^d} k(\mathbf{x}, \mathbf{y}) dP(\mathbf{y}) \approx \frac{1}{n} \sum_{i=1}^n k(\mathbf{x}, \mathbf{x}^{(i)}), \mathbf{x}^{(i)} \in \mathbf{X}_n. \quad (3.22)$$

The kernel mean embedding is approximated on sample $\mathbf{X}_n = (\mathbf{x}^{(1)}, \dots, \mathbf{x}^{(n)})$ following the distribution P . Figure 3.10 illustrates the kernel mean embedding of two distributions in the function space \mathcal{H}_k defined previously. Notice that this procedure allows us to embed continuous distributions (such as P) as well as discrete distributions (such as Q).

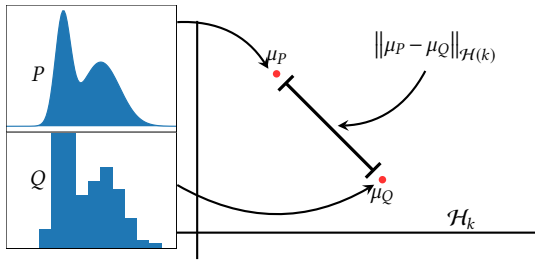


Figure 3.10 Kernel mean embedding of two probability distributions P and Q mapped in the RKHS H_k

The distance between the two kernel mean embeddings μ_P and μ_Q is called the maximum mean discrepancy (MMD). This distance between two distributions P and Q is initially defined by the worst-case error for any function within a unit ball of a Hilbert space \mathcal{H}_k , generated by the kernel k :

$$\text{MMD}_k(P, Q) := \sup_{\|g\|_{\mathcal{H}_k} \leq 1} \left| \int_{\mathbb{R}^d} g(\mathbf{x}) dP(\mathbf{x}) - \int_{\mathbb{R}^d} g(\mathbf{x}) dQ(\mathbf{x}) \right| = \|\mu_P(\mathbf{x}) - \mu_Q(\mathbf{x})\|_{\mathcal{H}_k}. \quad (3.23)$$

The MMD fully relies on the difference of kernel mean embeddings. Moreover, according to Sriperumbudur et al. (2010), a kernel is called “characteristic kernel” when the following equivalence is true, $\text{MMD}_k(P, Q) = 0 \iff P = Q$, making the MMD a metric on \mathbb{R}^d . For its good convergence behavior, the squared MMD has been used for multiple other purposes than numerical integration: statistical testing Gretton et al. (2006), sensitivity analysis Da Veiga (2015). When elevated to the square, it can be estimated using one n -sized representative sample of P denoted $\{\mathbf{x}^{(i)}\}_{i \in (1, \dots, n)}$ (and respectively one m -sized sample of Q denoted $\{\mathbf{y}^{(i)}\}_{i \in (1, \dots, m)}$:

$$\widehat{\text{MMD}}_k(P, Q)^2 = \frac{1}{n^2} \sum_{i,j=1}^n k(\mathbf{x}^{(i)}, \mathbf{x}^{(j)}) - \frac{2}{nm} \sum_{i=1}^n \sum_{j=1}^m k(\mathbf{x}^{(i)}, \mathbf{y}^{(j)}) + \frac{1}{m^2} \sum_{i,j=1}^m k(\mathbf{y}^{(i)}, \mathbf{y}^{(j)}). \quad (3.24)$$

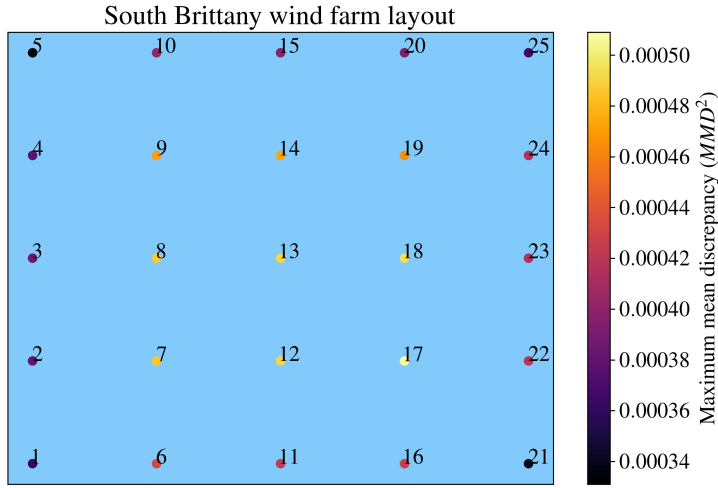


Figure 3.11 South Brittany layout and wake effects measured by the squared MMD on wind conditions. Note that the vertical direction on this plot does not represent the north direction.

In the following, the idea is to compare the ambient wind distribution p_0 to the wake-perturbed wind conditions p'_l at the WT l using the previously defined squared MMD.

Application to the South Brittany wind farm project Once the joint perturbed distributions of each WT are estimated by a large Monte Carlo sample (cf. section 3.5.1), the MMD with the ambient wind conditions can be computed. Figure 3.11 illustrates for each WT the squared MMD value computed to measure the wake-induced perturbation. Let us remind that MMD is a distance between the joint perturbed distribution at a WT computed for all wind orientations with the ambient wind distribution. Despite the wake obviously depend on the wind direction, our final goal is to define a small number of WT for RBD thus independently of the wind orientation. The lower this metric gets, the closer to the ambient wind distribution. Quite logically, the WT in the center of the farm are more affected by the wake since they are subject to the wake regardless of the wind direction.

The values of squared MMD given in the previous figure are estimated between two samples:

- the Monte Carlo sample of the free environmental distribution: \mathbf{X}_n ,
- the wake-perturbed Monte Carlo sample at the WT l : $\mathbf{X}'_{n,l}$ (output of the steady-state wake numerical model).

To ensure that the Monte-Carlo estimation converged, Figure 3.12 plots the squared MMD between the sample \mathbf{X}_n and the increasing samples $\mathbf{X}'_{i,l}, i \in 400, \dots, 6000$. After a few thousands of simulations, the MMD of each WT tends to converge towards a stable value, as expected. The design of experiment with $n = 6\,000$ is thus considered as sufficient.

3.5.3 Summary and discussion

A steady-state engineering wake model is coupled with a hydrostatic solver to take into account the effect of the floaters position in the wake computation of a floating offshore wind farm. The

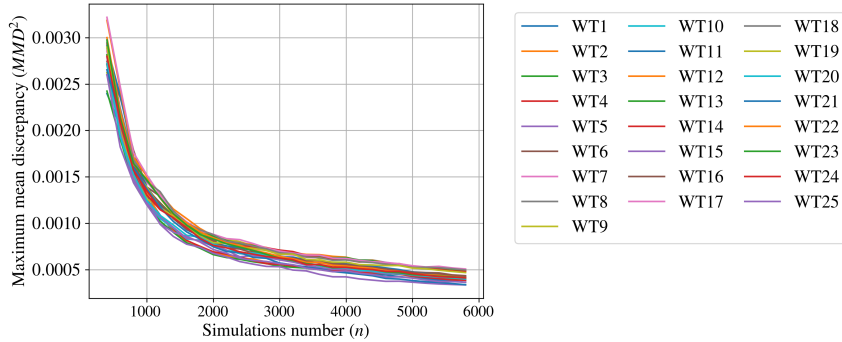


Figure 3.12 Convergence of the squared MMD estimation

main impact of the floater's position is the increased rotor tilt, which leads to a larger vertical deflection of the wake. In the South-Brittany farm, the elevation of wake center is significant and could modify the fatigue loads on the downstream WT. This low-fidelity, or engineering model is very fast (about 3 minutes on a regular computer), while higher fidelity models can simulate the wake in a wind farm more accurately, but with much higher computational cost (several days for LES Meso-NH solver, with intensive parallelisation). In this paper, we consider that the modelling error made by the engineering wake model as reasonable. Further investigations should be done on the integration of the different fidelity levels in the uncertainty propagation. In this work, the uncertainty propagation is performed for random inputs: the wind speed and the turbulence intensity, leading to a wake perturbed distribution per WT. A metric was then defined to measure the distance between distributions in order to build clusters of WT seeing similar wind conditions. After applying the metric to the South Brittany case, a clustering approach is used to determine a limited number of WTs representing the farm for RBD. Several clustering methods are compared and provide similar results for the current case study. In this case, a solution with 4 clusters is a good compromise between low relative error with clusters and low number of clusters. Getting a low number of clusters allows us to reduce the number of representative WT on which a RBD study can be done to assess the RBD over the whole farm. The differences among a cluster and between clusters have to be studied when looking directly to the output of interest for ultimate or fatigue reliability. However the difference on load output quantities may be reduced when compared to that on wake output quantities thanks to the damping of the WT. Depending on the definition of a wind farm failure (series system: one WT fails or parallel system: all WT fail or intermediate system), the probability of failure can be estimated from the probability of failure of the representative WT. These considerations need to be further explored to improve RBD at the farm scale.

3.6 Conclusion

Bibliography

- Abdo, T. and Rackwitz, R. (1991). A new beta-point algorithm for large time-invariant and time-variant reliability problems. In *Reliability and Optimization of Structural Systems' 90: Proceedings of the 3rd IFIP WG 7.5 Conference*, pages 1–12.
- Abdullah, M., Yatim, A., Tan, C., and Saidur, R. (2012). A review of maximum power point tracking algorithms for wind energy systems. *Renewable and sustainable energy reviews*, 16(5):3220–3227.
- Abtini, M. (2018). *Plans prédictifs à taille fixe et séquentiels pour le krigeage*. PhD thesis, Ecole Centrale Lyon.
- Ahmed, S., Hawlader, B., and Roy, K. (2015). Finite element modeling of large diameter monopiles in dense sand for offshore wind turbine foundations. In *International Conference on Offshore Mechanics and Arctic Engineering*, volume 56475, page V001T10A009. American Society of Mechanical Engineers.
- Ajenjo, A. (2023). *Info-gap robustness assessment of reliability evaluations for the safety of critical industrial systems*. PhD thesis, Université Bourgogne Franche-Comté.
- Ajenjo, A., Ardillon, E., Chabridon, V., Iooss, B., Cogan, S., and Sadoulet-Reboul, E. (2022). An info-gap framework for robustness assessment of epistemic uncertainty models in hybrid structural reliability analysis. *Structural Safety*, 96:102196.
- Al-Solihat, M. and Nahon, M. (2018). Flexible multibody dynamic modeling of a floating wind turbine. *International Journal of Mechanical Sciences*, 142:518–529.
- Ameryoun, H., Schoefs, F., Barillé, L., and Thomas, Y. (2019). Stochastic modeling of forces on jacket-type offshore structures colonized by marine growth. *Journal of Marine Science and Engineering*, 7(5):158.
- Ang, G., Ang, A. H.-S., and Tang, W. (1992). Optimal importance-sampling density estimator. *Journal of engineering mechanics*, 118(6):1146–1163.
- Ardillon, E., Paskyabi, M., Cousin, A., Dimitrov, N., Dupoirion, M., Eldevik, S., Fekhari, E., Ferreira, C., Guiton, M., Jezequel, B., et al. (2023). Turbine loading and wake model uncertainty. Technical report, European Union.
- Au, S.-K. and Beck, J. L. (2001). Estimation of small failure probabilities in high dimensions by subset simulation. *Probabilistic Engineering Mechanics*, 16(4):263–277.
- Auder, B., De Crecy, A., Iooss, B., and Marques, M. (2012). Screening and metamodeling of computer experiments with functional outputs. Application to thermal–hydraulic computations. *Reliability Engineering & System Safety*, 107:122–131.

- Bachoc, F. (2013). Cross validation and maximum likelihood estimations of hyper-parameters of Gaussian processes with model misspecification. *Computational Statistics & Data Analysis*, 66:55–69.
- Bai, Z., Radhakrishna-Rao, C., and Zhao, L. (1989). Kernel estimators of density function of directional data. In *Multivariate statistics and probability*, pages 24–39.
- Baker, E., Barbillon, P., Fadikar, A., Gramacy, R., Herbei, R., Higdon, D., Huang, J., Johnson, L., Mondal, A., Pires, B., et al. (2020). Stochastic simulators: An overview with opportunities. arXiv preprint arXiv:2002.01321.
- Baudin, M., Dutfoy, A., Iooss, B., and Popelin, A. (2017). Open TURNS: An industrial software for uncertainty quantification in simulation. In Ghanem, R., Higdon, D., and Owhadi, H., editors, *Springer Handbook on Uncertainty Quantification*, pages 2001–2038. Springer.
- Beauregard, E., Bérille, E., Berrabah, N., Berthelot, M., Burrows, J., Capaldo, M., Cornet, S., Costan, V., Duchet, M., Dufossé, E., Dupont, E., Franchet, M., Gouze, E., Grau, A., Joly, A., Kell, N., de Laleu, V., Latraube, F., Lovera, A., de Bazelaire, A., Monnot, E., Nogaro, G., Pagot, J., Pérony, R., Peyrard, C., Piguet, C., Régnier, A., Santibanez, E., Senn, C., Smith, C., Soriano, F., Stephan, P., Terte, N., Veyan, P., Vizireanu, D., and Yeow, L. (2022). *L'éolien en mer : un défi pour la transition énergétique*. Lavoisier.
- Bect, J., Bachoc, F., and Ginsbourger, D. (2019). A supermartingale approach to Gaussian process based sequential design of experiments. *Bernoulli*, 25(4A):2883 – 2919.
- Bect, J., Ginsbourger, D., Li, L., Picheny, V., and Vazquez, E. (2012). Sequential design of computer experiments for the estimation of a probability of failure. *Statistics and Computing*, 22:773–793.
- Beer, M., Ferson, S., and Kreinovich, V. (2013). Imprecise probabilities in engineering analyses. *Mechanical systems and signal processing*, 37(1-2):4–29.
- Beirlant, J., Goegebeur, Y., Segers, J., and Teugels, J. (2006). *Statistics of extremes: theory and applications*. John Wiley & Sons.
- Bénard, C., Biau, G., Da Veiga, S., and Scornet, E. (2022). SHAFF: Fast and consistent SHAPley eFfct estimates via random Forests. In *Proceedings of The 25th International Conference on Artificial Intelligence and Statistics*, volume 151, pages 5563–5582.
- Benoumechiara, N. and Elie-Dit-Cosaque, K. (2019). Shapley effects for sensitivity analysis with dependent inputs: bootstrap and kriging-based algorithms. *ESAIM: Proceedings and Surveys*, 65:266–293.
- Binois, M., Huang, J., Gramacy, R., and Ludkovski, M. (2019). Replication or exploration? Sequential design for stochastic simulation experiments. *Technometrics*, 61(1):7–23.
- Bitner-Gregersen, E. (2015). Joint met-ocean description for design and operations of marine structures. *Applied Ocean Research*, 51:279–292.
- Bjerager, P. (1988). Probability integration by directional simulation. *Journal of Engineering Mechanics*, 114(8):1285–1302.
- Blatman, G. and Sudret, B. (2011). Adaptive sparse polynomial chaos expansion based on least angle regression. *Journal of computational Physics*, 230(6):2345–2367.
- Bossanyi, E. (2003). Individual blade pitch control for load reduction. *Wind Energy: An International Journal for Progress and Applications in Wind Power Conversion Technology*, 6(2):119–128.

- Bouezmarni, T., Ghouch, E., and Taamouti, A. (2013). Bernstein estimator for unbounded copula densities. *Statistics & Risk Modeling*, 30(4):343–360.
- Bourinet, J.-M. (2018). *Reliability analysis and optimal design under uncertainty-Focus on adaptive surrogate-based approaches*. PhD thesis, Université Clermont Auvergne.
- Branlard, E. (2017). *Wind turbine aerodynamics and vorticity-based methods: Fundamentals and recent applications*. Springer.
- Breiman, L. (1996). Bagging predictors. *Machine learning*, 24:123–140.
- Briol, F., Oates, C., Girolami, M., Osborne, M., and Sejdinovic, D. (2019). Probabilistic Integration: A Role in Statistical Computation? *Statistical Science*, 34:1 – 22.
- Bucher, C. (1988). Adaptive sampling—an iterative fast Monte Carlo procedure. *Structural safety*, 5(2):119–126.
- Bugallo, M., Elvira, V., Martino, L., Luengo, D., Miguez, J., and Djuric, P. (2017). Adaptive importance sampling: The past, the present, and the future. *IEEE Signal Processing Magazine*, 34(4):60–79.
- Bui, H. and Bakhoday-Paskyabi, M. (2022). Mesoscale Simulation of Open Cellular Convection: Roles of Model Resolutions and Physics Parameterizations. In *Journal of Physics: Conference Series*, volume 2362, page 012006.
- Burton, T., Jenkins, N., Bossanyi, E., Sharpe, D., and Graham, M. (2021). *Wind energy handbook*. John Wiley & Sons.
- Caillé, F., Bozonnet, P., Perdrizet, T., Poirette, Y., and Melis, C. (2017). Model test and simulation comparison for an inclined-leg TLP dedicated to floating wind. In *International Conference on Offshore Mechanics and Arctic Engineering*, volume 57786, page V010T09A070. American Society of Mechanical Engineers.
- Cermelli, C., Leroux, C., Díaz-Domínguez, S., and Peiffer, A. (2018). Experimental measurements of WindFloat 1 prototype responses and comparison with numerical model. In *International Conference on Offshore Mechanics and Arctic Engineering*, volume 51319, page V010T09A050.
- Cérou, F., Guyader, A., and Rousset, M. (2019). Adaptive multilevel splitting: Historical perspective and recent results. *Chaos: An Interdisciplinary Journal of Nonlinear Science*, 29(4):043108.
- Chabridon, V. (2018). *Reliability-oriented sensitivity analysis under probabilistic model uncertainty—Application to aerospace systems*. PhD thesis, Université Clermont Auvergne.
- Chen, T., Wang, X., Yuan, G., and Liu, J. (2018). Fatigue bending test on grouted connections for monopile offshore wind turbines. *Marine Structures*, 60:52–71.
- Chen, Y., Welling, M., and Smola, A. (2010). Super-samples from kernel herding. In *Proceedings of the Twenty-Sixth Conference on Uncertainty in Artificial Intelligence*, pages 109 – 116. AUAI Press.
- Cordle, A. and Jonkman, J. (2011). State of the art in floating wind turbine design tools. In *ISOPE International Ocean and Polar Engineering Conference*.
- Cortes, C. and Vapnik, V. (1995). Support-vector networks. *Machine learning*, 20:273–297.
- Cottin, C. and Pfeifer, D. (2014). From Bernstein polynomials to Bernstein copulas. *J. Appl. Funct. Anal.*, 9(3-4):277–288.

- Cousin, A. (2021). *Optimisation sous contraintes probabilistes d'un système complexe : Application au dimensionnement d'une éolienne offshore flottante*. PhD thesis, Institut Polytechnique de Paris.
- Da Veiga, S. (2015). Global sensitivity analysis with dependence measures. *Journal of Statistical Computation and Simulation*, 85:1283 – 1305.
- da Veiga, S. (2021). Kernel-based anova decomposition and shapley effects – application to global sensitivity analysis.
- Da Veiga, S., Gamboa, F., Iooss, B., and Prieur, C. (2021). *Basics and Trends in Sensitivity Analysis: Theory and Practice in R*. Society for Industrial and Applied Mathematics.
- Dai, J., Hu, Y., Liu, D., and Long, X. (2011). Aerodynamic loads calculation and analysis for large scale wind turbine based on combining BEM modified theory with dynamic stall model. *Renewable Energy*, 36(3):1095–1104.
- Damblin, G., Couplet, M., and Iooss, B. (2013). Numerical studies of space-filling designs: Optimization of Latin Hypercube Samples and subprojection properties. *Journal of Simulation*, 7.
- De Lozzo, M. and Marrel, A. (2016). New improvements in the use of dependence measures for sensitivity analysis and screening. *Journal of Statistical Computation and Simulation*, 86(15):3038–3058.
- de Rocquigny, E., Devictor, N., and Tarantola, S. (2008). *Uncertainty in industrial practice: a guide to quantitative uncertainty management*. John Wiley & Sons.
- Deheuvels, P. (1979). La fonction de dépendance empirique et ses propriétés. Un test non paramétrique d'indépendance. *Bulletins de l'Académie Royale de Belgique*, 65(1):274–292.
- Demange-Chryst, J., Bachoc, F., and Morio, J. (2023). Shapley effect estimation in reliability-oriented sensitivity analysis with correlated inputs by importance sampling. *International Journal for Uncertainty Quantification*, 13(3).
- Der Kiureghian, A. and Dakessian, T. (1998). Multiple design points in first and second-order reliability. *Structural Safety*, 20:37–49.
- Der Kiureghian, A. and Ditlevsen, O. (2009). Aleatory or epistemic? Does it matter? *Structural Safety*, 31(2):105–112.
- Dimitrov, N. and Natarajan, A. (2017). Application of simulated lidar scanning patterns to constrained Gaussian turbulence fields for load validation. *Wind Energy*, 20(1):79–95.
- Dimitrov, N., Natarajan, A., and Mann, J. (2017). Effects of normal and extreme turbulence spectral parameters on wind turbine loads. *Renewable Energy*, 101:1180–1193.
- Dirlik, T. and Benasciutti, D. (2021). Dirlik and tovo-benasciutti spectral methods in vibration fatigue: a review with a historical perspective. *Metals*, 11(9):1333.
- DNV-OS-J103 (2013). DNV-OS-J103: Design of floating wind turbine structures. Technical report, Det Norske Veritas.
- DNV-RP-C203 (2016). DNV-RP-C203: Fatigue design of offshore steel structures. Technical report, Det Norske Veritas.
- DNV-ST-0126 (2018). Dnv-st-0126: Support structures for wind turbines. *Copenhagen, Denmark: DNV*.

- DNV-ST-0437 (2016). DNV-ST-0437: Loads and site conditions for wind turbines. Technical report, Det Norske Veritas.
- Doubrawa, P., Churchfield, M., Godvik, M., and Sirnivas, S. (2019). Load response of a floating wind turbine to turbulent atmospheric flow. *Applied Energy*, 242:1588–1599.
- Doubrawa, P., Quon, E., Martinez-Tossas, L., Shaler, K., Debnath, M., Hamilton, N., Herges, T., Maniaci, D., Kelley, C., Hsieh, A., et al. (2020). Multimodel validation of single wakes in neutral and stratified atmospheric conditions. *Wind Energy*, 23(11):2027–2055.
- Dowling, N. E. (1972). Fatigue Failure Predictions for Complicated Stress-Strain Histories. *Journal of Materials, JMLSA*, 7:71 – 87.
- Drexler, S. and Muskulus, M. (2021). Reliability of an offshore wind turbine with an uncertain S-N curve. *Journal of Physics: Conference Series*, 2018:012014.
- Driscoll, F., Jonkman, J., Robertson, A., Sirnivas, S., Skaare, B., and Nielsen, F. (2016). Validation of a FAST model of the statoil-hywind demo floating wind turbine. *Energy Procedia*, 94:3–19. 13th Deep Sea Offshore Wind R&D Conference, EERA DeepWind’2016.
- Durante, F. and Sempi, C. (2015). *Principles of copula theory*. CRC press.
- Echard, B., Gayton, N., and Lemaire, M. (2011). AK-MCS: An active learning reliability method combining Kriging and Monte Carlo Simulation. *Structural Safety*, 33:145–154.
- Ehre, M., Papaioannou, I., and Straub, D. (2020). A framework for global reliability sensitivity analysis in the presence of multi-uncertainty. *Reliability Engineering & System Safety*, 195:106726.
- Ewans, K. C., Bitner-Gregersen, E. M., and Guedes-Soares, C. (2004). Estimation of Wind-Sea and Swell Components in a Bimodal Sea State. *Journal of Offshore Mechanics and Arctic Engineering*, 128(4):265–270.
- Fan, J. and Lv, J. (2010). A selective overview of variable selection in high dimensional feature space. *Statistica Sinica*, 20(1):101.
- Fang, K., Liu, M.-Q., Qin, H., and Zhou, Y.-D. (2018). *Theory and application of uniform experimental designs*, volume 221. Springer.
- Fatemi, A. and Yang, L. (1998). Cumulative fatigue damage and life prediction theories: a survey of the state of the art for homogeneous materials. *International Journal of Fatigue*, 20(1):9–34.
- Fazeres-Ferradosa, T., Chambel, J., Taveira-Pinto, F., Rosa-Santos, P., Taveira-Pinto, F., Giannini, G., and Haerens, P. (2021). Scour protections for offshore foundations of marine energy harvesting technologies: A review. *Journal of Marine Science and Engineering*, 9(3):297.
- Fekhari, E., Baudin, M., Chabridon, V., and Jebroun, Y. (2021). otbenchmark: an open source Python package for benchmarking and validating uncertainty quantification algorithms. In *Proceedings of the 4th International Conference on Uncertainty Quantification in Computational Sciences and Engineering*, pages 218 – 231.
- Fernández-Godino, M., Park, C., Kim, N.-H., and Haftka, R. (2016). Review of multi-fidelity models. arXiv preprint arXiv:1609.07196.
- Fleming, P., King, J., Bay, C., Simley, E., Mudafort, R., Hamilton, N., Farrell, A., and Martinez-Tossas, L. (2020). Overview of FLORIS updates. In *Journal of Physics: Conference Series*, volume 1618, page 022028.

- Forrester, A., Sobester, A., and Keane, A. (2008). *Engineering design via surrogate modelling: a practical guide*. John Wiley & Sons.
- Freyssinet, C., Rey, V., Schoefs, F., and Moro, T. (2023). Bayesian calibration of a non linear damage model of steel structures with random material property: Sensitivity analysis and reliability assessment. *Engineering Structures*, 295:116853.
- Galparsoro, I., Menchaca, I., Garmendia, J., Borja, A., Maldonado, A., Iglesias, G., and Bald, J. (2022). Reviewing the ecological impacts of offshore wind farms. *npj Ocean Sustainability*, 1(1):1.
- Genest, C., Nešlehová, J. G., and Rémillard, B. (2017). Asymptotic behavior of the empirical multilinear copula process under broad conditions. *Journal of Multivariate Analysis*, 159:82–110.
- Geoga, C., Anitescu, M., and Stein, M. (2020). Scalable Gaussian process computations using hierarchical matrices. *Journal of Computational and Graphical Statistics*, 29(2):227–237.
- Geyer, S., Papaioannou, I., and Straub, D. (2019). Cross entropy-based importance sampling using Gaussian densities revisited. *Structural Safety*, 76:15–27.
- Giles, M. (2008). Multilevel Monte Carlo Path Simulation. *Operations Research*, 56:607–617.
- Gionfra, N. (2018). *Stratégies de commande distribuée pour l'optimisation de la production des fermes éoliennes*. PhD thesis, Université Paris-Saclay; La Sapienza, Università di Roma.
- Glad, I., Hjort, N., and Ushakov, N. (2007). Mean-squared error of kernel estimators for finite values of the sample size. *Journal of Mathematical Sciences*, 146(4):5977–5983.
- Gobet, E., Lerasle, M., and Métivier, D. (2022). Mean estimation for randomized quasi Monte Carlo method. hal-03631879v3.
- González-Barrios, J. and Hoyos-Argüelles, R. (2021). Estimating checkerboard approximations with sample d-copulas. *Communications in Statistics-Simulation and Computation*, 50(12):3992–4027.
- Gottschall, J., Gribben, B., Stein, D., and Würth, I. (2017). Floating lidar as an advanced offshore wind speed measurement technique: current technology status and gap analysis in regard to full maturity. *Wiley Interdisciplinary Reviews: Energy and Environment*, 6(5):e250.
- Gramacy, R. (2020). *Surrogates: Gaussian process modeling, design, and optimization for the applied sciences*. CRC press.
- Grasedyck, L., Kressner, D., and Tobler, C. (2013). A literature survey of low-rank tensor approximation techniques. *GAMM-Mitteilungen*, 36(1):53–78.
- Gretton, A., Borgwardt, K. M., Rasch, M., Schölkopf, B., and Smola, A. (2006). A Kernel Method for the Two-Sample-Problem. In *Proceedings of the 19th International Conference on Neural Information Processing Systems*, pages 513–520.
- Guédé, Z., Sudret, B., and Lemaire, M. (2007). Life-time reliability based assessment of structures submitted to thermal fatigue. *International Journal of Fatigue*, 29(7):1359–1373.
- Guignier, L., Courbois, A., Mariani, R., and Choisnet, T. (2016). Multibody Modelling of Floating Offshore Wind Turbine Foundation for Global Loads Analysis. In *International Ocean and Polar Engineering Conference*, pages ISOPE-I-16–392.

- Han, Q., Hao, Z., Hu, T., and Chu, F. (2018). Non-parametric models for joint probabilistic distributions of wind speed and direction data. *Renewable Energy*, 126:1032–1042.
- Hansen, N., Auger, A., Ros, R., Mersmann, O., Tušar, T., and Brockhoff, D. (2021). COCO: A platform for comparing continuous optimizers in a black-box setting. *Optimization Methods and Software*, 36(1):114–144.
- Hartigan, J. (1975). Printer graphics for clustering. *Journal of Statistical Computation and Simulation*, 4(3):187–213.
- Hasselmann, K., Barnett, T., Bouws, E., Carlson, H., Cartwright, D., Enke, K., Ewing, J., Gienapp, A., Hasselmann, D., Kruseman, P., et al. (1973). Measurements of wind-wave growth and swell decay during the Joint North Sea Wave Project (JONSWAP). *Ergaenzungsheft zur Deutschen Hydrographischen Zeitschrift, Reihe A*.
- Hastie, T., Tibshirani, R., and Friedman, J. (2009). *The elements of statistical learning: data mining, inference, and prediction*, volume 2. Springer.
- Hawchar, L., El Soueid, C.-P., and Schoefs, F. (2017). Principal component analysis and polynomial chaos expansion for time-variant reliability problems. *Reliability Engineering & System Safety*, 167:406–416.
- Hegseth, J. and Bachynski, E. (2019). A semi-analytical frequency domain model for efficient design evaluation of spar floating wind turbines. *Marine Structures*, 64:186–210.
- Heier, S. (2014). *Grid integration of wind energy: onshore and offshore conversion systems*. John Wiley & Sons.
- Heinrich, J. and Weiskopf, D. (2013). State of the art of parallel coordinates. *Eurographics (state of the art reports)*, pages 95–116.
- Hickernell, F. (1998). A generalized discrepancy and quadrature error bound. *Mathematics of computation*, 67(221):299–322.
- Hirvoas, A. (2021). *Development of a data assimilation method for the calibration and continuous update of wind turbines digital twins*. PhD thesis, Université Grenoble Alpes.
- Hoeffding, W. (1948). A class of statistics with asymptotically normal distributions. *Annals of Mathematical Statistics*, 19(3):293–325.
- Holm-Jørgensen, K. (2009). *Nonlinear multibody dynamics of wind turbines*. PhD thesis, Aalborg University.
- Huchet, Q. (2019). *Kriging based methods for the structural damage assessment of offshore wind turbines*. PhD thesis, Université Blaise Pascal.
- IEC-61400-1 (2019). IEC 61400-1: Wind energy generation systems - Part 1: Design requirements. Technical report, International Electrotechnical Commission (IEC).
- Janssen, P., Swanepoel, J., and Veraverbeke, N. (2012). Large sample behavior of the Bernstein copula estimator. *Journal of Statistical Planning and Inference*, 142(5):1189 – 1197.
- Jensen, J. and Skelton, K. (2018). Wind turbine blade recycling: Experiences, challenges and possibilities in a circular economy. *Renewable and Sustainable Energy Reviews*, 97:165–176.
- Jensen, N. (1983). A note on wind generator interaction. Technical report, DTU.
- Jiang, Z. (2021). Installation of offshore wind turbines: A technical review. *Renewable and Sustainable Energy Reviews*, 139:110576.

- Joe, H. (1997). *Multivariate Models and Multivariate Dependence Concepts*. Chapman and Hall.
- Joe, H. (2014). *Dependence modeling with copulas*. CRC press.
- Joe, H. and Kurowicka, D. (2011). *Dependence modeling: vine copula handbook*. World Scientific.
- Jones, D., Schonlau, M., and Welch, W. (1998). Efficient global optimization of expensive black-box functions. *Journal of Global optimization*, 13:455–492.
- Jonkman, B. (2009). Turbsim User's Guide: Version 1.50. Technical report, NREL.
- Joseph, V., Gul, E., and Ba, S. (2015). Maximum projection designs for computer experiments. *Biometrika*, 102.
- Kaimal, J., Wyngaard, J., Izumi, Y., and Coté, O. (1972). Spectral characteristics of surface-layer turbulence. *Quarterly Journal of the Royal Meteorological Society*, 98(417):563–589.
- Kallehave, D., Byrne, B. W., LeBlanc T., C., and M., K. K. (2015). Optimization of monopiles for offshore wind turbines. *Philosophical Transactions of the Royal Society A: Mathematical, Physical and Engineering Sciences*, 373(2035):20140100.
- Kaplan, Z., Li, Y., Nakayama, M., and Tuffin, B. (2019). Randomized quasi-Monte Carlo for quantile estimation. In *2019 Winter Simulation Conference (WSC)*, pages 428–439.
- Kelly, M. and Vanem, E. (2022). Environmental joint probability distributions and uncertainties. Technical report, Tech Rep. of HIPERWIND H2020 project, Grant Agreement No. 101006689, <https://www.hiperwind.eu/>.
- Kim, T., Natarajan, A., Lovera, A., Julian, E., Peyrard, E., Capaldo, M., Huwart, G., Bozonnet, P., and Guiton, M. (2022). A comprehensive code-to-code comparison study with the modified IEA15MW-UMaine Floating Wind Turbine for H2020 HIPERWIND project. *Journal of Physics: Conference Series*, 2265(4):042006.
- Kiriliouk, A., Segers, J., and Tsukahara, H. (2021). *Resampling procedures with empirical beta copulas*, pages 27–53. Springer.
- Koehler, J. and Owen, A. (1996). 9 Computer experiments. In *Design and Analysis of Experiments*, volume 13 of *Handbook of Statistics*, pages 261–308. Elsevier.
- Koutsourelakis, P. (2004). Reliability of structures in high dimensions. Part II. Theoretical validation. *Probabilistic engineering mechanics*, 19(4):419–423.
- Kucherenko, S. and Iooss, B. (2017). *Derivative-Based Global Sensitivity Measures*, pages 1241–1263. Springer International Publishing, Cham.
- Kucherenko, S., Rodriguez-Fernandez, M., Pantelides, C., and Shah, N. (2009). Monte Carlo evaluation of derivative-based global sensitivity measures. *Reliability Engineering & System Safety*, 94:1135–1148. Special Issue on Sensitivity Analysis.
- Kurtz, N. and Song, J. (2013). Cross-entropy-based adaptive importance sampling using Gaussian mixture. *Structural Safety*, 42:35–44.
- Lamboni, M., Iooss, B., Popelin, A.-L., and Gamboa, F. (2013). Derivative-based global sensitivity measures: General links with Sobol' indices and numerical tests. *Mathematics and Computers in Simulation*, 87:45–54.
- Larsen, G. C., Madsen, H., Thomsen, K., and Larsen, T. (2008). Wake meandering: a pragmatic approach. *Wind Energy: An International Journal for Progress and Applications in Wind Power Conversion Technology*, 11(4):377–395.

- Lasserre, J.-B. (2023). Chebyshev and equilibrium measure vs bernstein and lebesgue measure.
- Lasserre, M. (2022). *Apprentissages dans les réseaux bayésiens à base de copules non-paramétriques*. PhD thesis, Sorbonne Université.
- Lataniotis, C. (2019). *Data-driven uncertainty quantification for high-dimensional engineering problems*. PhD thesis, ETH Zürich.
- Laurie, D. (1997). Calculation of Gauss-Kronrod quadrature rules. *Mathematics of Computation*, 66(219):1133–1145.
- Le, T., Eiksund, G., Strøm, P., and Sæu, M. (2014). Geological and geotechnical characterisation for offshore wind turbine foundations: A case study of the Sheringham Shoal wind farm. *Engineering Geology*, 177:40–53.
- Le Maître, O. and Knio, O. (2010). *Spectral methods for uncertainty quantification: with applications to computational fluid dynamics*. Springer Science & Business Media.
- Le Riche, R. and Picheny, V. (2021). Revisiting Bayesian optimization in the light of the COCO benchmark. *Structural and Multidisciplinary Optimization*, 64(5):3063–3087.
- Lebrun, R. (2013). *Contributions à la modélisation de la dépendance stochastique*. PhD thesis, Université Paris-Diderot – Paris VII. (in English).
- L’Ecuyer, P. (2018). Randomized Quasi-Monte Carlo: An Introduction for Practitioners. In *Monte Carlo and Quasi-Monte Carlo Methods*, pages 29–52, Cham. Springer International Publishing.
- Lemaire, M. (2013). *Structural reliability*. John Wiley & Sons.
- Lemaître, P., Sergienko, E., Arnaud, A., Bousquet, N., Gamboa, F., and Iooss, B. (2015). Density modification-based reliability sensitivity analysis. *Journal of Statistical Computation and Simulation*, 85(6):1200–1223.
- Leobacher, G. and Pillichshammer, F. (2014). *Introduction to quasi-Monte Carlo integration and applications*. Springer.
- Li, X., Mikusiński, P., and Taylor, M. D. (1998). Strong approximation of copulas. *Journal of Mathematical Analysis and Applications*, 225(2):608–623.
- Li, Y., Kang, L., and Hickernell, F. (2020). Is a transformed low discrepancy design also low discrepancy? *Contemporary Experimental Design, Multivariate Analysis and Data Mining: Festschrift in Honour of Professor Kai-Tai Fang*, pages 69–92.
- Lieudarde, H.-P. (1982). *La Pratique des essais de fatigue – méthodes expérimentales et analyse des résultats*. Pyc édition.
- Lin, Y. and Dong, S. (2019). Wave energy assessment based on trivariate distribution of significant wave height, mean period and direction. *Applied Ocean Research*, 87:47–63.
- Lovera, A. (2019). *Cyclic lateral design for offshore monopiles in weak rocks*. PhD thesis, Université Paris Est.
- MacKinnon, D., Afewerki, S., and Karlsen, A. (2022). Technology legitimation and strategic coupling: A cross-national study of floating wind power in Norway and Scotland. *Geoforum*, 135:1–11.
- Mak, S. and Joseph, V. (2018). Support points. *The Annals of Statistics*, 46:2562 – 2592.
- Mann, J. (1998). Wind field simulation. *Probabilistic engineering mechanics*, 13(4):269–282.

- Mara, T. A. and Tarantola, S. (2012). Variance-based sensitivity indices for models with dependent inputs. *Reliability Engineering & System Safety*, 107:115–121.
- Marelli, S. and Sudret, B. (2014). UQLab: A framework for uncertainty quantification in Matlab. In *Vulnerability, uncertainty, and risk: quantification, mitigation, and management*, pages 2554–2563.
- Marrel, A. and Chabridon, V. (2021). Statistical developments for target and conditional sensitivity analysis: Application on safety studies for nuclear reactor. *Reliability Engineering & System Safety*, 214:107711.
- Marrel, A., Iooss, B., Laurent, B., and Roustant, O. (2009). Calculations of Sobol indices for the Gaussian process metamodel. *Reliability Engineering & System Safety*, 94(3):742–751.
- Marty, A., Berhault, C., Damblans, G., Facq, J.-V., Gaurier, B., Germain, G., Soulard, T., and Schoefs, F. (2021). Experimental study of hard marine growth effect on the hydrodynamical behaviour of a submarine cable. *Applied Ocean Research*, 114:102810.
- Matha, D., Schlipf, M., Pereira, R., and Jonkman, J. (2011). Challenges in simulation of aerodynamics, hydrodynamics, and mooring-line dynamics of floating offshore wind turbines. In *ISOPE International Ocean and Polar Engineering Conference*.
- Matsumoto, M. and Nishimura, T. (1998). Mersenne twister: a 623-dimensionally equidistributed uniform pseudo-random number generator. *ACM Transactions on Modeling and Computer Simulation (TOMACS)*, 8(1):3–30.
- Mckay, M., Beckman, R., and Conover, W. (1979). A Comparison of Three Methods for Selecting Vales of Input Variables in the Analysis of Output From a Computer Code. *Technometrics*, 21:239 – 245.
- Mei, X. and Xiong, M. (2021). Effects of second-order hydrodynamics on the dynamic responses and fatigue damage of a 15 mw floating offshore wind turbine. *Journal of Marine Science and Engineering*, 9(11):1232.
- Meyers, J., Bottasso, C., Dykes, K., Fleming, P., Gebraad, P., Giebel, G., Göçmen, T., and Van Wingerden, J. (2022). Wind farm flow control: prospects and challenges. *Wind Energy Science Discussions*, 2022:1–56.
- Milano, D. (2021). *Numerical prototype for floating offshore wind turbines*. PhD thesis, The University of Edinburgh.
- Montes-Iturriaga, R. and Heredia-Zavoni, E. (2016). 'multivariate environmental contours using c-vine copulas'. *Ocean engineering*, 118:68–82.
- Morio, J. (2011). Non-parametric adaptive importance sampling for the probability estimation of a launcher impact position. *Reliability Engineering and System Safety*, 96(1):178–183.
- Morio, J. and Balesdent, M. (2015). *Estimation of Rare Event Probabilities in Complex Aerospace and Other Systems: A Practical Approach*. Woodhead Publishing, Elsevier.
- Morokoff, W. J. and Caflisch, R. E. (1995). Quasi-Monte Carlo Integration. *Journal of Computational Physics*, 122(2):218–230.
- Morris, M. (1991). Factorial sampling plans for preliminary computational experiments. *Technometrics*, 33:161–174.
- Moustapha, M., Marelli, S., and Sudret, B. (2022). Active learning for structural reliability: Survey, general framework and benchmark. *Structural Safety*, 96:102174.

- Nagababu, G., Srinivas, B., Kachhwaha, S., Puppala, H., and Kumar, S. (2023). Can offshore wind energy help to attain carbon neutrality amid climate change? A GIS-MCDM based analysis to unravel the facts using CORDEX-SA. *Renewable Energy*, page 119400.
- Nagler, T., Schellhase, C., and Czado, C. (2017). Nonparametric estimation of simplified vine copula models: comparison of methods. *Dependence Modeling*, 5:99–120.
- Nelsen, R. (2006). *An introduction to copulas*. Springer.
- Oates, C. and Sullivan, T. (2019). A modern retrospective on probabilistic numerics. *Statistics and computing*, 29(6):1335–1351.
- Oberkampf, W. and Roy, C. (2010). *Verification and validation in scientific computing*. Cambridge university press.
- Otter, A., Murphy, J., Pakrashi, V., Robertson, A., and Desmond, C. (2022). A review of modelling techniques for floating offshore wind turbines. *Wind Energy*, 25(5):831–857.
- Owen, A. (2003). The dimension distribution and quadrature test functions. *Statistica Sinica*, 13:1–17.
- Owen, A. (2013). Monte Carlo theory, methods and examples.
- Owen, A. (2014). Sobol' indices and Shapley value. *SIAM/ASA Journal on Uncertainty Quantification*, 2(1):245–251.
- Owen, A. and Zhou, Y. (2000). Safe and effective importance sampling. *Journal of the American Statistical Association*, 95(449):135–143.
- Papaioannou, I., Betz, W., Zwirglmaier, K., and Straub, D. (2015). MCMC algorithms for Subset Simulation. *Probabilistic Engineering Mechanics*, 41:89–103.
- Papaioannou, I., Geyer, S., and Straub, D. (2019). Improved cross entropy-based importance sampling with a flexible mixture model. *Reliability Engineering & System Safety*, 191:106564.
- Papaioannou, I. and Straub, D. (2021). Variance-based reliability sensitivity analysis and the FORM α -factors. *Reliability Engineering & System Safety*, 210:107496.
- Papakonstantinou, K., N., H., and Eshra, E. (2023). Hamiltonian MCMC methods for estimating rare events probabilities in high-dimensional problems. *Probabilistic Engineering Mechanics*, 74:103485.
- Petit, S. (2022). *Improved Gaussian process modeling : Application to Bayesian optimization*. PhD thesis, Université Paris-Saclay.
- Petrovska, E. (2022). *Fatigue life reassessment of monopile-supported offshore wind turbine structures*. PhD thesis, University of Edinburgh.
- Plischke, E. and Borgonovo, E. (2019). Copula theory and probabilistic sensitivity analysis: Is there a connection? *European Journal of Operational Research*, 277(3):1046–1059.
- Póczos, B., Ghahramani, Z., and Schneider, J. (2012). Copula-Based Kernel Dependency Measures. In *Proceedings of the 29th International Conference on International Conference on Machine Learning*, ICML'12, pages 1635–1642.
- Popko, W., Robertson, A., Jonkman, J., Wendt, F., Thomas, P., Müller, K., Kretschmer, M., Hagen, T., Galinos, C., Le Dreff, J.-B., et al. (2021). Validation of numerical models of the offshore wind turbine from the alpha ventus wind farm against full-scale measurements within OC5 Phase III. *Journal of Offshore Mechanics and Arctic Engineering*, 143(1):012002.

- Powell, M. (1994). *A direct search optimization method that models the objective and constraint functions by linear interpolation*. Springer.
- Pronzato, L. and Müller, W. (2012). Design of computer experiments: space filling and beyond. *Statistics and Computing*, 22:681–701.
- Pulselli, R., Maccanti, M., Bruno, M., Sabbetta, A., Neri, E., Patrizi, N., and Bastianoni, S. (2022). Benchmarking marine energy technologies through LCA: Offshore floating wind farms in the mediterranean. *Frontiers in Energy Research*, 10:902021.
- Qiu, J., Wu, Q., Ding, G., Xu, Y., and Feng, S. (2016). A survey of machine learning for big data processing. *EURASIP Journal on Advances in Signal Processing*, 2016:1–16.
- Ragan, P. and Manuel, L. (2007). Comparing estimates of wind turbine fatigue loads using time-domain and spectral methods. *Wind engineering*, 31(2):83–99.
- Rahman, S. (2016). The f-sensitivity index. *SIAM/ASA journal on uncertainty quantification*, 4(1):130–162.
- Raoult, C., Joly, A., Andreevsky, M., and Joly-Lauzel, A. (2018). Anemoc-3: amélioration de la base de données d'état de mer anemoc-2 par prise en compte des effets de la marée anemoc-3: improving the anemoc-2 sea state database by adding tide effects. In *16e journées de l'hydrodynamique*.
- Rasmussen, C. and Williams, C. (2006). *Gaussian processes for machine learning*, volume 1. Springer.
- Reale, C., Tott-Buswell, J., and Prendergast, L. (2021). Impact of geotechnical uncertainty on the preliminary design of monopiles supporting offshore wind turbines. *ASCE-ASME Journal of Risk and Uncertainty in Engineering Systems, Part B: Mechanical Engineering*, 7(4):040903.
- Ren, Z., Verma, A., Li, Y., Teuwen, J., and Jiang, Z. (2021). Offshore wind turbine operations and maintenance: A state-of-the-art review. *Renewable and Sustainable Energy Reviews*, 144:110886.
- Robertson, A., Gueydon, S., Bachynski, E., Wang, L., Jonkman, J., Alarcon, D., Amet, E., Beardsell, A., Bonnet, P., Boudet, B., et al. (2020). OC6 Phase I: Investigating the underprediction of low-frequency hydrodynamic loads and responses of a floating wind turbine. *1618(3):032033*.
- Rocher, B., Schoefs, S., François, M., Salou, A., and Caouissin, A.-L. (2020). A two-scale probabilistic time-dependent fatigue model for offshore steel wind turbines. *International Journal of Fatigue*, 136:105620.
- Rockafellar, R. and Royset, J. (2015). Engineering Decisions under Risk Averseness. *ASCE-ASME Journal of Risk and Uncertainty in Engineering Systems, Part A: Civil Engineering*, 1.
- Rollón de Pinedo, A., Couplet, M., Iooss, B., Marie, N., Marrel, A., Merle, E., and Sueur, R. (2021). Functional outlier detection by means of h-mode depth and dynamic time warping. *Applied Sciences*, 11(23):11475.
- Rongé, E., Peyrard, C., Venugopal, V., Xiao, Q., Johanning, L., and Benoit, M. (2023). Evaluation of second and third-order numerical wave-loading models for floating offshore wind TLPs. *Ocean Engineering*, 288:116064.
- Rose, D. (2015). *Modeling and estimating multivariate dependence structures with the Bernstein copula*. PhD thesis, Ludwig Maximilian University of Munich.

- Rott, A., Doekemeijer, B., Seifert, J., van Wingerden, J., and Kühn, M. (2018). Robust active wake control in consideration of wind direction variability and uncertainty. *Wind energy science*, 3(2):869–882.
- Rozsas, A. and Slobbe, A. (2019). Repository and black-box reliability challenge 2019.
- Rubinstein, R. Y. and Kroese, D. P. (2004). *The cross-entropy method: a unified approach to combinatorial optimization, Monte-Carlo simulation, and machine learning*, volume 133. Springer.
- Saltelli, A., Ratto, M., Andres, T., Campolongo, F., Cariboni, J., Gatelli, D., Saisana, M., and Tarantola, S. (2008). *Global sensitivity analysis: the primer*. John Wiley & Sons.
- Sancetta, A. and Satchell, S. (2004). The Bernstein copula and its applications to modeling and approximations of multivariate distributions. *Econometric Theory*, 20(3):535–562.
- Saporta, G. (2006). *Probabilités, analyse des données et statistique*. Editions technip.
- Saranyasoontorn, K., Manuel, L., and Veers, P. (2004). A Comparison of Standard Coherence Models for Inflow Turbulence With Estimates from Field Measurements. *Journal of Solar Energy Engineering*, 126(4):1069–1082.
- Schöbi, R. and Sudret, B. (2017). Structural reliability analysis for p-boxes using multi-level meta-models. *Probabilistic Engineering Mechanics*, 48:27–38.
- Schobi, R., Sudret, B., and Wiart, J. (2015). Polynomial-chaos-based Kriging. *International Journal for Uncertainty Quantification*, 5(2).
- Schoefs, F. and Tran, T. (2022). Reliability updating of offshore structures subjected to marine growth. *Energies*, 15(2):414.
- Schütz, W. (1996). A history of fatigue. *Engineering Fracture Mechanics*, 54(2):263–300.
- Segers, J., Sibuya, M., and Tsukahara, H. (2017). The empirical beta copula. *Journal of Multivariate Analysis*, 155:35–51.
- Sempreviva, A., Barthelmie, R., and Pryor, S. (2008). Review of methodologies for offshore wind resource assessment in European seas. *Surveys in Geophysics*, 29:471–497.
- Shahriari, B., Swersky, K., Wang, Z., Adams, R., and De Freitas, N. (2015). Taking the human out of the loop: A review of Bayesian optimization. *Proceedings of the IEEE*, 104(1):148–175.
- Shang, B. and Apley, D. (2020). Fully-sequential space-filling design algorithms for computer experiments. *Journal of Quality Technology*, 53:1 – 24.
- Shapley, L. S. et al. (1953). A value for n-person games.
- Shields, M., Beiter, P., Nunemaker, J., Cooperman, A., and Duffy, P. (2021). Impacts of turbine and plant upsizing on the levelized cost of energy for offshore wind. *Applied Energy*, 298:117189.
- Simley, E., Fleming, P., and King, J. (2020). Design and analysis of a wake steering controller with wind direction variability. *Wind Energy Science*, 5(2):451–468.
- Slot, R. M., Sørensen, J. D., Sudret, B., Svenningsen, L., and Thøgersen, M. L. (2020). Surrogate model uncertainty in wind turbine reliability assessment. *Renewable Energy*, 151:1150 – 1162.
- Sobolí, I. (1993). Sensitivity estimates for nonlinear mathematical models. *Mathematical Modelling and Computational Experiments*, 1:407.

- Sobol, I. and Gresham, A. (1995). On an alternative global sensitivity estimators. *Proceedings of SAMO*, pages 40–42.
- Soize, C. and Ghanem, R. (2004). Physical systems with random uncertainties: chaos representations with arbitrary probability measure. *SIAM Journal on Scientific Computing*, 26:395–410.
- Song, E., Nelson, B. L., and Staum, J. (2016). Shapley effects for global sensitivity analysis: Theory and computation. *SIAM/ASA Journal on Uncertainty Quantification*, 4(1):1060–1083.
- Sriperumbudur, B., Gretton, A., Fukumizu, K., Schölkopf, B., and Lanckriet, G. (2010). Hilbert Space Embeddings and Metrics on Probability Measures. *J. Mach. Learn. Res.*, 11:1517–1561.
- Stieng, L. and Muskulus, M. (2020). Reliability-based design optimization of offshore wind turbine support structures using analytical sensitivities and factorized uncertainty modeling. *Wind Energy Science*, 5:171–198.
- Straub, D. (2014). *Engineering risk assessment*, pages 333–362. Springer.
- Sudret, B. (2008). Global sensitivity analysis using polynomial chaos expansions. *Reliability engineering & system safety*, 93(7):964–979.
- Sudret, B. (2013). *Probabilistic Design of Structures Submitted to Fatigue*, chapter 5, pages 223–263. John Wiley & Sons, Ltd.
- Sullivan, T. (2015). *Introduction to uncertainty quantification*, volume 63. Springer.
- Sun, F., Wang, Y., and Xu, H. (2019). Uniform projection designs. *The Annals of Statistics*, 47:641 – 661.
- Suresh, S. (1998). *Fatigue of materials*. Cambridge university press.
- Sutherland, H. (2000). A summary of the fatigue properties of wind turbine materials. *Wind Energy: An International Journal for Progress and Applications in Wind Power Conversion Technology*, 3(1):1–34.
- Tabandeh, A., Jia, G., and Gardoni, P. (2022). A review and assessment of importance sampling methods for reliability analysis. *Structural Safety*, 97:102216.
- Teixeira, R., Nogal, M., and O'Connor, A. (2021). Adaptive approaches in metamodel-based reliability analysis: A review. *Structural Safety*, 89:102019.
- Torre, E., Marelli, S., Embrechts, P., and Sudret, B. (2019). A general framework for data-driven uncertainty quantification under complex input dependencies using vine copulas. *Probabilistic Engineering Mechanics*, 55:1–16.
- Trefethen, L. (2008). Is Gauss quadrature better than Clenshaw–Curtis? *SIAM review*, 50(1):67–87.
- Van der Hoven, I. (1957). Power spectrum of horizontal wind speed in the frequency range from 0.0007 to 900 cycles per hour. *Journal of Atmospheric Sciences*, 14(2):160–164.
- Van Kuik, G., Peinke, J., Nijssen, R., Lekou, D., Mann, J., Sørensen, J., Ferreira, C., van Wingerden, J., Schlipf, D., Gebraad, P., et al. (2016). Long-term research challenges in wind energy—a research agenda by the European Academy of Wind Energy. *Wind energy science*, 1(1):1–39.
- Vanem, E. (2016). Joint statistical models for significant wave height and wave period in a changing climate. *Marine Structures*, 49:180–205.

- Vanem, E., Fekhari, E., Dimitrov, N., Kelly, M., Cousin, A., and Guiton, M. (2023). A joint probability distribution model for multivariate wind and wave conditions. In *International Conference on Offshore Mechanics and Arctic Engineering*, volume 86847, page V002T02A013. American Society of Mechanical Engineers.
- Veers, P. (1988). Three-dimensional wind simulation. Technical report, Sandia National Labs., Albuquerque, NM (USA).
- Veers, P., Dykes, K., Lantz, E., Barth, S., Bottasso, C., Carlson, O., Clifton, A., Green, J., Green, P., Holttinen, H., et al. (2019). Grand challenges in the science of wind energy. *Science*, 366(6464):eaau2027.
- Walter, C. (2015). Moving particles: A parallel optimal multilevel splitting method with application in quantiles estimation and meta-model based algorithms. *Structural Safety*, 55:10–25.
- Wand, M. and Jones, M. (1994). *Kernel smoothing*. CRC press.
- Wang, Z. and Song, J. (2016). Cross-entropy-based adaptive importance sampling using von Mises-Fisher mixture for high dimensional reliability analysis. *Structural Safety*, 59:42–52.
- Warnock, T. (1972). Computational investigations of low-discrepancy point sets. In *Applications of number theory to numerical analysis*, pages 319–343. Elsevier.
- Waskom, M. (2021). Seaborn: statistical data visualization. *Journal of Open Source Software*, 6(60):3021.
- Wilkie, D. and Galasso, C. (2021). Gaussian process regression for fatigue reliability analysis of offshore wind turbines. *Structural Safety*, 88:102020.
- X., Z. (2022). *Surrogate Modeling for Stochastic Simulators Using Statistical Approaches*. PhD thesis, Chair of Risk, Safety and Uncertainty Quantification, ETH Zurich.
- Zhan, L., Letizia, S., and Iungo, G. (2020). Optimal tuning of engineering wake models through lidar measurements. *Wind Energy Science*, 5(4):1601–1622.
- Zhang, P. (1996). Nonparametric importance sampling. *Journal of the American Statistical Association*, 91(435):1245–1253.

